Simulation of Microstructural Evolution of Selective Laser Melting of Metal Powders

By:

Omar Eduardo Lopez Botello

A thesis submitted in partial fulfilment of the requirements for the degree of
Doctor of Philosophy

The University of Sheffield
Faculty of Engineering
Department of Mechanical Engineering

June of 2016

A mi esposa

Abstract

Selective Laser Melting (SLM) is an Additive Manufacturing (AM) process used to create 3D objects by laser melting pre-deposited powdered feedstock. During SLM, powdered material is fused layer upon layer, the scanning laser melts regions of the powder bed that corresponds to the geometry of the final component. During SLM the component undergoes rapid temperature cycles and steep temperature gradients. These processing conditions generate a specific microstructure for SLM components. Understanding the mechanism by which these generated microstructures evolve can assist in controlling and optimising the process.

The present research develops a two dimensional Cellular Automata – Finite Element (CA-FE) coupled model in order to predict the microstructure formed during the melting process of a powdered AA-2024 feedstock using the AM process SLM. The presented CA model is coupled with a detailed thermal FE model which computes the heat flow characteristics of the SLM process. The developed model takes into account the powder-to-liquid-to-solid transformation, tracks the interaction between several melt pools within a melted track, and several tracks within various layers. It was found that the simulated temperature profiles as well as the predicted microstructures bared a close resemblance with manufactured AA-2024 SLM samples.

The developed model predicts the final microstructure obtained from components manufactured via SLM, as well as is capable of predicting melt pool cooling and solidification rates, the type of microstructure obtained, the size of the melt pool and heat affected zone, level of porosity and the growth competition present in microstructures of components manufactured via SLM. The developed models are an important part in understanding the SLM process, and can be used as a tool to further improve consistency of part properties and further enhance their properties.

Acknowledgements

My greatest thanks go to my supervisor Dr. Kamran Mumtaz. His guidance, counselling and advice were crucial in undertaking this research. Special thanks also to Dr. Christophe Pinna and Dr Iain Todd for their immense input throughout this work. Many thanks also to my colleagues Pratik Vora, Neil Harrison, Kate Pitt, Haider Ali and Miguel Zavala for their prompt assistance and support. Thanks to the National Council of Science and Technology (CONACyT) of Mexico for giving me the opportunity of making a PhD abroad.

I would also thank my family and friends for their encouraging words and timely support throughout my time in the UK. Thanks to all of my friends over in Sheffield, special thanks to Martha, Victor, Jimena, Sara, Javier, Zusej, Mike, Nataly, Brenda and Alberto for their support and advice throughout the development of my PhD as well as making my time in Sheffield more enjoyable.

Last and most important of all, I would like to thank my wife, Monica, for her strong belief in me, her encouraging words, timely support, advice, guidance, help and all the patience she had when difficult moments were present. Thank you!!!

Nomenclature

AM	Additive Manufacturing
SLM	Selective Laser Melting
CA	Cellular Automata
FEM	Finite Element Method
CAD	Computer Aided Design
STL	Stereo lithography
ASTM	American Society for Testing and Materials
LD	Laser Diameter
LP	Laser Power
PD	Point Distance
ET	Exposure Time
PSD	Particle Size Distribution
Ab	Absorptivity
R	Reflectivity
S	Spreading coefficient
Ar	Argon
N_2	Nitrogen
He	Helium
r_c	Critical radius
T	Temperature
Z	Number of total neighbours
k_b	Boltzmann constant
L_{at}	Atomic latent heat of fusion
T_m	Melting temperature
v^*	Growth velocity
r_{tip}	Dendrite tip radius
w_{eut}	Eutectic
CET	Columnar to equiaxed transition
RS	Rapid solidification
G	Temperature Gradient

V	Solidification rate or velocity of the solid-liquid interface
CA-FE	Cellular Automata-Finite Element
LENS	Laser Engineered Net Shaping
PF	Phase Field
MC	Monte Carlo
LBM	Lattice Boltzmann Method
AA	Aluminium Alloy
Al	Aluminium
Cr	Chromium
Cu	Copper
Fe	Iron
Mg	Magnesium
Mn	Manganese
Si	Silicon
Ti	Titanium
Zn	Zinc
P_T	Property (density, thermal conductivity, etc.)
f_s	Solid fraction
H	Enthalpy
K	Thermal conductivity
P	Porosity
B	Deformation parameter
A	Area
Cp	Specific Heat Capacity
CFD	Computational Fluid Dynamics
UDF	User Defined Functions
APDL	Ansys Parametric Design Language
T_{sol}	Solidus Temperature
T_{liq}	Liquidus Temperature
T_{amb}	Ambient Temperature
hc	Convection coefficient
HAZ	Heat Affected Zone
FVM	Finite Volume Method

T_r	Recoating Time
RSP	Rapid solidification processing
LN	Number of layers
GS	Grain Size Number
DOE	Design of Experiments
HS	Hatch Spacing
HNO_3	Nitric Acid
HCl	Hydrochloric Acid
HF	Hydrofluoric Acid

λ	Wavelength
γ_{sl}	Solid-liquid interface surface tension
γ_{sv}	Solid-vapour interface surface tension
γ_{lv}	Liquid-vapour interface surface tension
$d\gamma/dT$	Surface tension temperature coefficient
ΔG	Nucleation barrier
Γ_{sl}	Gibbs-Thomson coefficient
ΔT	Undercooling temperature
α'	Transition from a rough to faceted interface
η_1	Number of nearest neighbours
λ_1	Primary dendrite arm spacing
λ_2	Secondary dendrite arm spacing
ρ	Density
ρ_{pwd}	Bulk Density
ΔH^{fus}	Latent heat of fusion
Ψ	Flattened surface fraction
ε	Emissivity
σ	Stefan-Boltzmann constant
α_{ii}	Anisotropic enhancement factor
$\lvert\dot{T}\rvert$	Cooling rate

Table of Contents

List of Figures

List of Tables

1. Introduction

1.1 Background

The emergence of Additive Manufacturing (AM) technologies first came in the late 1980's, it has been widely expected to revolutionise the manufacturing of complex components, from medical implants to jet-engine components (Powley, 2015). Since these technologies appeared, they have been developed and applied to a wide range of industrial and research applications. With the further development of metal AM technologies, it has proven to be a promising technology for the manufacturing and development of complex products. AM technologies allow parts to be produced with high geometric freedom that can be difficult to produce using conventional manufacturing processes, as well as to reduce the lead time from design to market (Mumtaz and Hopkinson, 2010). According to the Wohler's report (Wohlers, 2013) the metal AM technologies have been in a constant growth since they started to be available at the market (see Figure 1.1). The Selective Laser Melting (SLM) technology is one of the most used and studied technologies of metal AM (Wohlers, 2013).

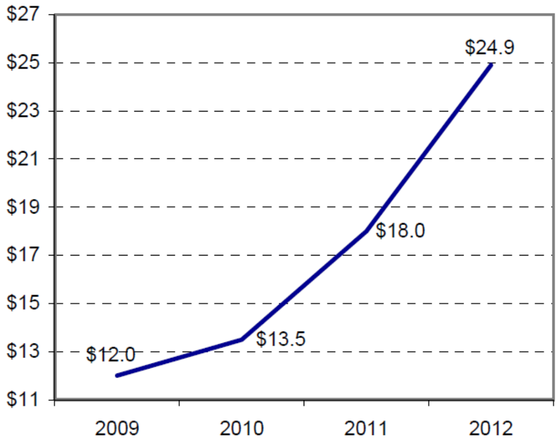

Figure 1.1 Revenue (in millions of dollars) from metals additive manufacturing (Wohlers, 2013).

In SLM near full and full density parts can be produced without the need for post-processing steps (Kruth et al., 2004), and usually the mechanical properties of parts produced by SLM can be comparable to those manufactured using conventional manufacturing techniques (Tolosa et al., 2010, Chlebus et al., 2011). One of the limitations that have truncated the further development and application of this technology is the difficulty of controlling or obtaining a modified or tailored microstructure depending in the particular needs of the part, despite the amount of work that has been conducted in this field of interest. On the other hand, studies on the thermal gradients generated during the processing of parts have been conducted in order to have a better understanding of the process, and to predict resultant effects due to the thermal history in the process (Roberts et al., 2009, Loh et al., 2015, Khairallah and Anderson, 2014).

Nevertheless, when users aim to gain more control over the process or to find the optimum processing parameters; experimental trials have to be undertaken in order to obtain the desired results, increasing the total energy consumption required to manufacture a part, as well as increasing the amount of time and material needed during the manufacturing. However, for other widely used manufacturing technologies such as casting, the control and optimisation of the process and of the properties of the resultant part is all made via numerical simulations; reducing the amount of time, material and energy consumption required for the manufacturing of the component.

A tool capable of predicting the developed microstructure on components manufactured via SLM will lead the SLM process to have the advantages of other manufacturing process (e.g. casting process) as well as further developments on the technology. The tool could lead to manufacture components with tailored microstructures if it is developed properly, as it has been done before with the casting process using the ProCast software developed by ESI Group.

1.2 Novelty Statement

To date no academic work has investigated the development of a tool capable of modelling microstructural growth within the Selective Laser Melting(SLM) process. This is the first work of its kind, a novel self-developed Cellular Automata – Finite Element (CA-FE) coupling capable of predicting the microstructural evolution of a component manufactured using the metallic powder bed process SLM.

The simulation developed within this work uses a novel Finite Element Method (FEM) approach that accurately calculates the thermal history within the SLM process. The complex thermal history within the SLM process has been modelled in other work (Shiomi et al., 1999, Matsumoto et al., 2002, Guo-feng and Guang-nan, 2004, Roberts et al., 2009, Gusarov et al., 2007, Gusarov and Smurov, 2009, Gusarov and Smurov, 2010, Körner et al., 2011, Song et al., 2012, Safdar et al., 2013, Loh et al., 2015, Foroozmehr et al., 2016), however none of these include detailed properties of the materials modelled (i.e. critical solid, mushy zone and liquid properties) in order to accurately calculate the temperature distributions within the powder bed. This work is the first of its kind documenting an approach capable of predicting the melt pool cooling and solidification rates, the type of microstructure obtained, the size of the melt pool, the Heat Affected Zone (HAZ) and the level of porosity within an SLM manufactured component. The data obtained from the developed approach is then used within the novel CA-FE coupling and finally used to predict the grain growth competition present within an SLM processed microstructure.

1.3 Aim and Objectives of the Research

The aim of this research is to develop a tool able to predict the microstructural evolution of metallic components processed via SLM, using the CA-FE coupling. Such development would need the creation of a novel approach that accurately calculates the involved thermodynamics in the SLM process. Coupling the results obtained with this approach with the CA would create a novel tool that will be able to predict the microstructural evolution of a component processed with SLM, taking into account the thermal history of the component.

1.3.1 Objectives

- Develop a CA model for the nucleation and growth of grains.
- Develop a FEM model to calculate the most realistic thermodynamics involved during the SLM processing.
- Couple the CA and FEM results in order to acquire the full growth – thermal history of the part.
- Validate the results obtained on the model with experimental results.

1.4 Thesis Structure

The aim and objectives described in section 1.3 were accomplished following defined and planned steps. A detailed representation of the steps followed during the development of the current research can be observed in Figure 1.2. Several steps were undertaken in parallel even though it was not represented on the diagram.

In order to accomplish most of the proposed steps, aims and objectives of the current research, a complete understanding of the SLM process is required. The understanding of the SLM process will be in depth, i.e. familiarise with all the parameters involved during the manufacturing of a layer by layer metallic component with this process and the solidification theory involved in the manufacturing process. This stage is marked as the first step of the methodology shown, and it is described with more detail in Chapter 2 of the present work.

Once these phenomena are understood, simulation techniques suitable for the objectives and aims of the present work are explored in the second stage of the methodology. The exploration is undertaken in order to select, within the third step of the methodology, the most suitable techniques to simulate the SLM process, in both thermal and microstructural ways. Both the explored theory and the selected techniques are described in more detail in Chapter 2.

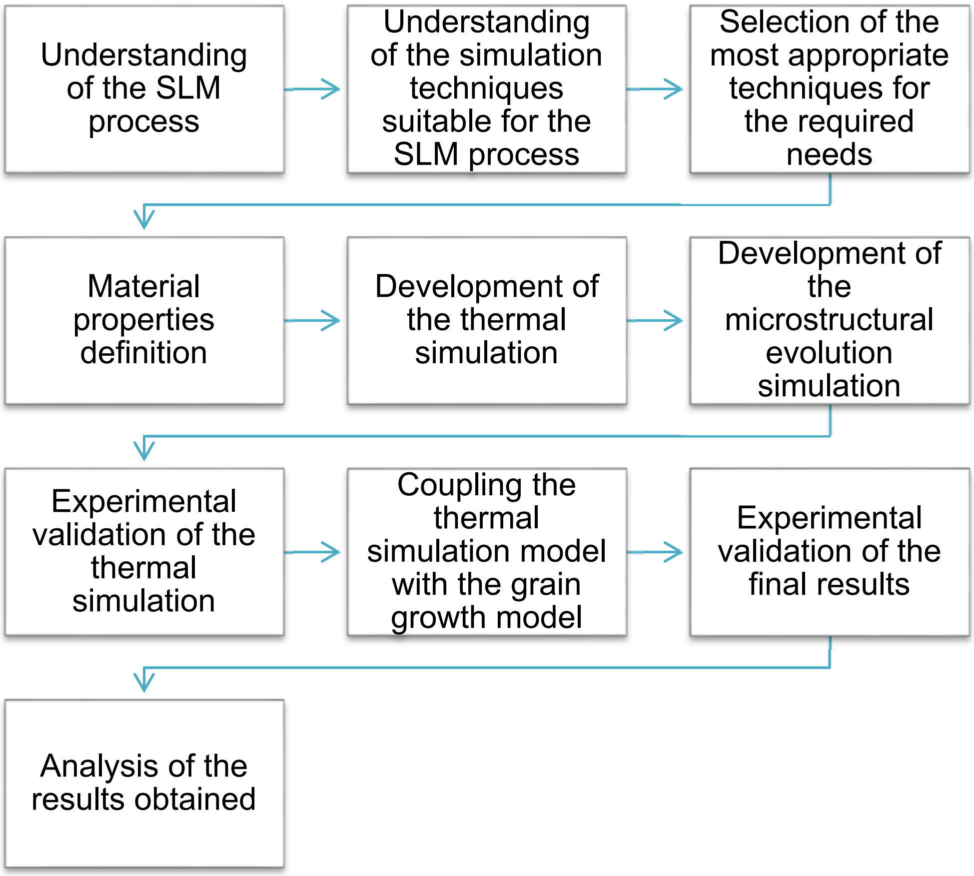

Figure 1.2. Followed methodology

Once the theory is established and understood, the material to use will be determined. In Chapter 3 detailed material properties used in the developed simulation for both solid and powder material are defined, as well as the equations used to calculate some of those properties are detailed.

With the material of interest selected in Chapter 3, as well as the modelling techniques mentioned in Chapter 2, the thermal simulation and the tool to predict the microstructural evolution are developed and described in Chapter 4. A detailed description of the process followed during the development of both the simulation and the tool, as well as brief obtained results are presented within the Chapter.

Experimental validation was then performed to the developed simulation and tools in order to determine its reliability. The experimental procedures followed in order to obtain the data of interest (melt pool dimensions, average grain size) are described in Chapter 5. In Chapter 6 the results obtained from both the FEM simulation and the CA-FE tool are then compared with experiments performed on the SLM system in order to validate with experiments and it was determined if the developed simulation and tool are reliable and accurate.

After the validation was performed, further data obtained from the developed FEM simulation and CA-FE tool is analysed and discussed in Chapter 7. Chapter 7 defines the capabilities of the developed research as well as future areas of opportunity for further research.

2. Literature Review

The development of a numerical tool capable to predict the microstructure development in a component manufactured via SLM requires knowledge in the SLM process, solidification theory as well as in simulation techniques. In order to have an in depth understanding of the SLM process, different factors that affect the processing of metallic components will be briefly described within the Chapter. Once the process is understood, the solidification theory is briefly described in order to understand the physical phenomena involved during the development of the microstructure. Next, a brief description of suitable simulation techniques as well as the gap of knowledge is highlighted.

2.1. Selective Laser Melting Process

SLM is an AM process which uses a three-dimensional CAD (computer aided design) model as information source, usually in the form of a STL (stereo lithography) file. This file is sliced (divided in an ‘x’ amount of two-dimensional layers depending on the thickness defined) by software, the ‘sliced’ file is then sent to the SLM machine. Using energy in form of a high powered laser beam, a three-dimensional metallic part is then created by fusing the metallic powder together layer-by-layer. The ASTM (American Society for Testing and Materials) committee in AM technologies F42, describes the process using the term of laser sintering, despite that SLM fully melts the powder particles into a solid homogeneous (ASTM, 2010).

Metal AM processes have seen an increased interest among research institutions and commercial users over the last years. Figure 2.1 shows how the revenues for AM products and services have been increasing over the last years (1993-2012). This can be attributed because of the advantages of these manufacturing techniques, which can: build complex geometries, directly fabricate components with moving parts, and reduce material waste. These can be reflected in lowering the total costs of production of a product.

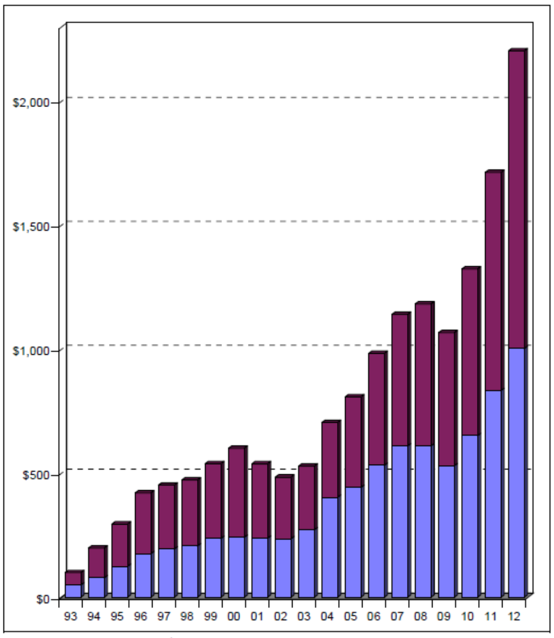

Source: Wohlers Associates, Inc.

Figure 2.1. Worldwide revenues (in millions of dollars) for AM products and services from 1993 to 2012. The lower (blue) segment of the bars indicates products, while the upper (burgundy) segment indicates services. Neither category includes secondary processes, such as tooling, moulded parts, or castings. (Wohlers, 2013)

A typical configuration of the SLM machine is shown in Figure 2.2. The parts are manufactured on a substrate plate (usually metallic) which is mounted on a processing table that moves vertically in the build chamber, the movement of this table is equivalent to the thickness of each slice of the CAD model (usually tenths of microns). A container stores the metallic powder and disposes it each layer, immediately after a leveller spreads it homogenously across the substrate plate. Afterwards the laser beam scans the corresponding cross-section of the layer into the powder, which selectively melts and starts forming a solid part. This process is repeated for each layer of the CAD model until the final layer has been processed.

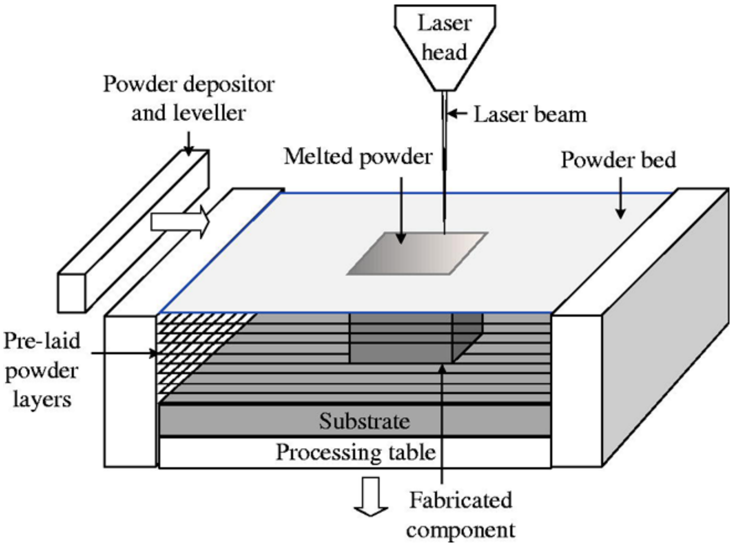

Figure 2.2. Selective Laser Melting Process(Mumtaz and Hopkinson, 2010)

2.1.1. Processing Parameters and Factors that affect the SLM Process

A variety of parameters and factors are involved during the fabrication of components with SLM. Some of the most important phenomena of the selective bean melting of powders are mentioned in Figure 2.3.

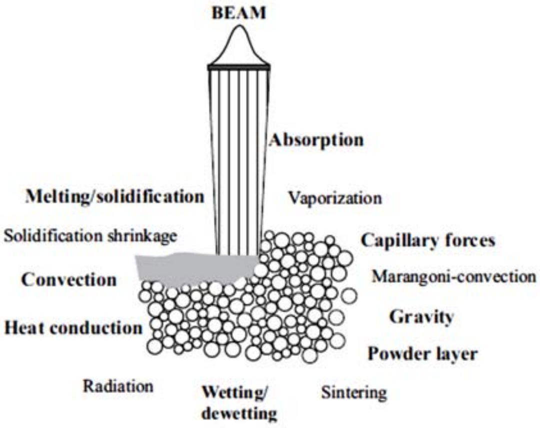

Figure 2.3. Physical phenomena during selective beam melting (Körner et al., 2011).

Within the section, a brief description of those parameters and factors considered as relevant to the present research will be presented.

2.1.1.1. Laser

As shown in Figures 2.2 and 2.3, a laser irradiates the surface of a powder bed as soon as the information of the corresponding cross-section of a layer is received. The absorbed energy is transformed into heat and dissipates across the powder bed due to the complex heat transfer properties of the powder bed. This heat fuses together powder particles forming a solid.

The properties of interest of a laser beam are the spot size, wavelength, laser power and the form in which the energy is delivered into the powder bed (pulsed or continuous). A continuous laser is considered as a Laser with constant Diameter (LD) that continuously emits light while it moves linearly with a constant scan speed through the cross section of the part, as represented in Figure 2.4a. These lasers usually have a constant energy output, and it is known that in most applications the heat is distributed homogeneously, having in consequence a homogeneous melt of the powder through the powder bed (Fischer et al., 2002).

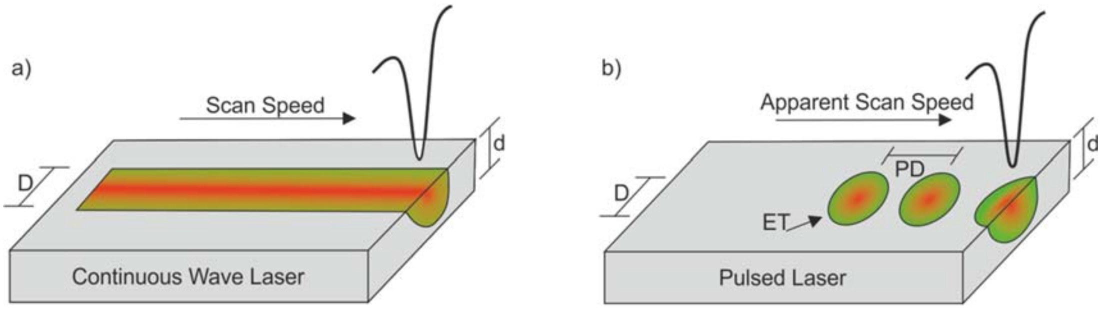

Figure 2.4. Representation of a Continuous Wave Laser and a Pulsed Laser.

Pulsed lasers emit light in the form of optical pulses, using small bursts of energy in order to melt the material up to a certain depth (d); the melt pool generated usually solidifies before the next pulse is applied (Yevko et al., 1998). Pulsed lasers overlaps multiple spots in order to scan a straight line (as seen in Figure 2.4b), these molten zones are evident in the overlapped solidified material seen in components produced with these types of lasers. These laser systems usually count with more parameters to control such as Laser Power (LP), Point Distance (PD), Exposure Time (ET), etc. The variation of these parameters will lead to an optimisation of parameters in order to obtain better results.

2.1.1.2. Material

The selection of the material of interest when manufacturing a component through SLM is made based on needed requirements of the final product. The thermo-physical properties of the material such as density, thermal conductivity and specific heat, determine the thermal history behaviour that would present. Generally, in a process like SLM, the thermal conductivity is one of the thermo-physical properties of more influence when processing the material and the thermal expansion coefficient is a critical value in order to determine the induced residual stresses during the solidification of the molten material. The mentioned properties are dependent of the alloy used, and the chemical composition of the alloy would determine in general terms the behaviour of the material.

The SLM technology uses material in form of powder, so the thermo-physical properties of the powder bed such as density, thermal conductivity (Loeb, 1954, Woodside, 1958, Laubitz, 1959, Zehner and Schlunder, 1970), absorption (Tolochko et al., 1997), between others, are different from those of the bulk material.

The absorption of a material is a complex phenomenon that describes the laser-material interaction or coupling. The absorption of a certain material can be affected by different factors such as the direction of the incident radiations, the surface roughness, the oxides present on the surface, the wavelength of the incident radiation, the temperature of the material and the type of material.

The absorptivity of a material is merely a surface phenomenon, and usually the oxide films (if present) may have a significant effect. The oxide films in order to have a considerable effect to the underneath material should be of a certain thickness (Steen and Mazumder, 2010).

Since the absorption/reflection phenomenon interacts with the atomic structure of the material, this means the absorption is also temperature dependent. As the temperature of the material increases, the phonon population increases as well; leading to more phonon-electron energy exchanges (Steen and Mazumder, 2010). At higher temperatures it is more likely that the electron of the irradiated material interacts with the phonons of the irradiated beam, thus the absorptivity increases and the reflectivity decreases.

As the SLM process uses powdered material, the absorption values of bulk materials are different to those of powdered materials. In order to obtain direct measurements of the absorption of powdered material, a complicated process is required (Tolochko et al., 1997). It has been demonstrated, through a numerical model, that the absorption of metal powders layers, as used in SLM, is significantly larger than its value on flat surfaces (Boley et al., 2015); this phenomenon is due to the multiple scatterings present in the powder bed, just as the interaction of a beam with short wavelength (1070 nm) and a rough surface (particle size of about 50 µm).

2.1.1.3. Melt pool dynamics

Due to the high thermal gradients induced to the metal powders by the high speed laser processing, oscillations in the behaviour of the molten material can be observed in the final parts. These oscillations affect the formation of the solid phase present during the processing, so its shape and size is affected by different phenomena during the molten stage of the material.

The surface and interface energies present in the molten material govern two phenomena, capillarity and wetting. Wetting is defined as the ability of a liquid to maintain contact with a solid surface; meanwhile capillarity is defined as the ability of a liquid to flow in narrow spaces without the assistance of external forces. Both liquid-solid characteristics are crucial in order to build successfully components with the SLM technology. Depending on the conditions of the molten and solid material, the liquid would wet differently the underneath material (see Figure 2.5).

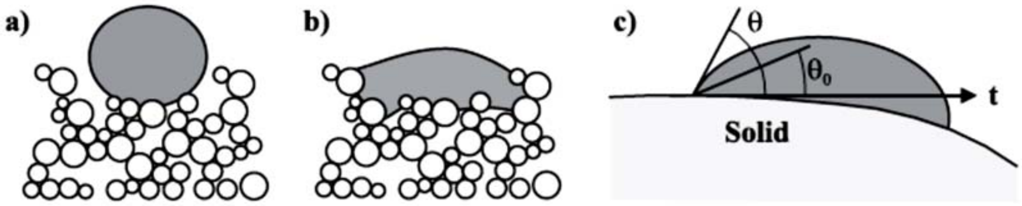

Figure 2.5. a)Non-wetting melt pool on top of the powder, b) wetting melt pool on top of the powder, c) dynamic wetting angle θ and equilibrium wetting angle θ$_0$ with respect to the tangent direction t (Körner et al., 2011).

The wetting is related to the surface tension of the solid-liquid interface (γ_{sl}), solid-vapour interface (γ_{sv}), and the liquid-vapour interface (γ_{lv}). Young's equation (Equation 2.1) defines the equilibrium of interfacial free energies by the contact angle θ (Young, 1805):

$$cos\theta = \frac{\gamma_{sv} - \gamma_{sl}}{\gamma_{lv}}$$ *Equation 2.1*

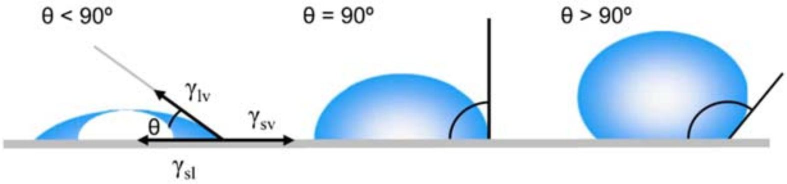

Figure 2.6. Illustration of contact angles formed by liquid drops on a smooth homogeneous solid surface (Yuan and Lee, 2013).

The liquid wets the solid as cos(θ)→1 (see Figure 2.6). In order to describe the wetting behaviour a spreading coefficient (Equation 2.2) is used (Das, 2003).

$$S = \gamma_{sv} - \gamma_{sl} - \gamma_{lv}$$ *Equation 2.2*

As the coefficient increases positively the spreading of the liquid is favoured. When the molten material becomes unstable on the solid (as the wetting angle increases), it breaks up into small spherical droplets called "balling" (Kruth et al., 2007). The formation of balling (see Figure 2.7) relates to the capillary instabilities induced due to the non-uniform heating during the laser processing temperature gradients.

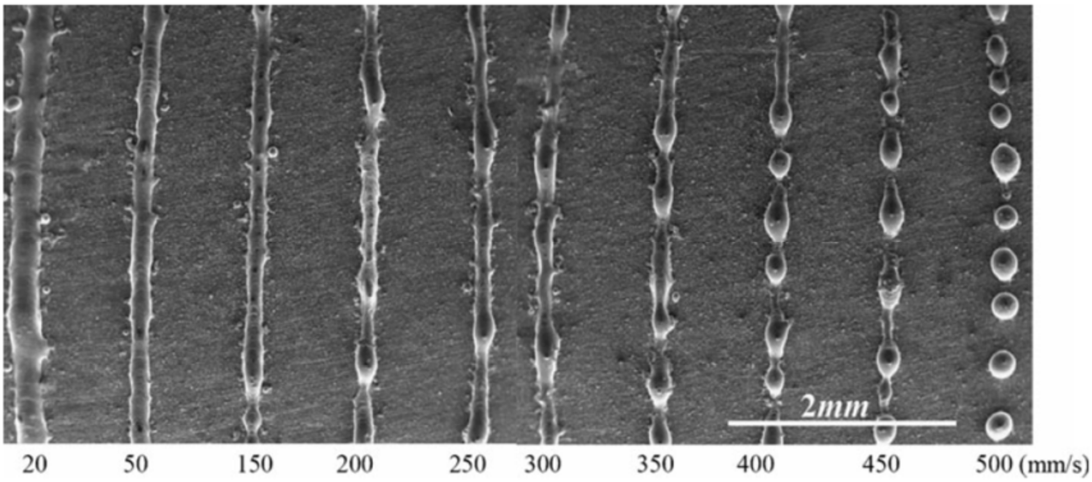

Figure 2.7. SEM images showing the balling characteristics of single scan tracks under different scan speeds (Li et al., 2012)

As the molten metal is formed, surface tension variations naturally tend to reduce, resulting in the break of the melt pool into these smaller droplets. In order to explain balling formation, the Plateau-Rayleigh capillary instability of a cylinder is used (Gusarov et al., 2007). If a strong non-wetting condition is present in the powder or in the underneath formed solid, balling is amplified.

During laser processing surface tension gradients are induced and drives the fluid flow from the centre of the melt pool toward the edges, this is known as Marangoni flow (see Figure 2.8). Marangoni flow is the dominant convection mechanism in melt pools formed with laser processing, since there are no Lorenz forces present (forces induced on moving charged particles in the presence of magnetic and electric fields) (Ion, 2005).

For pure metals as the temperature increases, the surface tension decreases, having a negative surface-tension-temperature coefficient ($d\gamma/dT$) (see Figure 2.8a) inducing a radially outward surface flow forming a wide shallow melt pool. For most of metal alloys ($d\gamma/dT$) is positive (Figure 2.8b) inducing a radially inward flow, that produces a downward flow in the centre of the melt pool forming a deep and narrow melt pool. Some systems go through a maximum (dγ/dT) after a certain temperature producing a complex flow, similar to that shown in Figure 2.8c.

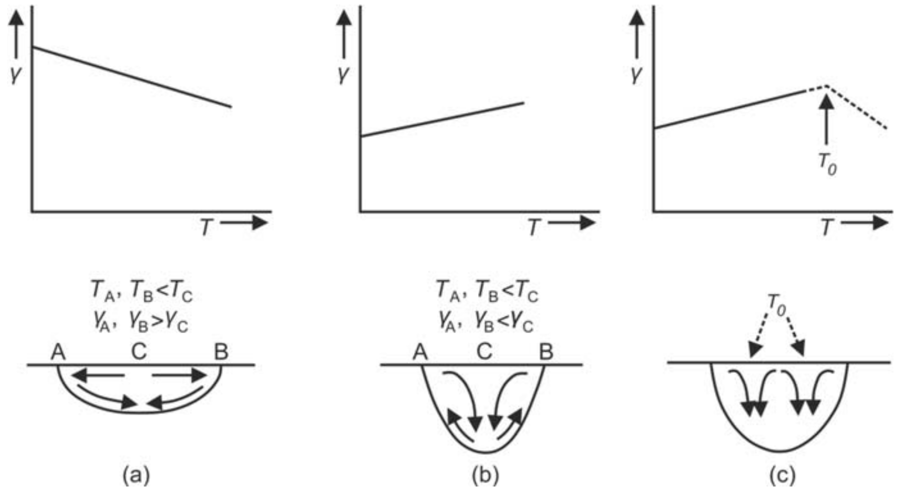

Figure 2.8. Schematic diagram illustrating the Heiple-Roper theory for variable weld penetration (Mills et al., 1998).

2.1.1.4. Environmental Effects

The metal powder used for the SLM process is melted and re-solidified inside a chamber, and the environment of this chamber is very important in order to obtain oxides-free parts. The environmental factors involved within the process usually are the effect of the inert gas inside the chamber and the effect of pre-heating the powder bed during the build.

Oxidation is usually present during laser processing of components, and it is an un-wanted phenomenon in produced parts. This phenomenon has been limited in commercially available SLM systems, since they use protective inert environments and a shield inert gas flow in the powder bed in order to maintain the oxygen contents in the working chamber in a very low value. The oxidation reaction is limited when the oxygen content in the chamber is below 0.5% (Zhang et al., 2013), limiting the interaction at high temperatures of oxygen and liquid metal.

The inert gases of protective and shield environments most commonly used are Argon (Ar), Nitrogen (N_2), Helium (He) and sometimes a deoxidiser (H_2). Parts produced under Ar and N_2 environments, exhibit near full density values, while parts produced with the same processing parameters and under He environments exhibit densities of around 90%. This effect on the part can be attributed to the shielding effect of the height of plasma plumes generated during the processing; since Ar and N_2 environments produce low height plasma plumes the coupling between the laser and the metal powder is maintained, meanwhile using He environments produce high height plasma plumes completely obstructing the transport of laser energy (Zhang et al., 2013). However, it is known that N_2 may react with some metals forming undesired nitrides in the microstructure affecting the mechanical properties of the produced parts; leaving as the best option the use of Ar as shielding and protective environment inert gas.

Laser processes such as SLM are known to have high cooling rates, large thermal gradients and thus induced residual stresses due to the large thermal gradients induced and due to the shrinkage of layers because of thermal contraction (Kempen et al., 2014). Due to the high temperatures experienced in the upper layers of the solid substrate, those layers will expand, while the colder underlying solid layers will restrict this expansions, inducing compressive stresses in the upper layers, as shown in Figure 2.9. In order to reduce this unwanted stresses and cracks generated because of those, pre-heating the powder bed is widely used.

By pre-heating the powder bed during laser processing thermal gradients are lowered as well as the cooling rates, thus the amount of thermal stresses induced and the amount of cracking are reduced (Kempen et al., 2014). Deformations due to induced residual stresses are lowered and even supressed having higher temperatures in the powder bed (Zhang et al., 2013). During the processing of some materials, pre-heating the powder bed can have a positive effect in the overall density of the component (Zhang et al., 2013). With high pre-heating temperatures, ceramics with low crack densities can be produced with SLM (Liu et al., 2015).

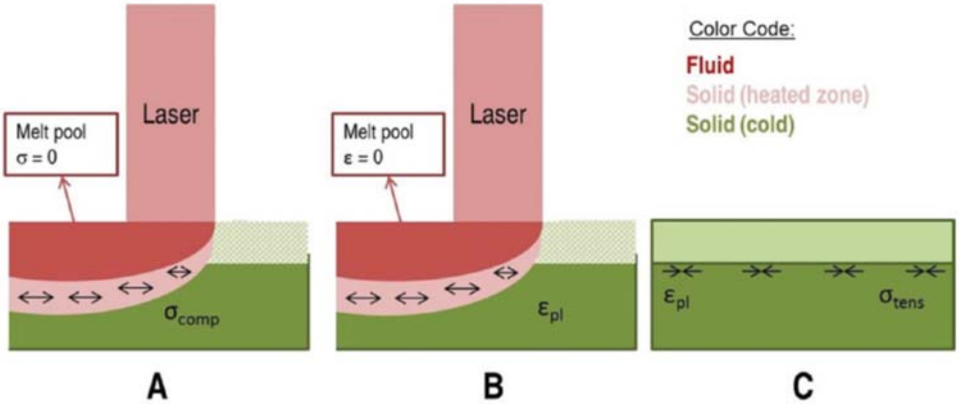

Figure 2.9. Formation of residual stresses due to thermal expansion of underlying layers (Kempen et al., 2014).

2.2 Solidification

A brief summary of the theory and of literature about the solidification phenomenon of metals is presented within this section. The solidification phenomena should be fully understood, since during the laser processing of components with SLM, the metallic powder fully melts and as it cools down it starts to solidify. With a better understanding of this area the SLM process can be understood thoroughly with ease.

2.2.1 Physical phenomena of the formation of microstructures in metals.

If an ingot is observed in cross-section along its length, the observed microstructure is the result of the interaction of many different physical phenomena during the solidification process of the ingot. The key aspects involved would be described within this section, as well as the different parameters that might influence the evolution and formation of the microstructure. The importance of the solid-liquid interface, the dendritic and eutectic structures, the competition between grains and the segregation phenomenon are some of the topics that would be briefly discussed next.

2.2.1.1 Nucleation

In a liquid, nucleation begins with a cluster of atoms of crystalline structure, which may occur due to random fluctuations in the liquid (Dantzig and Rappaz, 2009). As a nuclei commence to grow, a grain would be created. The nucleation phenomenon is based in thermodynamic concepts, in particular the consideration of the energy of the solid-liquid interface (γ_{sl}) of the embryo. Assuming the embryo as a sphere, the nucleation energy barrier (ΔG) is defined by Equation 2.3.

$$\Delta G = \frac{4\pi\gamma_{sl}r_c^2}{3} \qquad \textit{Equation 2.3}$$

Where r_c is the critical radius at which the embryo would be energetically stable in order to form a nucleus ($r_c = 2\Gamma_{sl}/\Delta T$, where Γ_{sl} is the Gibbs-Thomson coefficient, and ΔT the undercooling temperature). The critical radius is achieved by the thermal fluctuations present below the melting point of the metal. However, this theoretical approach undercooling temperatures of several hundred of Kelvins are required in order to form a nuclei, which is not consistent with the undercooling temperatures observed on experiments (Dantzig and Rappaz, 2009).

The theory of heterogeneous nucleation explains the nucleation behaviour in real systems, where the solidification phenomenon is usually initiated on foreign surfaces (surface of the mould, oxide skins, particles, etc.). Usually the undercooling temperature required to form nuclei is in the order of a few Kelvins. However, nucleation is still a phenomenon sensitive to the atomic scale thermal fluctuations, and because of this the position and the orientation of the first formed crystals at a macroscopic scale are almost impossible to predict. A statistical model (Rappaz, 1989) is used in order to calculate the distribution of the nucleation sites whose undercooling temperature, ΔT_{nucl}, could fit in a Gaussian distribution. As the local undercooling temperature

(Equation 2.4), ΔT, becomes greater to the critical undercooling temperature the nuclei would start to form a new grain.

$$\Delta T = T_{eq} - T \qquad \text{Equation 2.4}$$

where T is defined as the local temperature and T_{eq} is the equilibrium transformation temperature (i.e. the liquidus temperature). The average critical undercooling temperature (ΔT_N) usually is determined through experiments, as well as the standard deviation (ΔT_σ) and the maximum density of nucleation sites observed (n_{max}).

2.2.1.2 Description of the solid-liquid interface

During the solidification phenomenon, the nature and behaviour of the interface between the solid and liquid phases is determinant in the formation of crystals, and thus to the formation of the microstructure. The solid-liquid interface can be classified into three categories (Kurz and Fisher, 1998):

- Planar front, stable interface in the sense that perturbations melt back with time. This type of front is mainly obtained from the columnar growth of pure substances.
- Cell morphology, this morphology develops at the limit of the instability of the interface on the columnar growth. These morphologies are characterised by the growth of cells aligned with the thermal gradient.
- Dendritic morphology, the most common on metal alloys, corresponds to an unstable interface, where disturbances tend to amplify with time.

In addition to the described classification, the interface can be rough (as in most metals) or faceted (i.e. intermetallic semiconductors such as silicon). A rough interface is rough and uneven at the microscopic level, each facet being in fact a plane at the atomic scale. Those planes are the consequence of slower kinetics of attachment of the atoms, and it is associated with larger undercooling temperatures (Kurz and Fisher, 1998). In the fabrication of single crystal semiconductors (Czochralski process) the solid-liquid interface present is flat, although facets could be obtained.

The transition from a rough to faceted interface can be determined with Equation 2.5 (Jackson, 1984).

$$\alpha' = \frac{\eta_1 L_{at}}{Z k_b T_m} \qquad \textit{Equation 2.5}$$

where η_1/Z is the fraction of the total energy which is in a plane parallel to the surface., k_b the Boltzmann constant, L_{at} is the atomic latent heat of fusion and T_m the melting temperature of the material. For values of $\alpha < 2$ the interface should be rough on an atomic scale and the growth should be like the solidification observed in metals (Jackson, 1984). For values of $\alpha > 2$ the interface would be faceted, as observed in organic materials (Jackson, 1984).

2.2.1.3 Microstructure

As the nuclei form and are thermodynamically stable, they have a short theoretical spherical growth phase. Afterwards they form grains which continue their development along preferential directions. Those directions are related to the anisotropy of the interfacial energy and the kinetics of attachment of the atoms.

Dendritic grains are characterised for having primary dendrite arms, which are formed according to the preferential directions, with ramifications called secondary arms. In order to characterise dendritic structures, the primary and secondary spacing parameters (λ_1 & λ_2) are used (Figure 2.10). The primary and secondary spacing are dependent on the cooling rates and the temperature gradients present during the solidification, and thus they usually change from one point to another within the same solidified part. In addition, considerable changes might be present after the initial growth phase; usually this happens due to the dissolution and/or coarsening of the secondary arms of the dendritic structure. The material properties related to a part with dendritic structure are dependent on both spacing parameters.

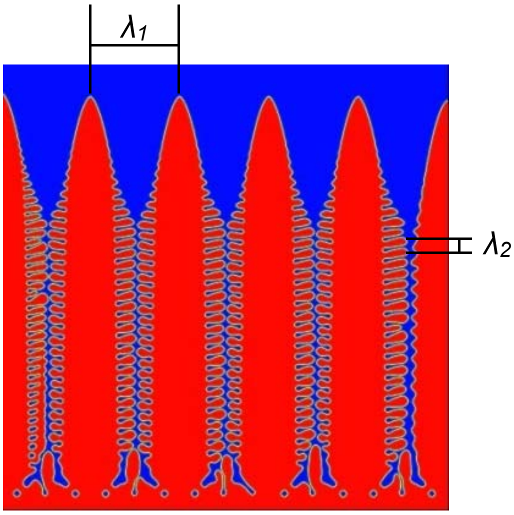

Figure 2.10 Primary and secondary spacing of dendritic structures.

Dendrite tips govern the growth of the dendrite arms. The undercooling temperature at the dendrite tip (ΔT) is given by Equation 2.6.

$$\Delta T = \Delta T_T + \Delta T_C + \Delta T_r + \Delta T_K \qquad \text{Equation 2.6}$$

In Equation 2.6, ΔT_T refers to the thermal undercooling, ΔT_C to the solutal undercooling, ΔT_r to the curvature undercooling and ΔT_K to the attachment kinetic of atoms undercooling. It should be noted that ΔT_r plays an important role: firstly, the curvature at the end of the tip is maximum, and secondly, the curvature varies at the tip of the dendrite. Therefore, ΔT_r also varies and the tip cannot be considered as isothermal. The heat diffusion in the solid and in the liquid must be taken into account, which increments notoriously the complexity of the problem. Note, that in most of the cases, except in rapid solidification and faceted interfaces, ΔT_K can be neglected.

A dendrite that grows in an undercooled melt can be approximated as a “needle crystal”, with a nearly parabolic shape, that grows at constant velocity. Solving the transport equations, the thermal (or solutal) field is obtained. The obtained field has the corresponding pairs of solutions of the growth velocity (v^*) and the tip radius (r_{tip}). When the surface energy is included in the equations, no stable solution exists (Dantzig and Rappaz, 2009). This issue leads to a second "solvability" condition that states that the product $r_{tip}^2 v^*$ is constant (Langer and Müller-Krumbhaar, 1977). Using both criteria, a unique value for the tip shape and growth velocity would be obtained. However, a relatively simple analytical procedure for computing a unique pair of v^* and r_{tip} that incorporates most of the essential phenomena has been developed (LGK model) (Lipton et al., 1987). The LGK model is widely used when modelling microstructures, since it provides a compact analytical form for obtaining the operating state (Dantzig and Rappaz, 2009).

As the solidification process proceeds the composition in the liquid would reach an invariant point, typically a eutectic (w_{eut}) or peritectic (would not be discussed in the scope of this work). A second phase would nucleate and grow with or at expenses of the first phase, this in order to proceed with the solidification in this invariant point. This is called eutectic growth, in which an exchange of solute between two solid phases occur via transport in the liquid phase (Dantzig and Rappaz, 2009).

The various combinations of materials and the volume fraction of the two formed phases affect the eutectic microstructure, leading to different eutectic morphologies (irregular, regular, divorced or nodular). An example of regular and irregular eutectic morphologies found in some binary systems is shown in Figure 2.11.

The general growth theory of Jackson and Hunt (Jackson and Hunt, 1966) for regular eutectics demonstrates how solute exchanges between the phases can contribute to decrease the required undercooling, as well as facilitates the understanding of the mechanisms involved in the solidification of the other types of morphologies found in eutectic systems (Dantzig and Rappaz, 2009).

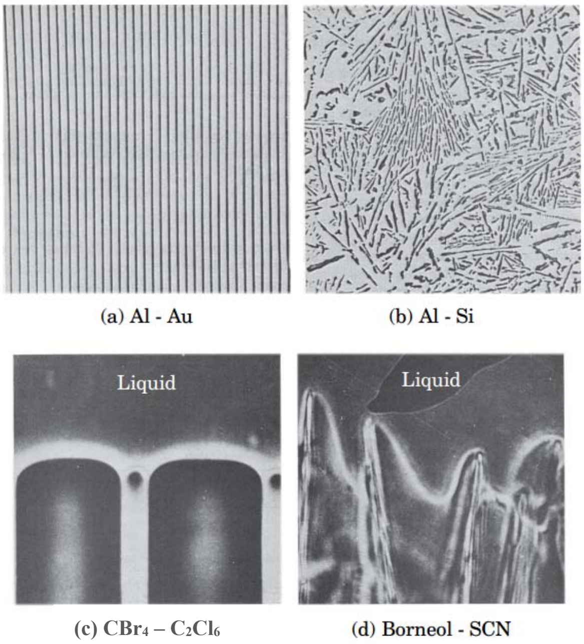

(a) Al - Au (b) Al - Si

(c) $CBr_4 - C_2Cl_6$ (d) Borneol - SCN

Figure 2.11 Regular (a & c) and irregular (b & d) eutectics (Dantzig and Rappaz, 2009).

In numerical models is often difficult to deal with the simultaneous growth of dendritic and eutectic grains; this due to the big difference that exists between the size of the dendritic grains and the size of the formed regular eutectic in which the spacing between the two phases is usually one or two orders of magnitude less than the secondary arm spacing of a dendrite. Usually, a eutectic grain is considered as a single structure in order to simplify this phenomenon.

2.2.1.4 Growth competition

Generally during the solidification of metallic alloys two types of grain morphologies are present, columnar and equiaxed. Sometimes a microstructural transition between these two morphologies can be found during certain solidification processes.

A columnar growth is characterised for having a preferential growth over one direction. Figure 2.12a and b show an example of regions during the solidification of an ingot with columnar growth present. The columnar grains form under a constrained growth, which means that grains are constrained to grow along the direction of the thermal gradient (usually a positive thermal gradient). In experiments, it has been observed that columnar grains whose preferential growth direction is along the thermal gradient would continue developing over others, leading to a further grain selection if required (Gandin and Rappaz, 1994).

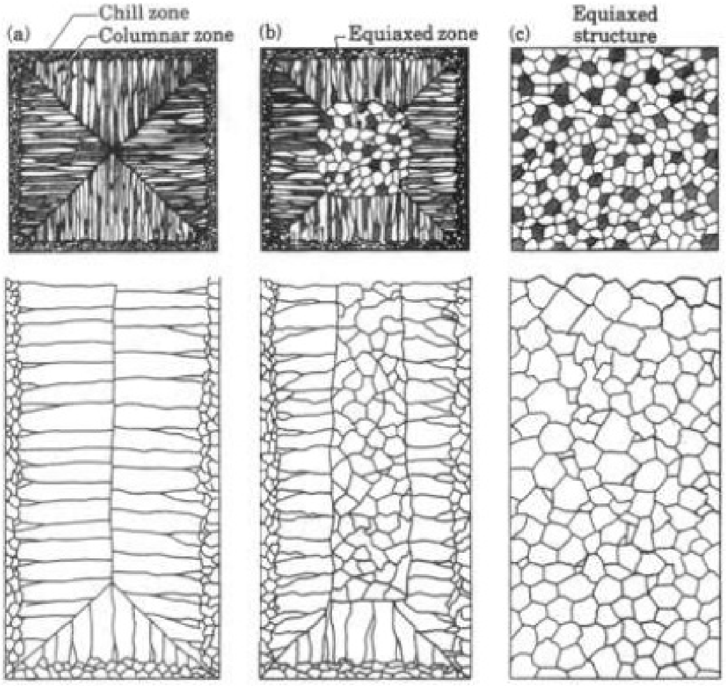

Figure 2.12 Schematic illustrations of three cast structures of metals solidified in a square mould: a) pure metals; b) solid-solution alloys; and c) structure obtained by heterogeneous nucleation of grains using nucleating agents. Source: G. W. Form, J. F. Wallace, J. L. Walker, and A. Cibula.

The selection of preferential growth direction in dendritic grains is based on the minimization of the surface energy, but because of their morphology, grain selection happens only due to the growth kinetics and local cooling conditions. As a result of the grain selection, there is a reduction in the number of grains and the microstructure will have only grains orientated in the same direction. Parts with this type of microstructure usually have anisotropic properties (i.e. mechanical). This phenomenon usually is used in “grain selectors” (Goulette et al., 1986), which impose a defined geometry in order to select a single grain as the solidification front advances and thus grow a single crystal part.

In the case of non-dendritic grains, minimizing the surface energy of the solidification front can become predominant in the growth competition at low cooling rates.

An equiaxed growth is characterised by having a similar size in all directions of the melt, as opposed to columnar growth. When casting ingots, this phenomenon is usually observed in two main areas: on the surface of the mould, when the cooling rate is at its maximum value and heterogeneous nucleation sites are present (see Figure 2.12a & b); and sometimes on the centre of the cast, where the temperature gradient is almost zero (see Figure 2.12b). In order to obtain a completely equiaxed microstructure during the solidification of an ingot, usually nucleation agents are added to the melt as external nucleation sites (see Figure 2.12c).

Usually this type of structures is related with isotropic properties (e.g. mechanical properties), due to the fact that the microstructure is homogeneous on all directions.

Under certain conditions of the solidification process a microstructural transition between columnar grains and equiaxed grains may be present; this is called columnar to equiaxed transition (CET). As the columnar grains advance in the melt nucleation of equiaxed grains in the free liquid may occur, these new grains may completely block the growth of the columnar front forming a new equiaxed zone (see Figure 2.12b). The “blockage” is said to be because of both mechanical and solutal interactions of the grains (Martorano et al., 2003).

The properties (e.g. mechanical properties) along the equiaxed and columnar zones differ, and depending on the final application of the part the equiaxed grains would be maximised for more isotropic properties, or minimised in order to grow single crystals or have anisotropic properties.

2.2.1.5 Rapid solidification

Rapid Solidification (RS) can be defined as the use of high cooling rates or the rapid extraction of thermal energy in order to include both superheat and latent heat during the transition from a liquid state at high temperatures, to solid material at room temperature producing high rates of advance of the solidification front (*V>1cm/s*) (Lavernia and Srivatsan, 2010, Kurz and Fisher, 1998). A process with cooling rates greater than 10^4 K/s is considered in the RS regime; however, cooling rates of 10^3 K/s is known to generate rapidly solidified microstructures in some cases (Lavernia and Srivatsan, 2010).

RS does not affect the solidification nucleation model presented before, only the growth is considered differently (Kurz and Fisher, 1998). In order to know how microstructures develop in the RS process, usually the diagram shown in Figure 2.13 represent what is to be dealt with on RS. Figure 2.13 is usually referred as the “G-V” diagram, G referring to the temperature gradient at the solid-liquid interface and the V referring to the rate of solidification or the velocity of the solid-liquid interface.

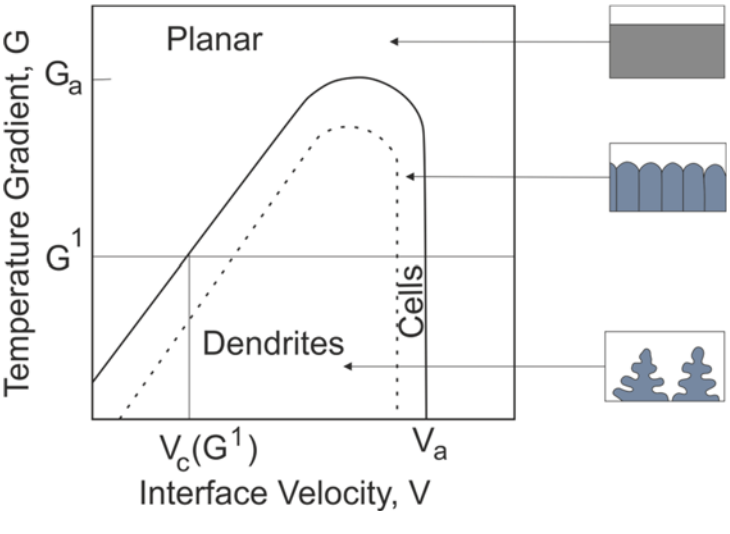

Figure 2.13 Schematic of G vs V showing regions of different solidification microstructure (Kurz and Fisher, 1998).

When an alloy of a given composition is imposed with a positive temperature gradient, G^1, at low growth rates ($V=V_c$), a transition from planar to cellular morphology due to constitutional undercooling is present. This undercooling happens as a result of the inability of solute atoms to diffuse away from the solidification front quickly enough to maintain a uniform composition at the liquid. Transition to dendrites is present as the velocity of the solidification front increases or as the temperature gradient decreases, as illustrated (Jacobson and McKittrick, 1994). It can also be observed, at high rates ($V>V_a$), a reverse transition from cells to a planar front, which is essentially independent of the imposed temperature gradient. Above a temperature gradient, G_a, the planar front would always be stable independent from the solidification front velocity (Kurz and Fisher, 1998). With the shown diagram, the development of rapidly solidified microstructures for alloys of constant composition can be predicted if the solidification front velocity and the temperature gradient are known. Alloys of different compositions will have different forms of the G-V curve.

RS can result in a solid with equal or similar composition to that of the liquid, this happens because there is insufficient time for the solute to redistribute in the liquid during the solidification process (Jacobson and McKittrick, 1994), so it can be considered that there is almost null segregation in the solidification process. Considering a general eutectic alloy, the RS can result in three different circumstances. If the alloy is undercooled sufficiently, solute trapping can result in certain regions of the solid solution. If the composition of the alloy is near the eutectic composition, it may be possible to undercool below the glass transition temperature, where an amorphous structure can be formed. And the third circumstance is that neither of these mentioned temperatures is accessible, then a two-phase solid would be formed; the solid will have either a coupled eutectic microstructure or a dendritic (or cellular) microstructure in which one phase grows rapidly and the second phase solidifies in between the dendrites or cells of the primary phase.

At the RS solidification rates, eutectic structures cannot form, due to the inability to maintain a planar interface; so, the solidification structures transition to cells or dendrites. In some cases, when having the highest solidification rates, solute trapping occurs and forms single-phase, metastable solid solution; amorphous phases or glass is even possible in other cases.

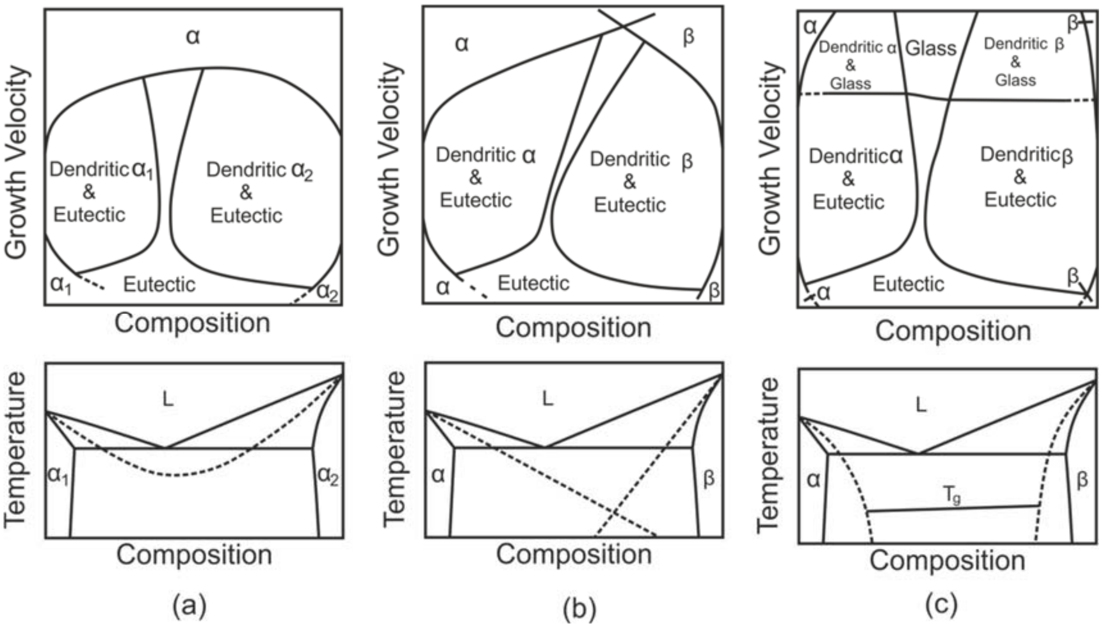

Figure 2.14 Solidification microstructures of three different types of eutectic systems, a) continuous T_0 curve; b) intersecting T_0 curves; c) non-intersecting T_0 curves, with glass transition (Boettinger, 1982).

Considering again a general eutectic alloy, a useful set of diagrams (see Figure 2.14) illustrate different types of solidification structures formed, as determined by composition and growth velocity (Boettinger, 1982). The three different possible types of eutectic systems are illustrated, and depending on the form of T_0, the location of the temperature-composition points at which the solid and liquid phase have the same free energy (dashed lines).

Each of the possible cases are described next (Jacobson and McKittrick, 1994, Boettinger, 1982):

- In the first case (Figure 2.14a), those eutectic alloys that have a continuous T_0 curve, the two solid phases present the same crystal structure (α_1 and α_2). These eutectic alloys usually present significant solid solubility. As shown on the diagram, at intermediate velocities dendritic α_1 and α_2 along eutectic forms. As the velocity increases, solute trapping occurs over the entire composition range forming a single-phase solid (α).

- For the second case (Figure 2.14b), those eutectic alloys in which the T_0 curves for each member intersect, the phase solids (α & β) have different crystal structures. At intermediate velocities the diagram shows a skewed coupled eutectic region towards phase β, which is observed because the β phase grows in faceted mode. As in the first case, at high velocities phases α and β, which are free of micro-segregation, form over the entire composition range.

- Those eutectic alloys in which the T_0 curves go downwards without intersecting are the third case (Figure 2.14c), in which the phase solids present (α & β) present very low solubility between each other. For this case, the glass transition temperature (T_g) is shown on the diagram, in which if the sufficient undercooling is applied a glass structure can be formed. As observed on the diagram, independently of the solidification velocity, at compositions near the eutectic crystalline phases does not nucleate forming a single-phase glass. Either side of the shown range, dendritic along eutectic or glass structures grow.

The latter diagrams usually are used to describe most of the rapidly solidified microstructures of general eutectic systems.

2.3 Simulation Techniques

In order to simulate accurately the SLM process, most of the parameters and characteristics involved in the process should be considered. In literature several FEM thermal models developed can be found (Roberts et al., 2009, Matsumoto et al., 2002, Gusarov and Smurov, 2010), in which a moving heat source model is considered, parametric studies were conducted and induced stresses due to thermal gradients were calculated. However, assumptions within the thermal models can be found in order to linearize some of the nonlinearities associated with the SLM process. Nevertheless, simulations of the microstructure evolution within metallic AM processes have been explored in limited occasions (Yin and Felicelli 2010) which used the finite element –

cellular automaton (CA-FE) model, described later on this section, in order to predict this evolution.

This section will discuss in detail, previously used simulation approaches and will highlight the strength and wakness points of each approach, as well as will highlight the current gap in knowledge which will be tackled in the present research.

2.3.1. Techniques used to simulate SLM and the Solidification Phenomenon

Multiscale modelling is generally employed to predict the microstructure evolution in materials, due to the large spatial and temporal spread of microstructural ingredients and the complexity of the phenomena (Raabe, 1998). In computational materials science, different simulation methods are used at different space and time scales, as shown in Figure 2.15.

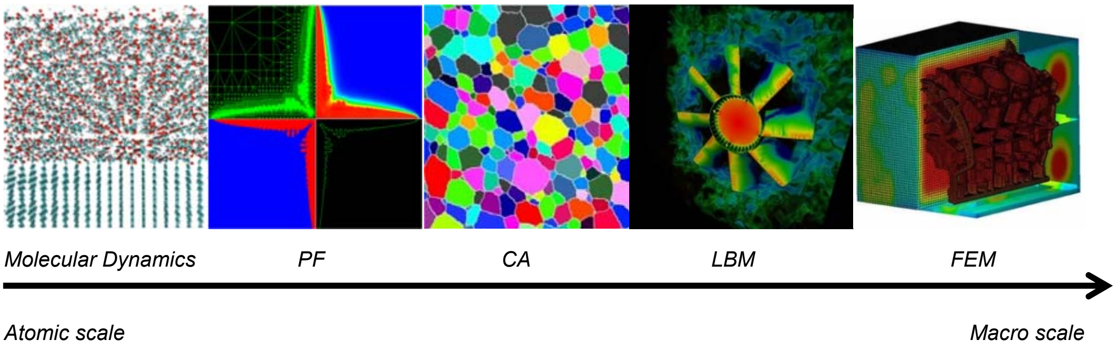

Figure 2.15 Multiscale modelling techniques scale representation.

As mentioned in Section 2.2, the microstructure formation of components produced by SLM is driven by rapid solidification and the simulation of this phenomena can be complicated. Limited studies (Tan et al., 2011) have been conducted in order to predict the formed microstructure in a similar process, laser welding, in which rapid solidification is sometimes present as well; this model utilises the cellular automata – phase field (CA-PF) technique in order to predict the dendritic growth. In the other hand, the simulation of the microstructural evolution during the solidification process that takes place on casting techniques have been developed widely ovev the years. These models have been developed using different simulation techniques such as FEM (Desbiolles et al., 1987, McCartney and Wills, 1988), CA (Kremeyer, 1998, Zhang and Zhang, 2006, Zhan et al., 2008, Tsai and Hwang, 2010), PF (Boettinger et al., 2002, Chen, 2002, Fallah et al., 2012), Monte Carlo (MC) (Das and Fan, 2004, Plapp and Karma, 2000, Koseki et al., 2003, Szpunar and Smith, 1996), and more recently the Lattice Boltzmann Method (LBM) (Semma et al., 2007, Semma et al., 2008); these models by its own had shown different strenghts and weaknesses in terms of the scale, accuracy and computing efficiency of the models, for this main reason a variety of couplings between the mentioned techniques have been explored. The most succesful coupling explored are: CA-FE (Gandin and Rappaz, 1994, Gandin and Rappaz, 1997, Gandin et al., 1999, Yin and Felicelli, 2010), PF-FE (Asle Zaeem et al., 2013, Zaeem et al., 2012), CA-PF (Tan et al., 2011), and CA-LBM (Yin et al., 2011, Eshraghi et al., 2012, Sun et al., 2011, Jelinek et al.). Each of these explored couplings aim to simulate a specific problem during the microstructural evolution of metallic components, a summary of how simulation techniques have been used to solve the solidification phenomenon of a determined manufacturing process is represented in Figure 2.16.

The SLM process is an AM process characterised for using a high powdered laser beam, which fuses metallic powder together in a layer-by-layer process. In literature, FEM has been widely used by researchers (Shiomi et al., 1999, Matsumoto et al., 2002, Guo-feng and Guang-nan, 2004, Roberts et al., 2009, Gusarov et al., 2007, Gusarov and Smurov, 2009, Gusarov and Smurov, 2010, Körner et al., 2011, Song et al., 2012, Safdar et al., 2013, Loh et al., 2015, Foroozmehr et al., 2016) in order to simulate the temperature profiles generated in this process. The most representative researches will be discussed in order to highlight the findings and weaknesses of each.

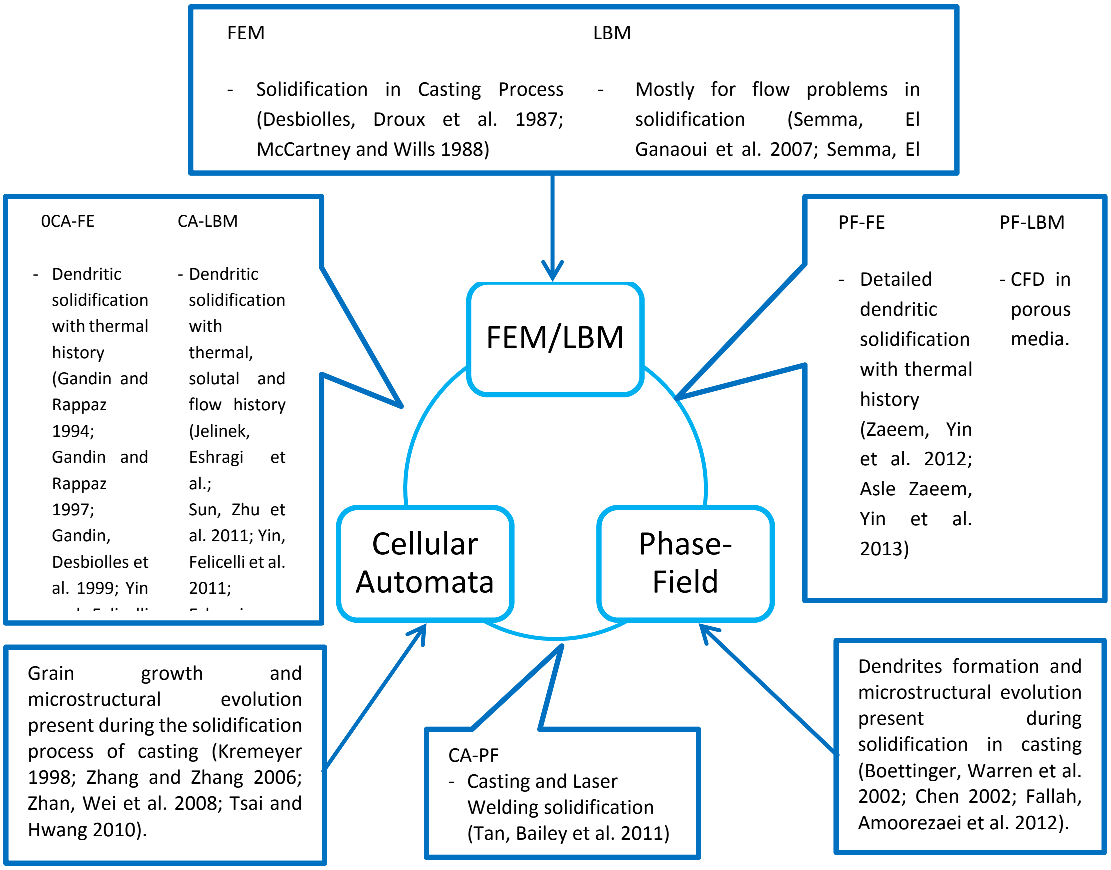

Figure 2.16 Different simulation techniques and how they have been used.

Shiomi et al. (1999) used FEM to clarify the forming mechanism in laser systems simulating the melting and solidifying process, the model was validated comparing the calculated weights of the solidified powder with experimental weights. The calculated weights agreed with the experimental weights, and it was determined that the maximum temperature reached by the system was affected by the peak laser power rather than the duration of the irradiated laser. However, this model was developed to simulate a single irradiation spot and detailed powder thermophysical properties were not used within the model.

Matsumoto et al. (2002) proposed a method for calculating the temperature distribution within a single metallic layer formed on a powder bed in SLM using FEM. The method computes the changes in properties from powder-to-liquid-to-solid and predicts a temperature profile which then is used to calculate the development of stress. However, the developed method does not consider the effect of a substrate plate underneath the powder bed, neither the absorption of the metallic powder, and the properties of the material used are not considered as thermal dependent. No experimental validation was performed, however, it is one of the first researches that manages to compute the change from powder-to-liquid-to-solid.

Roberts et al. (2009) developed a FEM simulation using the element birth and death technique in order to simulate the temperature profile generated by a laser irradiated into a powder bed for multiple layers. Detailed thermal conductivity of the powder bed was introduced in this research, however, the approach used is not as detailed as the approach proposed by Zehner and Schlunder (1970) and the mushy zone characteristics are ignored in all of the defined properties. The model was validate with experiments and provided a better understanding of the SLM process, however, a more detailed model is needed in order to compute the solidification phenomena involved within SLM.

Song et al. (2012) highlighted the importance of a SLM temperature distribution simulation in order to optimise processing parameters. Even though, basic thermal dependent properties were defined in the model and extremely high temperatures were predicted, the obtained results helped to fabricate a component with a desired degree of porosity. This research serves as an example of the importance of having a detailed FEM approach that accurately predicts the temperature profile generated, which can be used to optimise or predict the optimum processing parameters of a determined material.

Loh et al. (2015) developed a single layer FEM model that considers the powder-to-solid transition along with an effective method to achieve volume shrinkage and material removal. The developed FEM model considers a sacrifice layer (which is evaporated) in order to obtained the desired temperature profile and melt penetration. Volume shrinkage was valiadate with experiments, however, the assumptions made by this researchers limit the model to simulate a single layer of powder bed, not suitable for a real SLM process.

Recently Foroozmehr et al. (2016) developed a FEM approach to simulate the melt pool size during the SLM process, adopting the optical penetration depth of a laser beam (defined as the depth where the intensity of the laser energy reduced to 1/e of the intensity of the absorbed laser beam at the powder bed surface (Fischer et al., 2002)) into the powder bed and its dependecy on the powder size in definition of the heat sorce. The developed model considers a three-dimensional single layer powder bed, and defines with detail the thermal dependent properties of solid and powder (excluding mushy zone properties) in order to simulate the powder-to-liquid-to-solid transition. Experimental data was then used to calibrate the optical penetration depth in order to obtain more accurate results. The obtained results agreed with experiments, however, the interaction between layers was not studied.

In general terms, FEM has demonstrated to be a suitable technique to simulate the SLM process. From the FEM models studied, it was detected the need to consider the melt pool flow present in the melt, as well as detailed thermal dependent properties (which include the mushy zone) in order to accurately predict the temperature distributions present in the SLM process, as well as track the solidification phenomenon involved in the process. The present research will consider in detail the powder-to-liquid-to-solid transformation, with emphasis on the mushy zone properties, in aim to have a more detailed solidification model.

Simulating the microstructural evolution within a metallic AM process was explored by Yin and Felicelli (2010), using the Cellular Automata – Finite Element (CA-FE) coupling. This model described the formed dendritic structure during the solidification of a melt pool in the LENS (Laser-Engineered Net Shaping) deposition process. However, this model focuses on a small scale of a dendrite growth specifically at the boundary of a melt pool, and does not simulate the solidification process involved with the interaction of several melt pools or several layers.

Considering the background shown up to this point, it is well established that the CA-FE coupling is a suitable technique to simulate the microstructural evolution present in the SLM process. The present research will focus on developing a CA-FE coupling which will be able to predict the final microstructure of a component produced with the SLM process. FEM, CA, along with the CA-FE coupling will now be briefly described.

2.3.2. FEM

FEM is generally used to find the solution of a complicated problem replacing it with a simpler one (Rao, 2011). Replacing the actual problem with a simpler one then an approximate solution would be obtained rather than an exact solution. The solution regions is considered as a built up of many small, and interconnected sub-regions that are called finite elements, as shown in Figure 2.17.

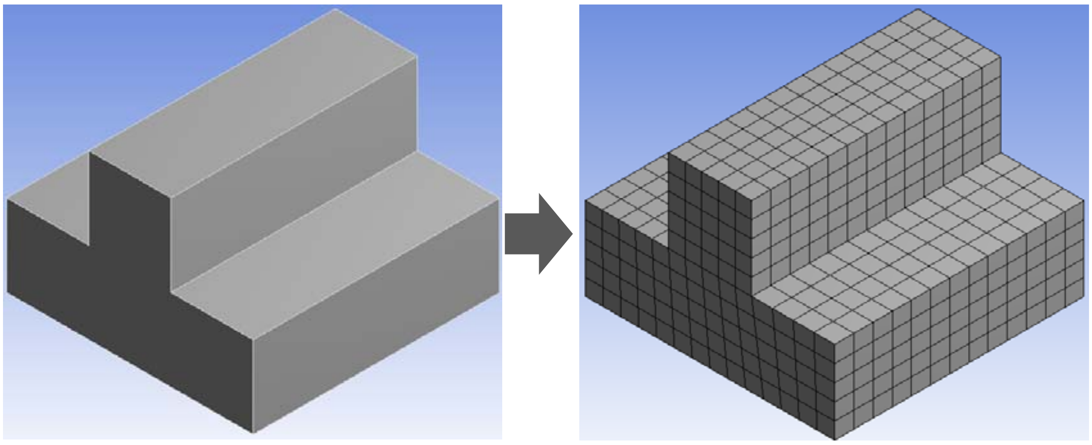

Figure 2.17 Finite elements representation.

This method has been extensively used in fields such as structural mechanics, heat conduction, fluid dynamics, etc. It has been established that the FEM can be used for the numerical solution of ordinary and partial differential equations and particularly to those involved in microstructural evolution (Frans et al., 2007).

In general terms, Rao (2011) describes that in the finite element method, the actual continuum or body of matter, is represented as an assemblage of subdivisions called finite elements (as shown in Figure 2.17). These elements are considered to be interconnected at specified joints called nodes or nodal points. The nodes usually lie on the element boundaries where adjacent elements are considered to be connected. Since the actual variation of the field variable (e.g., displacement, stress, temperature, pressure, or velocity) inside the continuum is not known, the variation of the field variables inside a finite element is assumed can be approximated by a simple function. The approximation functions (interpolation models) are defined in terms of the values of the field variables at the nodes. When field equation for the whole continuum are written, the new unknowns will be the nodal values of the field variable. By solving the finite element equations, which are generally in the form of matrix equations, the nodal values of the field variable will be known. Once these are known, the approximating functions define the field variable throughout the assemblage of elements.

2.3.3. CA

Cellular automata are algorithms that describe the discrete spatial and/or temporal evolution of different types of systems applying transformation rules to a regular grid of cells, also known as a lattice (Raabe, 2002). The lattice usually is defined in terms of a finite number of points, that can be related to the nodes of a finite difference field. The evolution of the CA takes place through the application of certain transformation rules (256 different rules (Wolfram, 2002)) that act on the state (on/off) of each node/cell. These rules determine the state of a node/cell as a function of its previous state and the state of the neighbouring nodes/cells. Usually CA evolves in discrete time steps, after each time interval the valies of the state variable are simultaneously updated for all nodes/cells.

A simplistic way to represent a two-dimensional CA is considering an infinite set of cells along with a defined set of transformation rules that would follow each of the cells. Each cell would have two possible states, on (black) or off (white). The neighbourhood of a cell is defined as the nearby or adjacent cells of the one of interest. The most common types of neighbourhoods that can be defined for each cell are the von Neuman neighbourhood and the Moore neighbourhood illustrated in Figure 2.18. The von Neumann neighbourhood consists of the four orthogonally adjacent cells to the one of interest, and the Moore neighbourhood consists of the von Neumann neighbourhood as well as the four remaining cell surrounding the cell of interest (Kier et al., 2005).

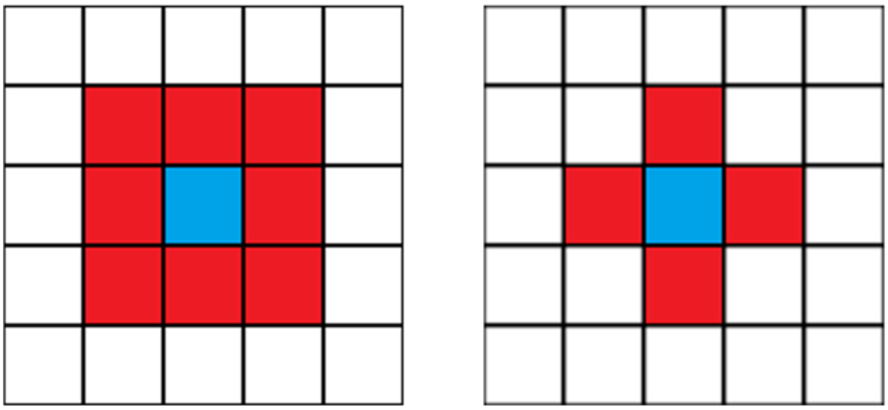

Figure 2.18 Moore and von Neumann neighbourhoods.

Generalized microstructure CA use a discrete spatial grid of cells or nodes, where space can be defined as real space values. The defined space usually is homogeneous throughout the lattice, where the transformation rule defined is the same everywhere. Usually every cell/node in the lattice would start with the same state value. Sometimes, it is assumed that the universe start out with a periodic or random pattern (nucleation). These cells will ten be updated in synchrony while the time steps increase.

As the CA is simulated on a finite lattice, in two dimensions the lattice would be represented in a form of a rectangle. This assumptions leads to the problem of how to handle the transformation rules along the cells/nodes on the edges of the lattice. The manner that the edges are handled will affect the values of all the cells in the lattice. One method of handling of these cells/nodes is consider that they would remain constant during all the algorithm, or another method is to define the transformation rules for the neighbours of the cells/nodes of the edges differently for all the other cells. These latter method would lead to fewer neighbours on those cells/nodes located on the edges. So depending on the local problem to solve, the most convenient method should be selected.

2.3.4. CA-FE

In the field of computational materials science, coupling modelling techniques such as CA-FE is having a huge momentum. These couplings are being used to predict the microstructure evolution under defined conditions. The main advantage of working with these couplings is having a more efficient computing performance and the ability to consider multiscale models, as shown in multiscale Figure 2.15, in the same calculations.

It is worth to mention that the CA method used on the CA-FE coupling, does not simulate the complex development of dendritic or eutectic patterns as other methods do (see Figure 2.15) (i.e. dendrite tip radius, microsegregation, secondary arms, etc.). This method instead, focuses on the simulation of the grain using simplified growth kinetic laws, and the inner solid-liquid mixture is then characterized by an internal volume fraction of solid.

The CA-FE method superimposes the FE mesh to the CA lattice, as shown in Figure 2.19. This superimposition is made in order to calculate and solve in a more efficient manner the conservation equations used at a bigger scale on FEM than the ones used to calculate the nucleation and growth kinetic laws in CA.

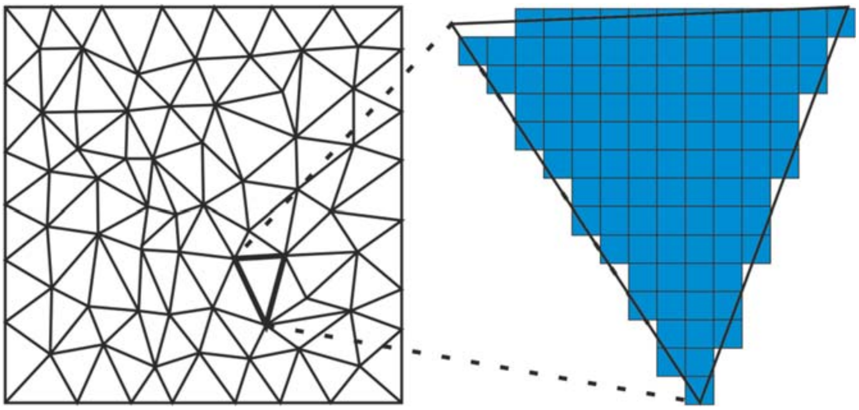

Figure 2.19 Schematic representation of a couple between CA and FE grids.

2.3.4.1. Nucleation Law

In the development of the CA-FE method, heterogeneous nucleation sites are considered, which can give rise to the nucleation events and they are randomly distributed among the cells/nodes of the solidifying domain. In order to identify the cells/nodes that belong to the bulk of the domain (volume) and those at the boundaries (surface) a reference index is used, which permits to identify the heterogeneous nucleation that happens on the bulk and on the surface of the domain. Therefore, with the definition of the reference index, different nucleation rules can be defined for the volume and surface of the domain. The location of each nucleation site is randomly selected through the algorithm. Each of the nucleation sites is characterized by the critical nucleation undercooling (ΔT^{nucl}). These undercoolings are assumed to follow a Gaussian distribution ($(dn/d(\Delta T))$), describing the density of the nucleation sites (dn), and becoming active in an undercooling increment ($d(\Delta T)$). Therefore, for the volume/surface of the solidifying domain, n is the density of grains that can possibly form up to an undercooling temperature (ΔT). This nucleation law require three main parameters in order to solve the calculations, the mean undercooling temperature (ΔT_N), the standard deviation (ΔT_σ), and the integral of the distribution (n_{max}) (Rappaz, 1989).

During the thermal calculations obtained with FEM, as soon as the local undercooling temperature ($\Delta \mathrm{T}_v^t$) at a given nucleation site location (v) becomes larger than the critical nucleation undercooling temperature associated with the nucleation site (ΔT_v^{nucl}), the nucleation event then takes place and a new grain will form with a random crystallographic orientation, this will only happen if the current state of the cell is liquid.

2.3.4.2. Growth Law

The growth of the newly nucleated grain is modelled using the rule 254 of the CA model, and it increases the size of the “grain”. The extension is then calculated by integrating over time the growth kinetics law of RS theory of the dendrite tips (Kurz et al., 1986). Once the “grain” is sufficiently large to capture the cell centre of one of its liquid neighbours, the state index of the current “grain” is then switched to that of the parent “grain”. If the “grain” is then fully surrounded by mushy cells, then it would no longer grow.

2.3.4.3. Coupling with FE

The local temperature or undercooling temperature of the cells calculated through FEM is a key parameter of the CA nucleation-growth algorithm. These temperatures have to be deduced from the solution of the average energy conservation equation, i.e., the heat flow equation averaged over the solid and liquid phases. The grid used to calculate the FEM solution usually is coarser than that of the CA cell size, however, some time it could be of the same size if the computing performance is not affected. The main objective of the coupling between CA and FE is to obtain the temperature variations and the volumes of solid fraction in order to use them as inputs in the nucleation-growth algorithm.

There are two coupling modes involved in the CA-FE method, the weak and the full coupling mode.

In the weak coupling mode, a unique solidification path ((e.g. the Gulliver-Scheil micro-segregation path (Kurz and Fisher, 1998)), can be used on the FEM macroscopic scale. The variation of the enthalpy becomes then a simple function of the temperature variation alone and the temperature field is directly solved on the macroscopic scale. Then the temperature dependent CA nucleation and growth rules defined above takes the value of temperature from the FE nodes at a certain time.

In the full coupling mode, the enthalpy variation at a cell location, as well as the explicit temperature are first interpolated from those calculated by FEM. The nucleation and growth algorithm can then calculate at the cell level the explicit temperatures. The variation of the solid fraction within each cell is then calculated using a truncated Gulliver-Scheil model (Gandin et al., 1999). Once the solid fraction is known, the variation of temperature can be calculated using the energy balance. This coupling mode allows the prediction of recalescence at specific locations of the solidifying domain.

2.3.4.4. Applications of CA-FE

Using the CA-FE coupling has some important advantages over other methods, such as the improved computing performance and multiscale modelling. It has been demonstrated that the CA-FE method is able to predict the microstructural evolution of real size casting parts, such as turbine blades, casting rods and pigtail selectors (Gandin et al., 1999) (see Figure 2.20); has predicted in micro scale the dendritic structures obtained with LENS processing (Yin and Felicelli, 2010) (see Figure 2.21); and more recently 3D simulations of CA-FE on aluminium alloy ingots have been developed (Carozzani et al., 2012) (see Figure 2.22).

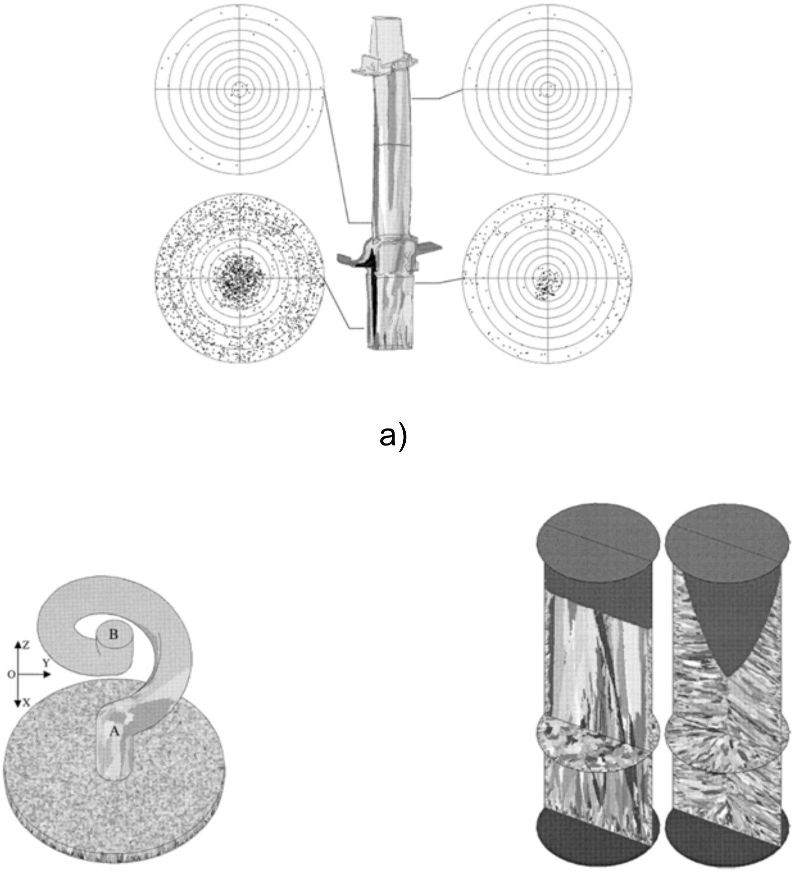

a)

b)

c)

Figure 2.20 a) A 3D view of the grain structure calculated for a turbine blade, b) A 3D computed columnar structure in a pigtail grain selector, c) Predicted 3D grain structure in continuously cast rods (Gandin et al., 1999).

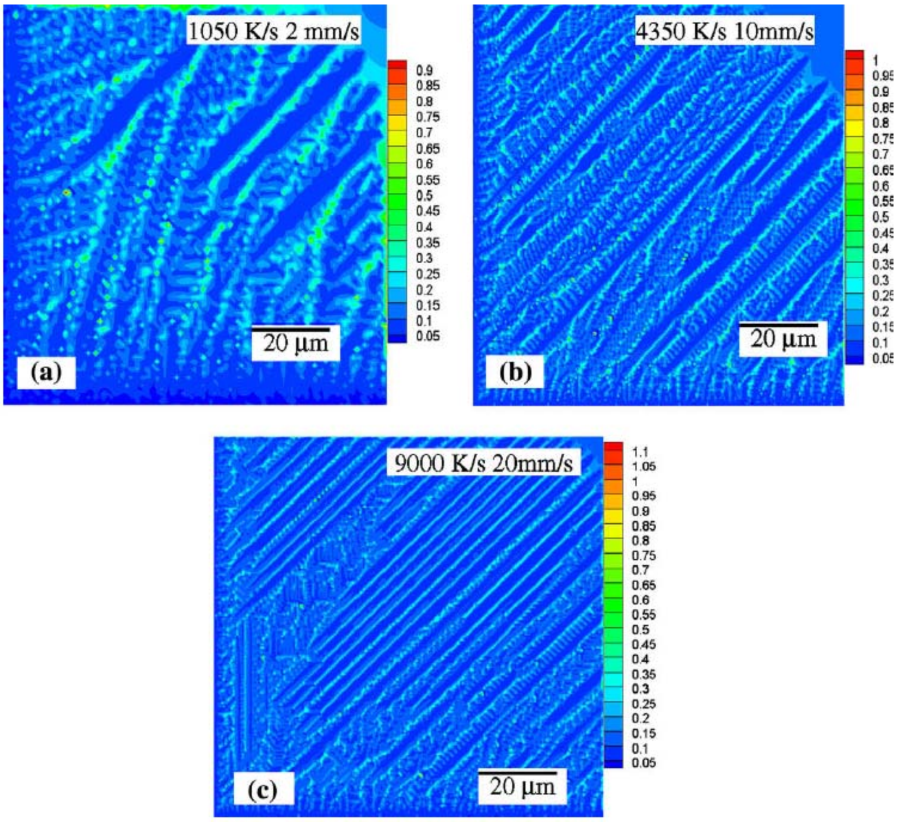

Figure 2.21 Simulated microstructure obtained during the solidification process of different laser moving speeds and cooling rates in the LENS process.

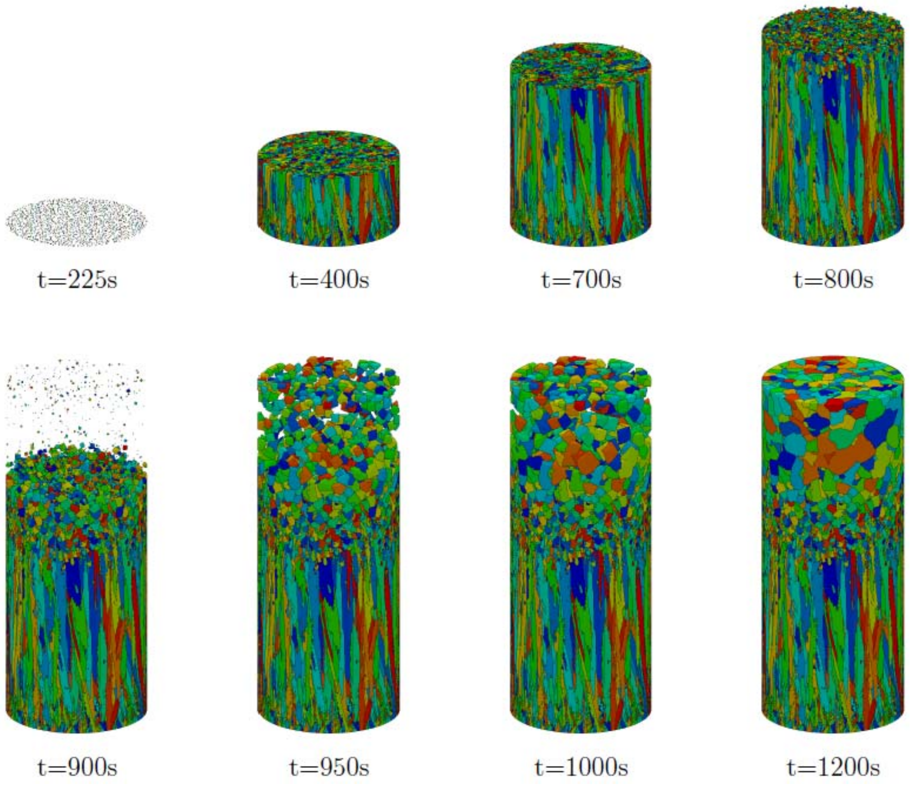

Figure 2.22 Modelled 3D Aluminium alloy (Al -7 wt% Si) microstructural evolution of the CET transition.

2.4 Summary

Along the present chapter a review of relevant academic work related to the undertaken research has been presented.

It was of great interest to have a deep understanding on the basics of the SLM process, so literature related to this process was presented and discussed on section 2.1. A high level of understanding of the conditions that affect the SLM process is found on literature. However, a gap in knowledge was identified when trying to understand the microstructural evolution within components manufactured via SLM. The present research focuses on covering this gap in knowledge by developing a tool that will help to understand with more detail this phenomenon.

Solidification theory is well-established, however, in section 2.2 the basics of solidification are studied in order to have a deep understanding of the development of microstructures within a component. Understanding the physical phenomena involved during the grain formation is of great importance to assist with the development of a numerical model capable of predicting this formation.

In order to develop a model capable of predicting both the temperature distributions in SLM and the microstructural evolution of processed components, different simulation techniques suitable for multi-scale modelling are reviewed in section 2.3. A brief summary of how different simulation techniques are used to solve the solidification phenomena was presented and it is clearly identified that researchers prefer using FEM and CA to model microstructural evolution. With this in consideration, an in depth analysis of how FEM is used to solve SLM related problems was performed and the need to have a detailed model which considers detailed material properties as well as the melt pool flow was identified. The present research will develop a model that includes the gaps found in the studied models in literature. A brief explanation of FEM, CA, and CA-FE was then presented, in order to get familiarised with those techniques.

Knowledge obtained from literature will be used in combination with knowledge generated in the present research to develop a tool which is capable of predicting the microstructural evolution of a component manufactured via SLM. The process followed for the creation of this tool will be described in subsequent Chapters.

3. Material Properties

While processing metallic components with AM technologies, such as SLM, the powder form material experiences a change of its state as it absorbs the energy from the laser. The state change involved during the process is powder-to-liquid-to-solid. In the present research these changes are accurately represented and described within the material properties, these properties are used to model these changes in a precise and accurate manner. Within this chapter the relevant material data for the numerical model developed is gathered, calculated and presented, as well as assumptions made for some of the properties.

3.1. Materials

The material of interest for the current research is Aluminium Alloy AA-2024. The material's thermophysical properties will be used in order to develop the models of the SLM process. Powder form of AA-2024 was obtained from a local powder supplier, LPW technologies. AA-2024 was selected due to its high concentration of copper, and due to its interest in industries such as aerospace. The chemical composition used in this work for AA-2024 is given in Table 3.1 (Mills, 2002).

Table 3.1 Composition of AA-2024 (mass %)

Al	Cr	Cu	Fe	Mg	Mn	Si	Ti	Zn
92.0	0.10	4.4	0.5	1.5	0.6	0.5	0.15	0.25

The thermo-physical properties of both solid and powders are described and defined in section 3.2 and 3.3 respectively.

3.2. Thermophysical Properties of Solids

During the development of the transient thermal analysis for the proposed models, temperature dependent physical properties (i.e. thermal conductivity, enthalpy and density) were taken into account. Temperature dependent properties and latent heat considerations implies a non-linear thermal analysis, as well as an approximation of the solidification involved in the process.

The thermophysical properties of the liquid phase are different from those of the solid phase (as shown in table 3.2) thus the value of the property (density, thermal conductivity, heat capacity, enthalpy of fusion, etc.), P_T, in the mushy region will be dependent upon the amount of liquid and solid. These values are calculated using (Equation 3.1 (Mills, 2002), where $f_{s(T)}$ is the fraction solid at T and P_{Tsol} and P_{Tliq} are the values of the property at the solidus temperature and the liquid at the liquidus temperature (fraction solid values obtained from (Mills, 2002)), respectively.

$$P_T = f_{s(T)} + \left(1 - f_{s(T)}\right) P_{Tliq} \qquad \text{(Equation 3.1)}$$

Equation 3.1 would also be used to calculate the mushy zone properties for the heat capacity, enthalpy of fusion and thermal conductivity.

The thermophysical properties of solid AA-2024 used on the present research (density, enthalpy, specific heat capacity and thermal conductivity), are those calculated by Mills (2002) which are listed in Table 3.2.

Table 3.2 Selected thermophysical properties of Solid AA-2024.

Temperature	*Density*	*Enthalpy*	*Specific Heat Capacity*	*Thermal Conductivity*
T(°C)	*ρ(kg/m^3)*	*H(J/g)*	*Cp(J/g*K)*	*K(W/m*K)*
25	2785	0	0.85	175
100	2770	66	0.9	185
200	2750	159	0.95	193
300	2730	255	0.97	193
400	2707	353	1	190
500	2683	457	1.08	188
538	2674	566	1.1	188
550	2653.12	614.48	1.1048	175.7
570	2644.42	634.68	1.1068	170.57
580	2639.2	646.8	1.108	167.5
600	2630.5	667	1.11	162.375
620	2587	768	1.12	136.75
632	2500	970	1.14	85.5
700	2480	1048	1.14	85
800	2452	1162	1.14	84

3.3 Thermophysical Properties of Powders

3.3.1 Bulk Density

The bulk density is a property of powders that is defined as the mass of many particles of the material divided by the total volume they occupy. It is not an intrinsic property, since it can change depending on how the material is handled. For the case of the present work the bulk density would be considered as “freely settled” since it is not going to be involved in any compaction or sintering process.

In order to determine the bulk density at room temperature of the metallic powders, a measuring cylinder of constant volume and a high precision measurement scale were used. A 50cm3 cylinder was filled with loose powder and its mass was measured.

The results of the mass measurements for AA-2024 were:

Powder mass (m_{pwd}) = 0.08016g
Powder volume (V_{pwd}) = 0.00000005m^3
Calculated density (ρ_{pwd}) = 1603.2kg/m^3
Density ratio (ρ_r) = 0.5756

The bulk density measurement obtained is for room temperature, but density is a thermophysical property so an interpolation of the variation with temperature was undertaken considering an increment of the bulk density of the powder with temperature until T$_{sol}$ is reached. The present research proposes (Equation 3.2 in order to describe the variation of bulk density with temperature below T$_{sol}$.

$$\rho_{pwd} = (4 \cdot 10^{-8}T^4) - (7 \cdot 10^{-5}T^3) + (0.0425T^2) - (10.964T) + 2580.5 \qquad \text{(Equation 3.2)}$$

Considering that the density of the powder at room temperature is ρ_{pwd}, and assuming that powder sinters at different rates as the temperature raises up to T_{sol}, the values shown in Figure 3.1 were proposed. Equation 3.2 was obtained from fitting an equation to the curve (between room temperature and T_{sol}) shown in Figure 3.1.

At T_{sol} the bulk density and the density of the solid material is equal. The mushy zone and liquid densities will be the same as the density of solid material for higher temperatures than T_{sol}. Figure 3.1 show the temperature dependence of the bulk density.

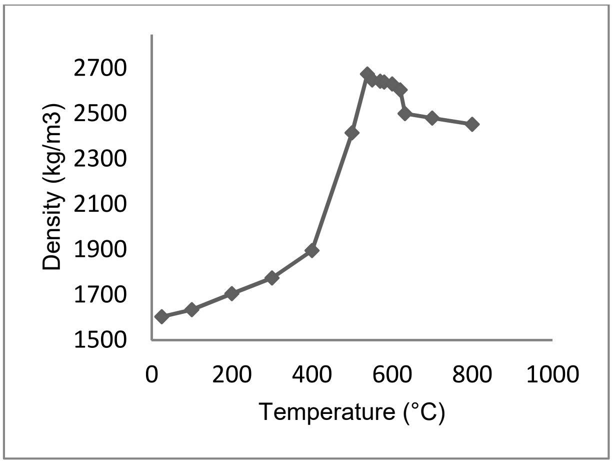

Figure 3.1 Calculated temperature dependence of bulk density for AA-2024.

The mushy zone and liquid values for bulk density are equal to those of the solid density. Above the melting point and up to the upper limit temperature, it is assumed that the density varies linearly with temperature.

3.3.2 Enthalpy of Metallic Powders

In order to describe the enthalpy of powders, the volumetric enthalpy is used. The volumetric enthalpy expresses the relationship between the enthalpy changes in solid and powder state, as seen in (Equation 3.3).

$$\Delta H_p = \rho_r \Delta H_s \qquad \text{(Equation 3.3)}$$

where ΔH_s is the change of enthalpy for the solid material and ρ_r is the density ratio presented in section 3.3.1. Figure 3.2 show the temperature dependence of the volumetric enthalpy of the powder used.

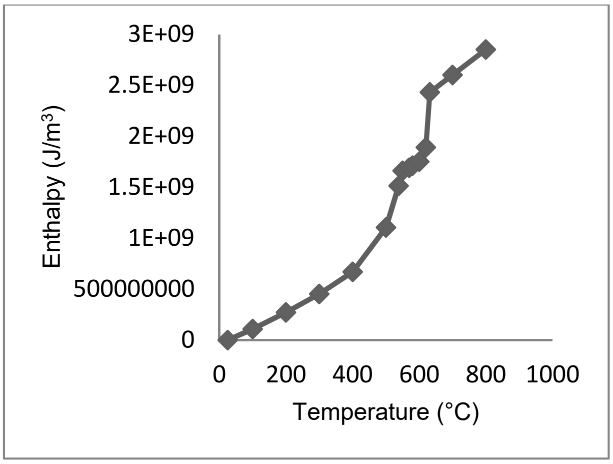

Figure 3.2 Temperature dependence of volumetric enthalpy of powder for AA-2024

The mushy zone and liquid values for the volumetric enthalpy are equal to those of the solid state enthalpy. For temperatures higher than the melting point, it is assumed that the density varies linearly with temperature.

In the case of specific heat capacity, the property does not change with porosity, since this property is intrinsic to the type of material. Therefore, no assumptions are made for the specific heat capacity of powders.

3.3.3 Thermal Conductivity of Metallic Powders

The thermal conductivity of a material is defined as the amount of heat that crosses a unit of area of the material per time per temperature gradient (Loeb, 1954). In porous materials, heat propagates by three processes: (1) thermal conductance through the solid; (2) radiation through pores and (3) convection through pores. In a similar manner the principal mechanisms of heat transfer in powders are (Luikov, 1971): (1) thermal conduction in gas filling the pores; (2) radiation through the pores and (3) thermal conduction through the contacts between the particles.

In the scope of this work the powder is considered as a “porous” media, therefore the thermal conductivity is estimated using two different approaches.

The first approach is using the relationship shown in (Equation 3.4) (Loeb, 1954).

$$K_{pwd} = K_s(1 - P) \tag{Equation 3.4}$$

where P is the porosity and K_s is the thermal conductivity of the solid state. This relation assumes a solid matrix phase continuous, isometric pores and regular distribution of pores. The temperature dependence of the estimated values of thermal conductivity are shown in Figure 3.3

The second approach is using the relationship shown in Equation 3.5 (Zehner and Schlunder, 1970).

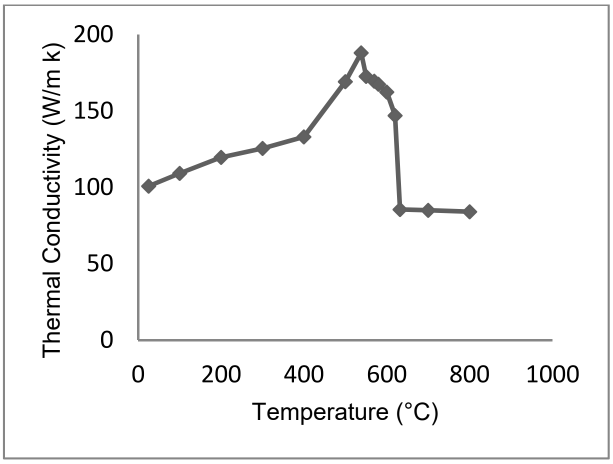

Figure 3.3. Temperature dependence of the thermal conductivity of powders for AA-2024 using first approach.

$$
\begin{aligned}
\frac{K_{pwd}}{K_g} = {} & \left[\left(1-\sqrt{1-P}\right)\left(1+P\frac{K_r}{K_g}\right)\right] \\
& + \left(\sqrt{1-P}\right)\Big\langle\Big(1 \\
& - \psi\Big)\left\{\left(\frac{2}{1-\frac{BK_g}{K_s}}\right)\left[\left(\frac{B}{\left(1-\frac{BK_g}{K_s}\right)^2}\right)\left(1-\frac{K_g}{K_s}\right)\left(\ln\left(\frac{K_s}{BK_g}\right)\right)\right.\right. \\
& \left.\left. - \left(\frac{B-1}{2}\right) - \left(\frac{B-1}{1-\frac{BK_g}{K_s}}\right)\right] + \left(\psi\frac{K_s}{K_g}\right)\right\}\Big\rangle
\end{aligned}
\qquad \text{(Equation 3.5)}
$$

Where,

K_{pwd} = effective thermal conductivity of the powder bed, W/m*K.

K_g = thermal conductivity of the gas inside the pores of the powder bed, W/m*K.

K_s = thermal conductivity of the solid material, W/m*K

P = porosity of the powder bed.

K_r = thermal conductivity of the powder bed owing to radiation, W/m*K.

Ψ = flattened surface fraction of the particle in contact with another particle; 0 when there is no contact between the particles, and 1 when there is complete particle contact.

B = deformation parameter of the particle, 1 for spheres.

Adopting a predictive model for computing the effective material properties of the powder bed (Sih and Barlow, 1994), K_r is calculated using the effective emissivity of the powder bed.

The effective emissivity of the powder bed (ε_{pwd}) is described as the combination of both the emissivity of particles and cavities in the powder bed, and can be defined with Equation 3.6.

$$\varepsilon_{pwd} = A_h\varepsilon_h + (1 - A_h)\varepsilon_s \qquad \text{(Equation 3.6)}$$

Where, ε_s is the emissivity of the bulk material, ε_h the emissivity of the cavities (defined by Equation 3.7) and A_h is the area fraction of the surface occupied by the cavities (defined by Equation 3.8).

$$A_h = \frac{0.908P}{1.908P^2 - 2P + 1} \qquad \text{(Equation 3.7)}$$

$$\varepsilon_h = \frac{\varepsilon_s\left[2 + 3.082\left(\frac{1-P}{P}\right)^2\right]}{\varepsilon_s\left[1 + 3.082\left(\frac{1-P}{P}\right)^2\right] + 1} \qquad \text{(Equation 3.8)}$$

Using the calculated effective emissivity of the powder bed, now K_r can be defined using Equation 3.9 (Mohanty and Hattel, 2014).

$$K_r = \frac{4\varepsilon_{pwd}\sigma T_p^3 D_p}{1 - 0.132\varepsilon_{pwd}} \qquad \text{(Equation 3.9)}$$

Where σ is the Stefan-Boltzmann constant, T_p is the mean absolute temperature and D_p is the mean diameter of the powder particles.

Using Equation 3.5, the thermal conductivity values for AA-2024 are calculated and plotted in Figure 3.4.

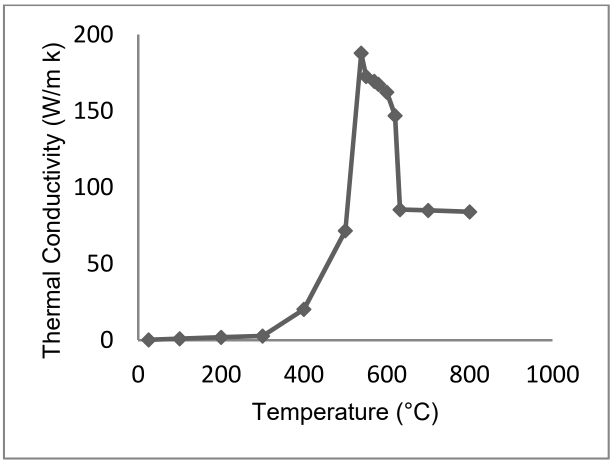

Figure 3.4 Temperature dependence of the thermal conductivity of powders for AA-2024 using second approach.

The mushy zone and liquid values for the thermal conductivity of powders calculated using both approaches are equal to those of the solid state thermal conductivity. Above the melting point and up to the upper limit temperature, it is assumed that the density varies linearly with temperature.

3.4 Summary of Selected Material Properties for the Numerical Model

A summary of the material properties used in the numerical model is presented in this section. The temperatures and properties selected include the key transitions to be modelled in order to provide a more detailed and accurate model. The values for intermediate temperatures for each of the properties are extrapolated directly within Ansys.

Detailed thermophysical material properties used in the numerical model have been presented and described in this chapter. The importance of such detail on each of the properties would have an impact on the model due to the non-linear behaviours experienced during the SLM processing of metallic components. The detailed thermophysical properties for solid AA-2024 used in the present research were listed in Table 3.2, and in Table 3.3 for powdered AA-2024.

Table 3.3 Selected thermophysical properties of Powder form AA-2024.

Tempera-ture	*Density*	*Enthalpy*	*Specific Heat Capacity*	*Thermal Conductivity First Approach*	*Thermal Conductivity Second Approach*
T(°C)	*ρ(kg/m^3)*	*H(J/m^3)*	*Cp(J/g*K)*	*K(W/m*K)*	*K(W/m*K)*
25	1603.2	0	0.85	100.747	0.2268
100	1634.3	1.08×10^8	0.9	109.157	0.9926
200	1705	2.71×10^8	0.95	119.666	1.8550
300	1774.5	4.52×10^8	0.97	125.456	2.7171
400	1894.9	6.69×10^8	1	133.005	20.2713
500	2414.7	1.1×10^9	1.08	169.201	71.6698
538	2674	1.51×10^9	1.1	188	188
550	2653.12	1.66×10^9	1.1048	175.7	175.7
570	2644.42	1.69×10^9	1.1068	170.57	170.57
580	2639.2	1.71×10^9	1.108	167.5	167.5
600	2630.5	1.75×10^9	1.11	162.375	162.375
620	2587	1.89×10^9	1.12	136.75	136.75
632	2500	2.43×10^9	1.14	85.5	85.5
700	2480	2.60×10^9	1.14	85	85
800	2452	2.85×10^9	1.14	84	84

4. Numerical Model

The numerical models developed within the present research will be detailed and described in the present chapter. Validations performed to the final models will be undertaken and discussed in Chapter 6.

The scope of the research presented was to develop an accurate and versatile numerical model detailing microstructural evolution within the SLM process. The model due to its complexity would be developed in a two-dimensional system, with possibilities of expanding the model to three-dimensions. The model would take into account the known material behaviours and the SLM process parameters in order to compute the thermal history and the grain growth within a defined sample. The defined sample selected for this case was a simple rectangular geometry in order to reduce the complexity that a freeform geometry could input to the numerical model.

Several numerical models were developed at different stages of this research, each of these models are interconnected at later stages. The stages in which the models were developed are mentioned:

- Single Layer Thermal Model (2D FEM)
- Layer by Layer Thermal Model (2D FEM)
- Microstructural Evolution (2D CA-FE)

FEM was used to model a whole layer of powder laying on top of a solid substrate in 2D, the results obtained will be discussed in section 4.1. The next step was to introduce the layer by layer model which is described and discussed in section 4.2. Finally, the last obtained results were coupled with CA in order to simulate the microstructural evolution based on the thermal history of the SLM process.

The FEM numerical models were developed under ANSYS Mechanical along with APDL (ANSYS Parametric Design Language) in order to automate common tasks and build the model in terms of parameters. Both programs are capable of calculating the nodal temperatures, track the solidification fronts at various times and both are easy to manipulate in order to change the process parameters. For CA, a C++ self-developed code is used to calculate the grain growth dependent of the thermal history obtained with FEM. The results of FEM are exported through a text file and then imported, read and superposed to the CA mesh in order to obtain the expected results. More details of each of the mentioned models are to be discussed in this chapter.

4.1 Single Layer Temperature Model (FEM) for AA-2024

This section will focus on the development of a single layer (multiple spots) FEM model. The model to be developed will be capable to predict the temperature distribution along the powder bed in 2D (single line on a single layer). In order to resemble the simulation to the actual SLM process, some additions to the algorithm will be made, i.e. a substrate plate will be considered. At the end of the section, the results of the developed model will be discussed and analysed in more detail, in order to introduce to the next developed algorithm. Next a description of the development of the model will be made.

4.1.1 Setup of the 2D single layer model

The single layer model will be treated as a transient thermal analysis, in order to capture with detail, the temperature profiles at each simulated spot. In the model a single laser spot (considered as a heat source) will irradiate a defined region (defined by the laser diameter, D) for a determined time (given by the Exposure Time, ET). Once the time is completed the heat source then moves to the next adjacent spot (which position is determined by the Point Distance, PD). Figure 4.1 illustrates the PD parameter.

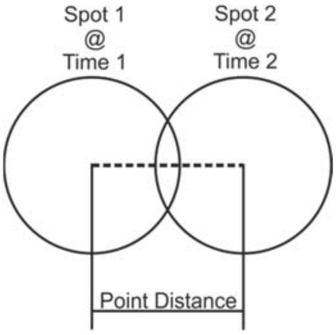

Figure 4.1. Point distance parameter

Normally the geometry of the laser spot is considered as a circle in a normal 3D space, however as the simulation developed in this section is in 2D, the laser spot is represented as a single line, since a single line represents the 2D projection of a circle, in which the laser spot diameter is equivalent to the length of the line.

The ambient temperature and the initial temperature of the powder bed were considered as 25°C. The laser spot diameter for the Renishaw AM125 (SLM system used for this research) is reported by the manufacturer to be 35μm. However, a 50μm diameter spot is simulated; this value was obtained from a measurement performed to the laser spot of the Renishaw SLM system with a Spiricon Laser Beam Analyser, the obtained results are shown in Appendix 6. The SLM of interest is equipped with an Ytterbium doped fibre-laser with an approximate wavelength of 1070 ±10nm, However, for the specific case of the present research a 1060nm wavelength is considered, due to valuable information found in literature for this specific wavelength (Shen et al., 2001). The absorptivity of aluminium powder to a wavelength of 1060nm according to Shen et al. (2001) is of 0.0588 for solid state and 0.064 for liquid state. In the scope of the present work, the absorptivity value for both solid and liquid state will be considered by rounding the value of both absorptivities to the closest integer for simplification, 0.06.

In order to determine the optimum mesh size for the present model, a mesh sensitivity study in the powder layer was conducted (shown in Figure 4.2).

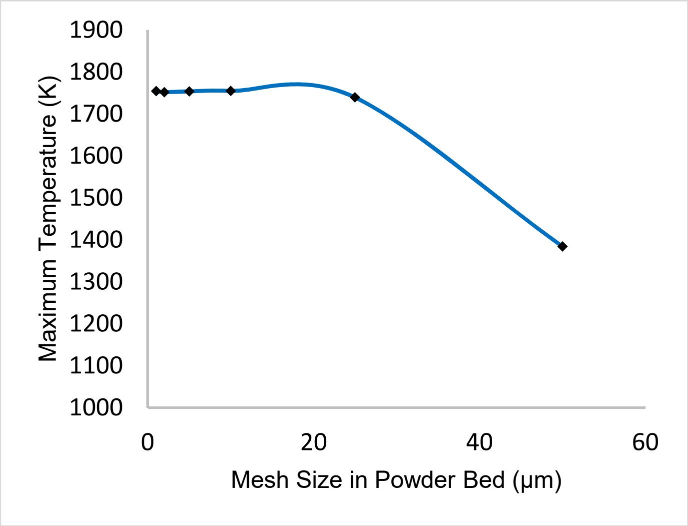

Figure 4.2 Mesh sensitivity study

From the convergence study performed (shown in Figure 4.2), it was determined that for the case of powders with particle size of approximately 50µm, the optimum ratio of particle size vs element size is of 5:1. If the element size of the powder bed is in agreement with the determined ratio, the simulation will give reliable results of predicted temperatures.

The mesh used to solve the desired calculations is showed in Figure 4.3. The dimensions of the model are: 50µm of thickness x 10cm of width for the powder bed and 1x10cm for the substrate plate.

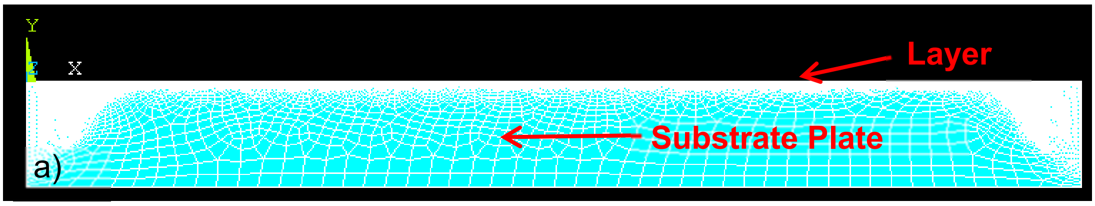

Figure 4.3. Meshed geometry for FEM of the 2D single layer temperature distribution model.

The mesh was constructed using PLANE 77 thermal elements. As observed in Figure 4.3 the deposited layer have a finer mesh compared to the rest of the model, this refinement was undertaken in order to capture accurately the thermal distribution in the area of interest around the melt pools. The contact area between the layer of powder and the solid substrate is considered as "perfect", in order to simplify the model.

Table 4.1 Process parameters for 2D single line model.

LP	143W
ET	450μs
LD	50μm
Recoating Time (Tr)	12s
PD	25μm
Ab	0.06
T_{sol}	811K
T_{liq}	905K
T_{amb}	298K
ρ	For powder see Table 3.3. For solid see Table 3.2.
Cp	For powder see Table 3.3. For solid see Table 3.2.
K	For powder see Table 3.3. For solid see Table 3.2.
hc	20W/m^2-K

Table 4.1 shows the process parameters used to calculate the temperature distribution of several laser spots irradiated onto a single layer of powder are enlisted.

According to Safdar et al. (2013) in order to artificially simulate the melt pool flow in SLM with FEM an anisotropic enhanced thermal conductivity approach should be used. This approach is defined by Equation 4.1.

$$K_{ii}'' = \alpha_{ii}'' K \qquad \textit{Equation 4.1}$$

where K is the normal isotropic thermal conductivity value at a certain temperature, ii represent the spatial co-ordinate and α_{ii} is the anisotropic enhancement factor for the respective spatial co-ordinate, which is defined as:

$$\alpha_{ii} = \begin{cases} 1 & if\ T < T_{liq} \wedge T_{sol} \\ Multiplying\ factor & if\ T > T_{liq} \end{cases}$$

The anisotropic enhancement factors considered in this model are the following: α_{xx}=3.0 and α_{yy}=1.5 in both solid and powder, this values were obtained from trial and error in order to obtain the desired melt pool dimensions.

The number of spots to be simulated was selected arbitrarily as 120. This number of spots was selected thinking that after a certain number of spots (less than the 120 defined spots) the maximum reached temperature and melt pool size will reach its maximum value. However, this will be analysed later on the chapter.

A boundary condition of natural convection is applied to the exposed top surface, in order to simulate the flow of inert gas through the powder bed that actually happens during the processing of metals in SLM. In this model a T_r is introduced, generally during the deposition of layers within the SLM system a time lapse in which a new layer is deposited is present. During this time lapse the top layer is exposed to the flow if inert gas that is present on the chamber. This time was measured on the Renishaw's SLM system and it is established within the model to be 12s. A convection boundary condition is applied on the top surface of the model for 12s before the scanning strategy initiates. The model is considered as transient and uses the full Newton-Raphson solver to implicitly solve the stiffness matrix values of the dynamic analysis in Ansys.

As introduced in section 4.1, the powder-melting-solidification method is used in the model in order to update the material properties during the calculation of the temperature distribution along the powder bed. The algorithm followed by the single layer models can be found in Figure 1 in Appendix 1.

The model developed will describe and predict the temperature profiles generated by a laser spot moving through a powder bed, mimicking the creation of 2D solid lines. The movement of the laser along the powder bed is considered within the algorithm of the developed model and considers the irradiation of the laser beam on a determined surface, defined by the diameter of the laser beam. The irradiation of the laser beam stays at the same spot for a defined time, which is defined by the ET; once this time is reached the laser beam will move of position by a PD in order to irradiate the next spot. This process is repeated until it reaches the defined number of spots and hatches.

In the next section, some results obtained with the described model will be presented and further analysis of the results will be undertaken.

4.1.2 Results and Discussion of the 2D FEM single layer model

Once the model has been set up just as described in section 4.2.1, the calculations were performed. The predicted temperature profiles of a single line on a single layer are shown in Figure 4.4.

According to the calculations performed by the single layer model after processing the irradiation of 120 spots in a single layer of powder on a solid substrate of the same material as the powder the temperature reached is of 1723.64K. The maximum predicted temperature after the 120 spots clearly is above the melting point of AA-2024, therefore a melt pool with certain dimensions is expected.

If an analysis of the evolution of the melt pool is undertaken, it can be observed that the melt pool appears since the very beginning of the process, as shown in Figure 4.5. However evolution of the predicted temperatures and melt pool will happen as observed on the final irradiated spot in Figure 4.4.

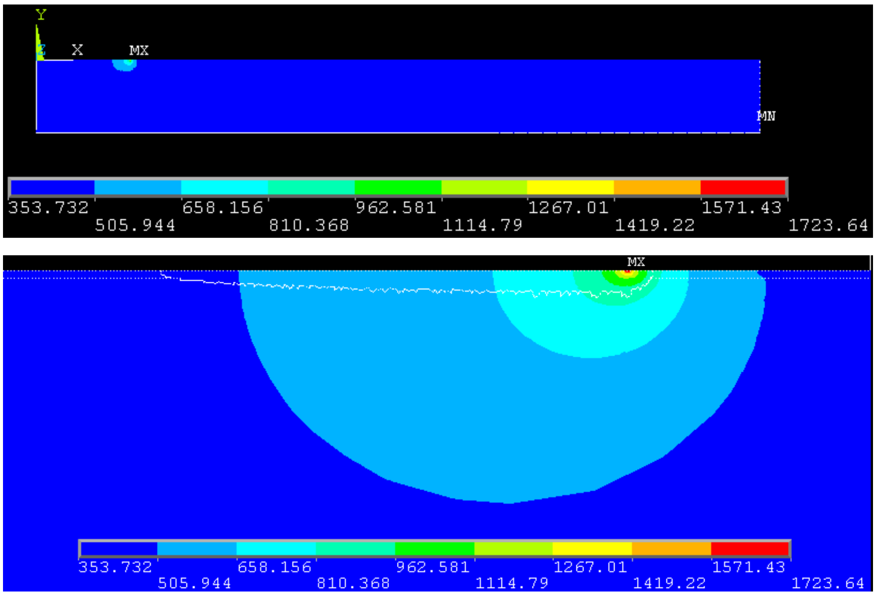

Figure 4.4. Predicted temperature distribution of a single line on a single layer.

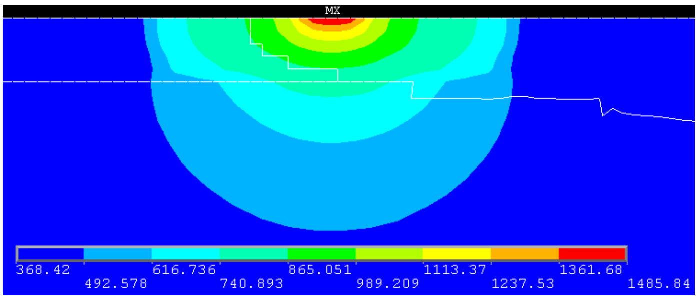

Figure 4.5 Temperature profile of the irradiation of the first spot.

The melt pool evolution through time along the processed line is represented in Figure 4.6. This evolution is represented in periods of 20 spots in order to make further analysis.

Examining with detail the evolution of the temperature distribution in process shown in Figure 4.6 it is determined that after the irradiation of 120 laser spots the temperature continues to increase so hypothetically the melt pool size is increasing as well. However, if the maximum temperature reached at each irradiated laser spot is plotted (see Figure 4.7), it is observed how the maximum temperature commence to stabilise as more spots are irradiated. It can also be noted that temperature increases and decreases each spot by an average of 125K, this difference can be attributed to both the error of the simulation and how heat dissipated through the whole system. In Figure 4.7

the red dots represent the maximum temperature reached per spot, meanwhile the solid line represent the mean value obtained.

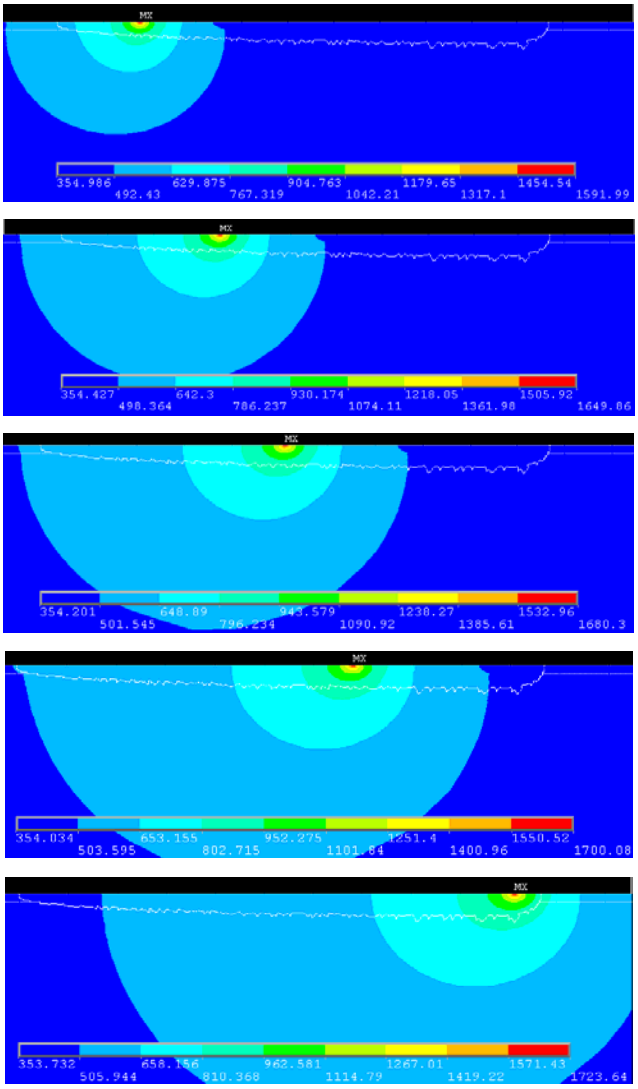

Figure 4.6. Melt pool evolution every 20 spots.

Next a similar analysis is performed to the evolution of the dimensions of the melt pool (see Figure 4.8), in which the dots/triangles represent the maximum values obtained at a randomly defined spot and the solid lines represent the obtained mean value.

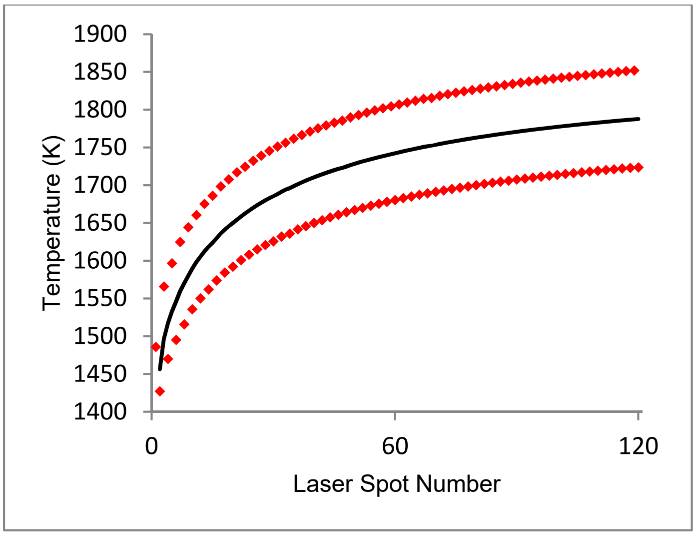

Figure 4.7. Maximum temperature reached at each irradiated laser spot.

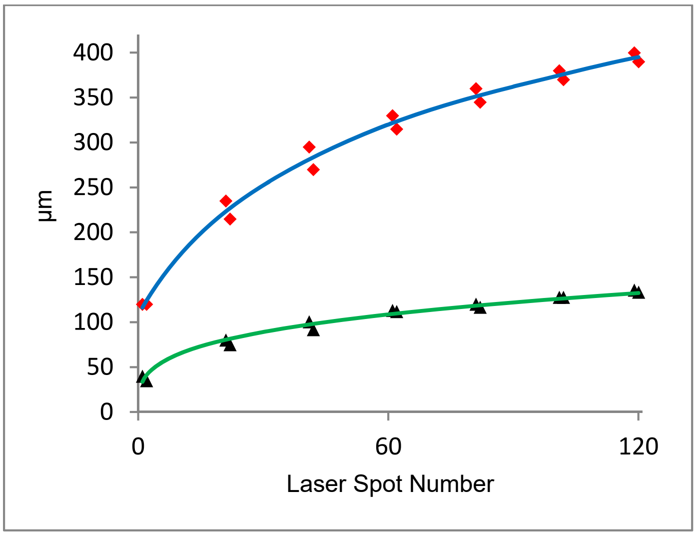

Figure 4.8. Melt pool diameter and depth evolution.

The dimensions of the melt pool increases as assumed before, however, the rate of increase of the melt pool diameter is higher than the melt pool depth. The melt pool depth seems to be stabilising after 120 irradiated spots, in contrast to the diameter. The variation from spot from spot perceived in the temperature profile can be reflected in the dimensions as well, so the melt pool is increasing and decreasing its size as the laser moves. This phenomenon can also be attributed to both the error present in the simulation and the heat dissipation present within the process.

Assuming that both the temperature profile and the melt pool dimensions will stabilize after the 120 irradiates laser spots, the melt pool obtained on the last irradiated spot can then be measured (Figure 4.9).

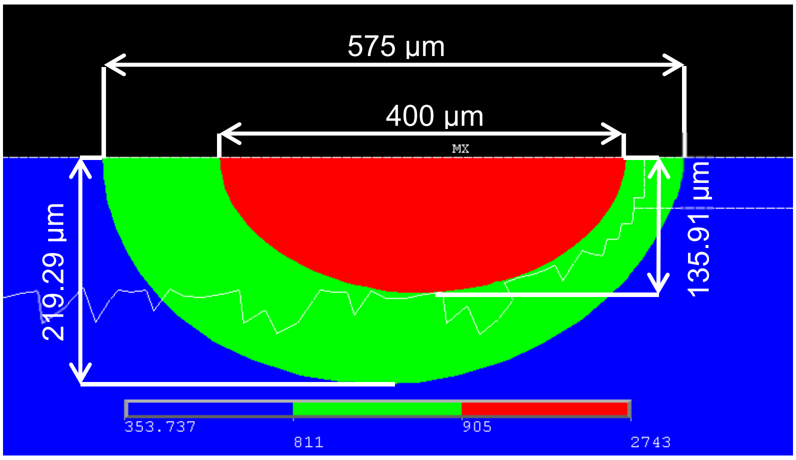

Figure 4.9. Maximum Predicted melt pool size and HAZ.

This data along with experimental data will be analysed in Chapter 6 in order to validate experimentally the produced model.

As the developed model is transient, several points along the powder bed can be monitored in order to determine their thermal history, as shown in Figure 4.10.

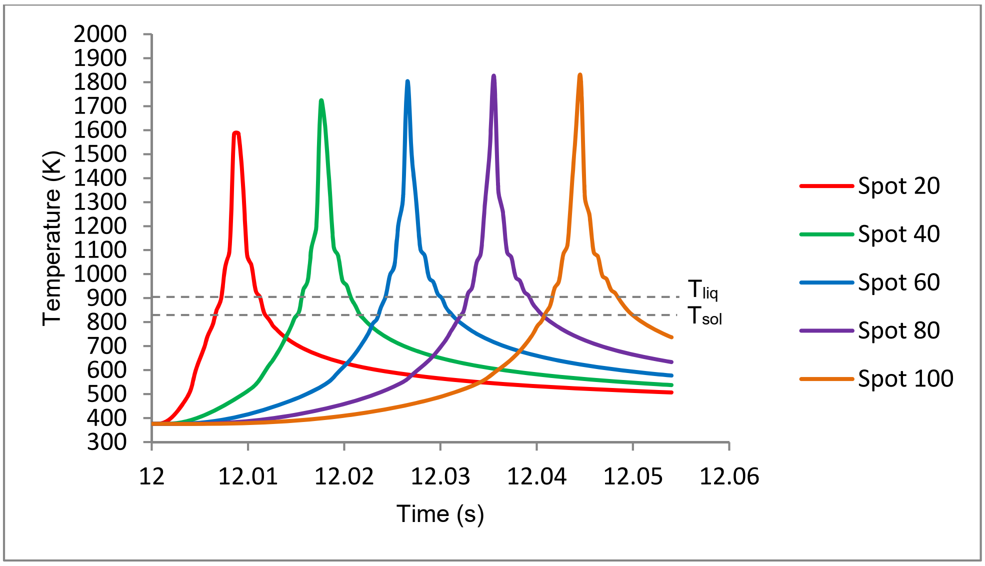

Figure 4.10. Temperature history of several points within the powder bed.

The data obtained in Figure 4.10 can be used to calculate the cooling rates at which the material is exposed. The rate is calculated between the T_{liq} and T_{sol}, this is undertaken in order to obtain the solidification time since the theoretically solidification occurs in that range of temperatures. The calculated cooling rates for the plotted spots are shown in Table 4.2. From the developed model the solidification rate and the thermal gradient in the liquid can be extracted as well. The solidification phenomenon occurs in the trailing edge of the melt pool due to the movement of the laser; the average solidification rate is calculated and enlisted in Table 4.2.

Table 4.2 Calculated cooling and solidification rates

Spot Number	Average cooling rate before T_{liq} (K/s)	Average cooling rate between T_{liq} & T_{sol} (K/s)	Solidification rate (K/m)	Thermal gradient in the liquid (K/m)
20	3.6×10^5	9.9×10^4	1.88×10^6	3.5×10^6
40	2.81×10^5	6.4×10^4	1.17×10^6	3.5×10^6
60	2.80×10^5	6.1×10^4	1.04×10^6	3.5×10^6
80	2.85×10^5	4.3×10^4	8.9×10^5	3.5×10^6
100	2.50×10^5	4.2×10^4	7.8×10^5	3.5×10^6
Average	2.91×10^5	6.01×10^4	1.15×10^6	3.5×10^6

The values enlisted in Table 4.2 are useful in order to determine the type of microstructure that will be obtained during SLM. The data obtained from the model determines that the average cooling rate associated with the SLM of AA-2024 is in the order of 10^5 K/s, and according to Jacobson and McKittrick (1994) Rapid Solidification Processing (RSP) estimated cooling rates are in the range of 10^5 to 10^6K/s. The solidification conditions on a similar process to SLM, laser surface processing, are outlined by Kurz and Trivedi (1994). In RSP the most important variable is the interface growth rate (V), in contrast the thermal gradient in the liquid ahead of the solid-liquid interface (G) plays a less important role in the microstructure selection processes. Other important variables are the cooling rate ($|\dot{T}|$=dT/dt, in directional growth is equal to GV) and the G/V ratio which controls the stability of the planar interface at low rates. Kurz and Trivedi (1994) determined that the solidification conditions for laser processing will, in most of the cases, lead to a columnar (directional) growth (see Figure 4.11).

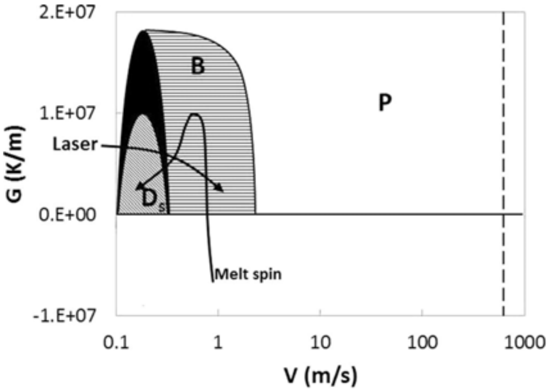

Figure 4.11. G-V microstructure selection map. Columnar growth is indicated by D_s, banded structure B and planar structure P (Harrison et al., 2015).

Using the calculated values from the model to calculate the value of V, it is also determined that the resulting microstructure for the present model will lead to a columnar growth of dendrites.

The values estimated up to this point can be overestimated, due to the considerations and assumptions (absorptivity value, powder modelled as continuous media, two-dimensional model, etc.) made within the model. However, in general terms the obtained information is in good agreement with theory as discussed before.

The next stage is to develop a layer-by-layer model that should be able to represent and estimate accurately the SLM process as by nature is a layer-by-layer process. The model developed in the present section will be used as a base in the layer-by-layer model which will be described in the next section.

4.2 Layer by Layer Model (FEM) for AA-2024

The analysis performed in section 4.2 lays as a basis on the development of the 2D layer-by-layer model developed in the present section. The data that will be obtained in this section will be used as input data in the CA microstructural evolution model. The developed numerical model mimics the SLM process operation in terms of a moving laser beam, material addition in form of powder layers, recoating time, air flow, etc., capturing as many variables as possible in order to maintain realistic results. The temperature profiles obtained within this stage are then going to be treated as response variables for the microstructural evolution model.

4.2.1 Setup of the 2D layer-by-layer model

Taking as a base the model developed in section 4.2 the element birth and death technique is introduced to the algorithm. The element birth and death considers that certain elements in the model may become “existent” or “non-existent”, so this option is used to deactivate and reactivate selected elements. This technique is applied within the model in order to mimic the deposition of powder layers by deactivating and activating the corresponding elements within the mesh.

In order to reduce computational time and to optimise the simulation, several modifications to the model were made. Initially the substrate was reduced from full dimensions to a length of 0.2cm and a depth of 0.05cm, boundary conditions to all the walls were added in order to maintain a very similar temperature distribution in the model, and less spots per layer (30 instead of 120) were simulated. However, the number of layers simulated was 4, giving a total of 120 spots simulated in order to maintain constant the total number of spots simulated. The powder layer depth is maintained as 50μm. Another change undertaken with respect the model developed in section 4.2 is that now the elements (PLANE 77) are constant all along the model in order to simplify the coupling process that will be undertaken in section 4.4. The mesh used for the FEM calculations in the present section is shown in Figure 4.12.

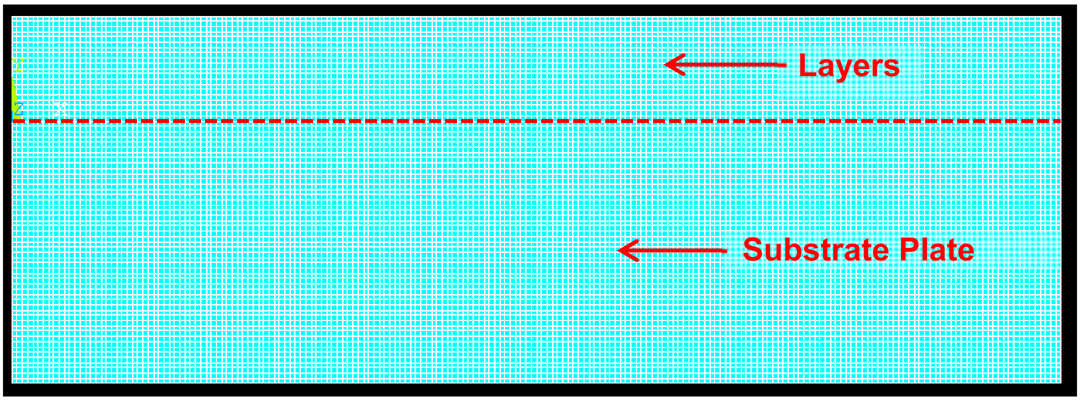

Figure 4.12. 2D FEM mesh used in the layer-by-layer model.

Table 4.3 shows the process parameters used to calculate the temperature distribution of several laser spots irradiated onto several layers of powder are enlisted.

The scanning strategy used within the developed model considers that the laser starts always in the same x coordinate and in the corresponding y coordinate and moves to the left until the 30 spots are completed. This consideration is undertaken in order to simplify the algorithm used in the mode.

It is worth to mention that the number of layers and spots was limited due to storage limitations of the generated data. Since the data obtained from this stage is going to be coupled with CA, the FEM model used contains 1,500,000 nodes. This amount of nodes leads to high computation times and high storage capabilities. So in order to optimise the developed model the assumptions mentioned before were considered.

Table 4.3. Process parameters for 2D layer-by-layer model.

LP	143W
ET	450µs
LD	50µm
Tr	12s
PD	25µm
Number of layers (Ln)	4
Ab	0.06
T_{sol}	811K
T_{liq}	905K
T_{amb}	298K
ρ	For powder see Table 3.4. For solid see Table 3.3.
Cp	For powder see Table 3.4. For solid see Table 3.3.
K	For powder see Table 3.4. For solid see Table 3.3.
hc	20W/m^2-K
α_{xx}	3.0
α_{yy}	1.5

The methodology followed in the layer-by-layer model is similar to the methodology used in model developed in section 4.2. In Appendix 1 Figure 2, the routine followed by the model developed in the present section is represented. It can be noted that one step has been added in comparison to the routine of section 4.2; this step involves the identification of the number of layers to be modelled.

4.2.2 Results and discussion of the 2D layer-by-layer FEM model

After the setup detailed in section 4.3.1 is undertaken, the relevant calculations of the FEM model are performed. Figure 4.13 shows the resultant temperature profile after the irradiation of 120 laser spots distributed within 4 layers of powder.

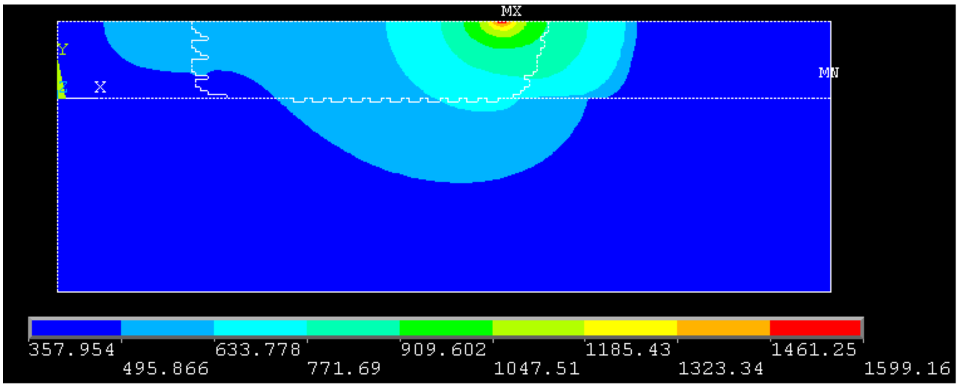

Figure 4.13. Predicted temperature profile of the layer-by-layer model

According to the calculations performed by the layer-by-layer model, after the irradiation of 120 laser spots the reached temperature is of 1599.15K. The predicted temperature is above the melting point of AA-2024; therefore, a melt pool with certain dimensions is expected to form.

In order to determine a correct trend in the thermal history of each layer and spot, the maximum temperature at each spot is plotted in Figure 4.14.

If the data shown in Figure 4.14 is analysed on more detail it can be observed how the maximum temperature at each layer tends to increase, this increase in temperature happens due to the thermal history of the previous layers. It is also observed that the temperature increases and decreases each spot; this variation can be attributed to both the error present in the simulation and the heat dissipation along the powder bed. It is also noted that the temperature profile in the first layer is constant, as it can be observed in the corresponding trend line, however in the consequent 3 layers there is a sudden increase of temperature near the end of the strategy. The variations of temperatures shown in Figure 4.14 should also be reflected in the evolution of the formed melt pool, in order to determine and analyse the mentioned variation the melt pool dimensions are plotted in Figure 4.15.

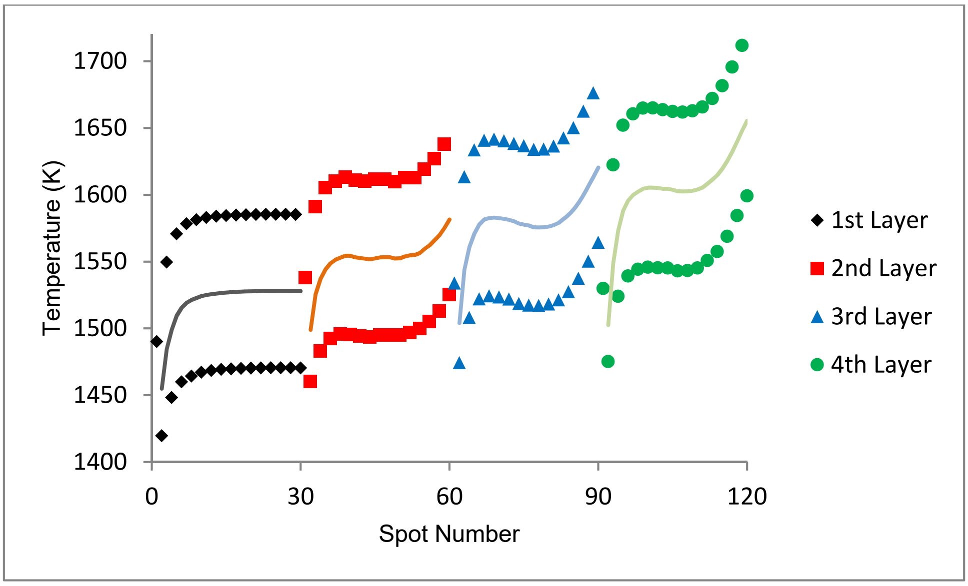

Figure 4.14 Temperature evolution of each irradiated spot.

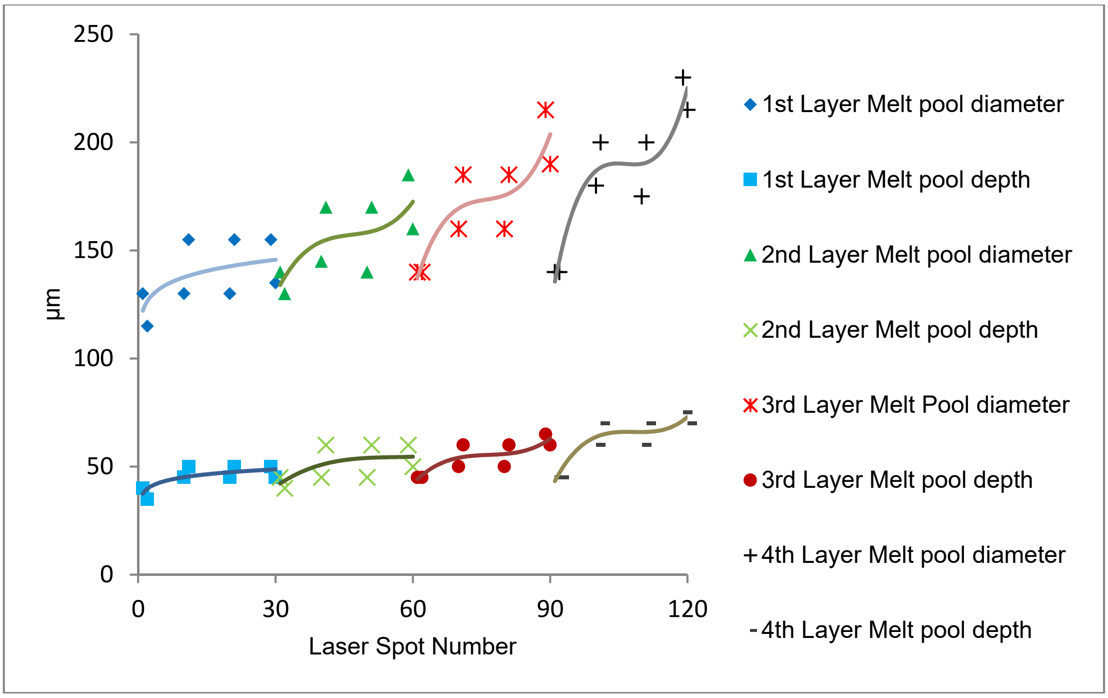

Figure 4.15. Evolution of the melt pool’s diameter and depth

Both the diameter and the depth of the melt pool are dependent of the thermal variations in each spot, as supposed. However if Figure 4.15 is observed with more detail, the melt pool diameter has a strong relationship with the temperature variations of the spot, since the trend lines are almost identical. In contrast the melt pool depth has very similar trends but the penetration of heat through layers is less than in the direction of the scanning. This difference of heat transfer along the coordinates can be attributed to the type of flow induced in the melt pool. This flow is characteristic of a negative surface tension gradient coefficient as discussed in Chapter 2. The increase and decrease diameter and depth of the melt pool between spots can be observed as in previous Figures. Again, this phenomenon can be attributed to both the error in the FEM calculations and the heat transfer effect in the process.

If it is supposed that after the irradiation of 120 laser spots, the obtained melt pool will maintain an average size then the melt pool diameter and depth can be measured and establish at the last irradiated laser spot (as shown in Figure 4.16)

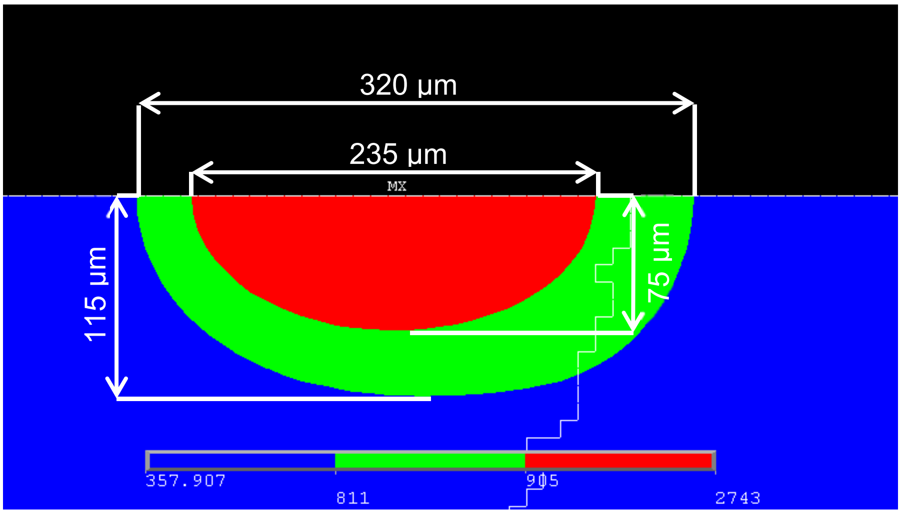

Figure 4.16 Maximum predicted melt pool size and HAZ.

The supposed maximum melt pool size obtained with different processing parameters will be validated with experimental data in Chapter 6.

As the model developed is a layer-by-layer process, each spot should have a thermal history. Figure 4.17 shows the evolution of the thermal history of several selected points across the deposited powder layers with data plotted.

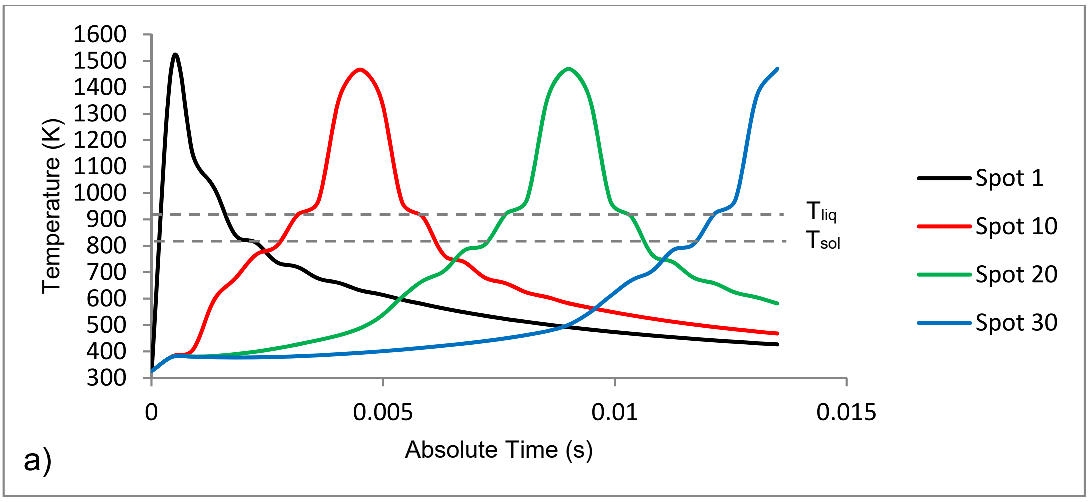

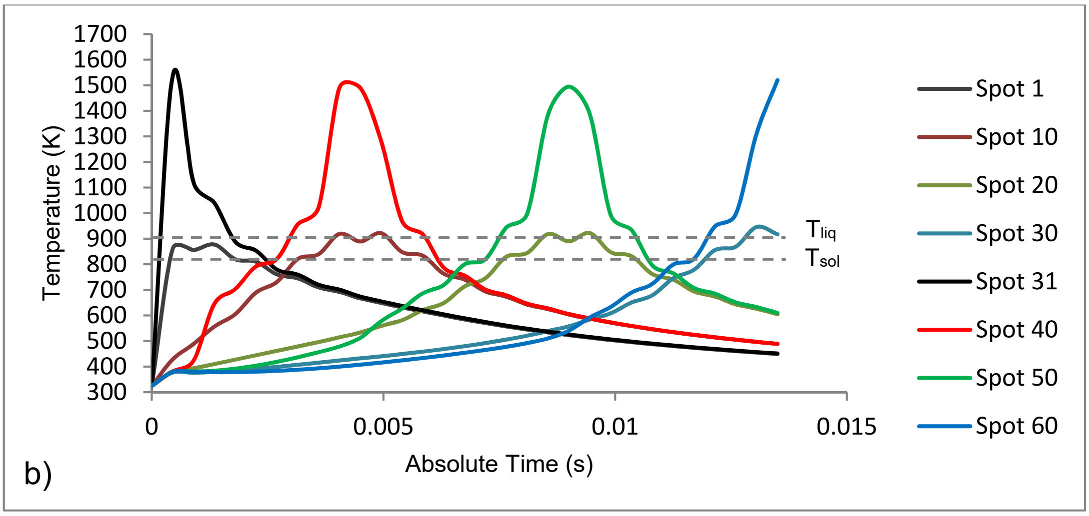

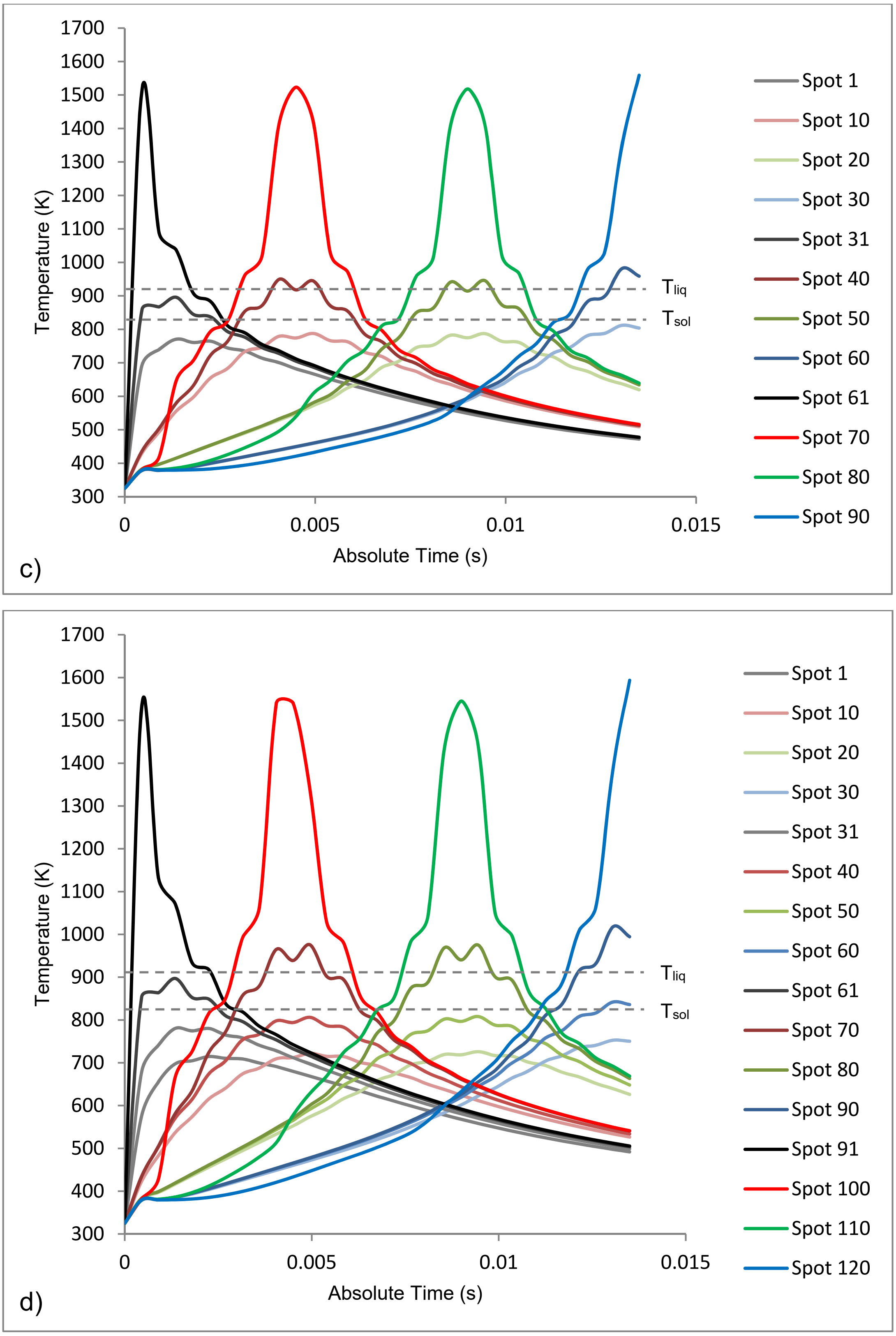

Figure 4.17. Thermal history of several points at an absolute time on the powder bed of the a) first layer, b) second layer, c) third layer and d) fourth layer.

From the data obtained from the developed layer-by-layer model and shown in Figure 4.17 it can be noted how the temperature at the centre of a spot evolves through time and through deposited layer. Figure 4.17d plots the monitored data of all the evaluated spots, it can be observed that the spots irradiated during last layer (layer number 4) are marked with a high intensity colour, however the spots irradiated during the first layer and monitored during the last layer are represented in less intense colours. The same applies to Figure 4.17b and c. With the combination of the obtained data and the melt pool dimensions' data it can be said that for the specific case of the simulated parameters a generated melt pool will penetrate a small portion of a previous solidified layer as well as heat to temperatures near the T_{liq} and T_{sol} deeper layers, as shown in Figure 4.27.

In order to validate the model with theory, the predicted cooling and solidification rates after the laser was irradiated are enlisted in Table 4.4.

Table 4.4 Predicted cooling and solidification rates.

Spot Number	Average cooling rate before T_{liq} (K/s)	Average cooling rate between T_{liq} & T_{sol} (K/s)	Solidification rate (K/m)	Thermal gradient in the liquid (K/m)
10	4.1×10^5	3.2×10^5	3.1×10^6	3.5×10^6
20	4.1×10^5	3.2×10^5	3.1×10^6	3.5×10^6
40	4.2×10^5	2.9×10^5	2.6×10^6	3.5×10^6
50	4.1×10^5	3×10^5	3.1×10^6	3.5×10^6
70	4.9×10^5	1.9×10^5	2.35×10^6	3.5×10^6
80	4.9×10^5	1.9×10^5	2.6×10^6	3.5×10^6
100	4.1×10^5	1.8×10^5	1.8×10^6	3.5×10^6
110	4×10^5	1.1×10^5	2.65×10^6	3.5×10^6
Average	4.3×10^5	2.37×10^5	2.66×10^6	3.5×10^6

The data shown in Table 4.4 agrees with the theory mentioned in section 4.2.2. So in general terms, considering the assumptions made within the developed layer-by-layer model, it agrees with theory and is able to predict successfully the solidification conditions for a SLM AA-2024 part.

The developed FEM model shown up to this point considers a laser beam irradiating a powder bed surface for a time defined by the ET; however, when the laser moves to the next spot it immediately starts the irradiation, this means there is no idle time between irradiations. The experimental data that will be discussed later in Chapter 6 were fabricated by a Renishaw SLM system which has a modulated laser; this means that an idle time between spots is present. So it can be said with this statement that the developed model has slight variations of the actual process, however in parallel a model that considers this idle time (of approximately 25μs) was developed. In general terms the predicted maximum temperature after the irradiation of a total of 120 spots on 4 layers including the idle time per spot is of 1583.65K (compared to the 1599.15K shown before) and the melt pool dimensions are: 225μm of diameter and 75μm of depth (compared to 235μm of diameter and 75μm of depth). However, the computing time of the “spotted” model is 2 times higher than the previously shown model. So in order to reduce processing time and considering that the final results of both models are almost the same, the model that will be used from this stage onwards is the model that doesn’t considers the idle time between irradiated spots.

The next stage will use the data obtained in the model developed in this section in order to virtually “grow” and predict the final microstructure of a produced part. The next section will describe in detail the development of the microstructural evolution prediction model.

4.3 Cellular Automata – Finite Element Model for the Simulation of Microstructural Evolution

The thermal history of the SLM process determines the microstructural evolution of a part, and it has gained more attention in recent years, as mentioned in Chapter 2. Therefore, there is a need of a numerical model able to consider the thermal history of a part in order to predict the evolution of the microstructure. Throughout this section the development of such model is detailed.

The microstructural evolution prediction model was self-developed and programmed in C++ and uses the information predicted by the 2D FEM layer-by-layer model described in section 4.3 and couples the resultant mesh with a CA mesh. This coupling is undertaken in order to have a thermal dependent grain growth during the solidification of the generated melt pool within SLM. The developed model uses the weak coupling mode of the CA-FE method introduced in section 2.3.1.3. The calculations of variation of enthalpy, density, and other variables are calculated in the FEM model; meanwhile the CA model calculates exclusively the nucleation and growth of the grains using the temperature values of the FEM model.

The set up process of the developed CA-FE model will be described with detail.

4.3.1 Setup of the CA-FE model

The prediction of the microstructural evolution requires a smaller scale than that generally used for thermal modelling. So the CA-FE coupling can be considered as a multi-scale modelling technique since it uses the FEM model to calculate the temperature profiles of the SLM process in a larger scale in order to calculate the growth of grains at a smaller scale.

For the scope of the present work, the CA mesh elements are considered to be of a size of 1μm. This in order to capture with great detail the interaction between melt pools, layers and grains, as well as to maintain the established ratio of at least 5:1 determined by the convergence study performed on section 4.1. It is worth to mention that the CA-FE model developed in the present section does not consider dendritic, nor eutectic, nor planar growth, or rapid solidified structures; it only simulates the interaction of grains as a whole in the solidifying system. The FEM model developed in section 4.3 will be modified in order to have an element size of 1μm, in order to relate directly each node of both meshes and simplify greatly the developed algorithm. So the dimensions of the CA-FE mesh will be the same as those mentioned in section 4.3.

According to Janssens et al. (2007) a generalised form CA is defined by the following minimal description:

- A n-dimensional space is partitioned into a discrete subset of finite dimensional volumes, which are named cells. In which in the case of the current research this are the elements of the FEM mesh.
- A state is assigned to each cell. The states assigned to each cell are “powder”, “solid”, “liquid” and “mushy”.
- At every time step (defined by the FEM model), a local neighbourhood is defined for each cell. For the present research, a Von Neumann Neighbourhood (see Figure 2.17) will be used.
- A state change rule is defined, which computes the new state of a cell as a function of the state(s) of all cell(s) in the local neighbourhood of that cell. Rule 254 of the CA rules described by Wolfram (2002) (see Figure 4.18) will be used in the present research in order to compute any state change.
- A CA simulation proceeds by discrete simulation steps – hence discrete time steps – consisting of the computation of the new states of all cells based on their current states.

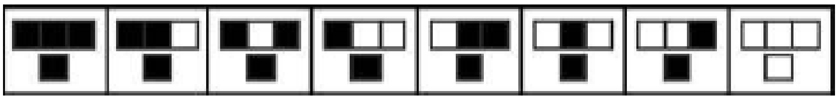

Figure 4.18. Graphical depiction of a CA state transformation function. A shaded square has a state 1, and unshaded state 0 (Frans et al., 2007).

The developed CA-FE model requires inputting the number of grain orientations, nuclei density as well as the undercooling temperature. Based on experimental observations (see figures 3 and 4 in Appendix 2) the number of grain orientations was determined as 4. According to Jacobson and McKittrick (1994) rapid solidification could result in undercooling the melt to a temperature below the T_{sol}, or up to a temperature in which only the solid phase is present; in such conditions a single phase solid could then nucleate and grow, having the same composition as the liquid phase. In the scope of the present work the undercooling temperature will be established as 94 K (T_{liq} – T_{sol}) for SLM processed AA-2024 based on the work undertaken by Jacobson and McKittrick (1994); and the nuclei density will be determine by experimental values obtained in Chapter 5.

The algorithm used to predict the microstructure evolution of AA-2024 parts produced with SLM can be found in Figure 3 in Appendix 1.

In general terms the data calculated by the FEM model by Ansys Mechanical APDL is first imported and translated by the algorithm, once the data is loaded in its own matrixes the CA matrix is then created based on the imported data and the programming conditions. This process is repeated every time step until a final CA matrix is obtained after the FEM defined time steps. The final CA matrix will contain the data related to the microstructural evolution along the scanned area.

Next the predicted thermal history in section 4.3 will be used to calculate the microstructural evolution in section 4.4.2. The obtained results will then be analysed and discussed.

4.3.2 Results and Discussion of the CA-FE Model

After running the algorithm showed in section 4.4.1 and inputting the adequate parameters the final microstructure is predicted and shown in Figure 4.19. Note that the different grain orientations are represented with different colours (red, green, blue and pink).

By visual inspection, it can be determined that the predicted microstructure bare a close resemblance (in terms of the direction of the columnar growth) to actual microstructures obtained from the SLM processing of AA-2024, as shown in Figure 4.20.

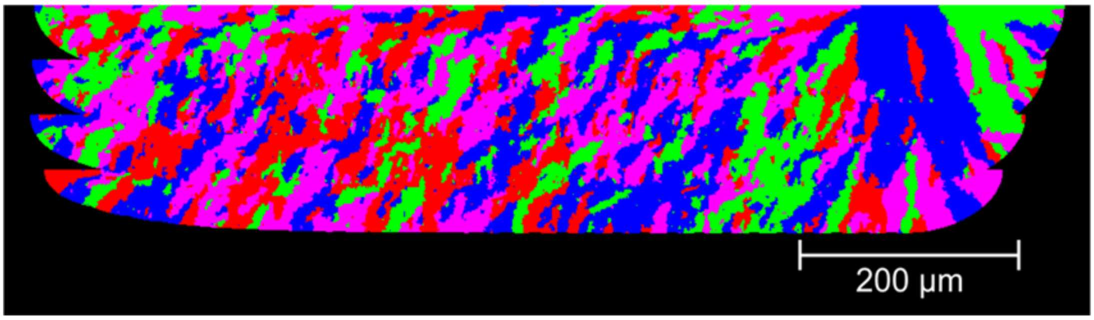

Figure 4.19. CA-FE model predicted microstructure of sample 1 after the irradiation of 120 laser spots.

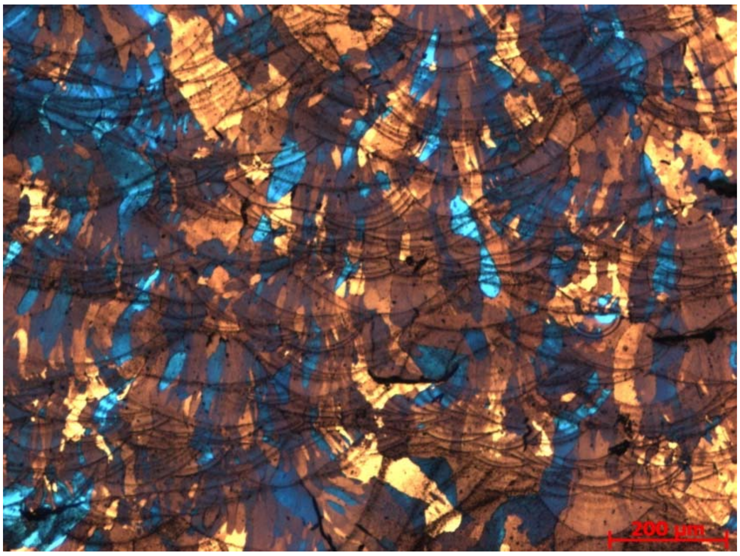

Figure 4.20 Micrograph of resulting microstructure of sample 1 of AA-2024 processed on SLM.

Despite having developed a model that illustrates how grains evolve while the laser advances through the powder bed, the experimental evaluation performed is on the final formed microstructure. The detailed experimental evaluation of the microstructure evolution is out of the scope of the present research. However, it is important to have an indication of how it develops spot after spot and layer after layer. Therefore Figure 4.21 shows this evolution in a time frame of every 15 irradiated laser spots.

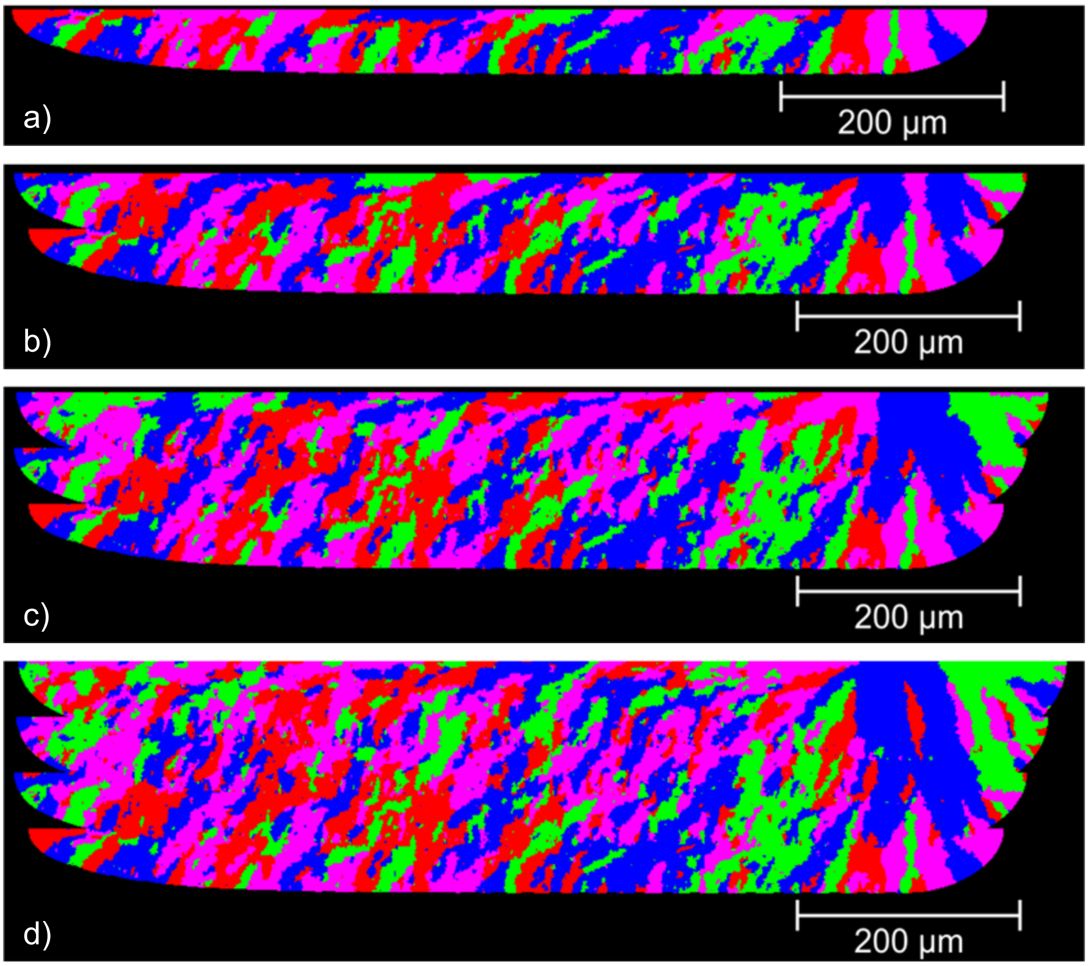

Figure 4.21 Calculated microstructure evolution of sample 1 after the deposition of a) 1 layer, b)2 layers, c) 3 layers and d) 4 layers.

From the evolution shown in Figure 4.34 it can be observed that the developed CA-FE model is able to calculate in a similar way the columnar growth which usually is present on SLM produced parts, as well as the interaction of grains within spots and layers.

From the simulated microstructure an average grain size number (GS) can be calculated, which can be compared afterwards with experimental data. In order to calculate the GS of the predicted microstructures, the ASTM E112 standard will be followed. According to ASTM E112 grain measurements of specimens with non-equiaxed grain shapes should be made on longitudinal, transverse and planar oriented surfaces for rectangular bar, plate or sheet type material. Using the intercept method, measurements can be made using directed test lines in either three or six of the principal directions using either two or three of the principal test planes. However, for the scope of the present research measurements will be performed only in one direction, parallel to the build direction of the component, since the developed models are two-dimensional. The GS will be determined measuring the mean number of grain boundary intersections per unit length (P_L). Considering that $GS = 6.643856 \log_{10} P_L - 3.288$ a grain size number will then be calculated. After calculating the average GS for the predicted microstructure a value of 8.3 ±0.47 was obtained. This value will be compared with experimental obtained data in Chapter 6, in order to determine if the developed model is reliable to predict the microstructure of SLM produced parts using different processing parameters.

In the next section, a summary of the models developed on the current chapter will be presented.

4.4 Summary

Throughout the present chapter different models were developed and presented in order to accomplish the ultimate goal of the present research, the development of a numerical model which can predict the final microstructure of an AA-2024 produced via the SLM process is shown in section 4.4.

During the first stages of the development of the numerical model, FEM is used and a detailed model of the SLM process was then created. In sections 4.1 and 4.2 a two-dimensional single layer and a layer-by-layer model were created respectively, both models uses as input most of the parameters involved in the manufacturing of parts on an actual SLM machine (i.e. laser power, point distance, hatch spacing, etc.) and other parameters that are particular for the material used (i.e. absorptance, density, thermal conductivity, etc.) in order to predict accurately the temperature profiles. In literature several models of the SLM process using FEM can be found (Shiomi et al., 1999, Matsumoto et al., 2002, Guo-feng and Guang-nan, 2004, Roberts et al., 2009, Gusarov et al., 2007, Gusarov and Smurov, 2009, Gusarov and Smurov, 2010, Körner et al., 2011, Song et al., 2012, Safdar et al., 2013, Loh et al., 2015, Foroozmehr et al., 2016), however few of them model with detail the powder-liquid-solid transformation, and none of them model with detail the liquid to solid properties (mushy zone), which is one of the novelties of the developed model, the included ability to perform thermal calculations of the mushy zone in order to have a more detailed solidification model (CA-FE). The obtained results of the developed models were accordingly presented and discussed in their respective sections. However, a comparison of the simulated results with the experimental results was not included in the present chapter, since this will be discussed with detail and in parametric studies in Chapter 6.

The temperature profiles obtained with the layer-by-layer FEM developed model will serve as input for the CA-FE model presented in section 4.4, which simulates the solidification phenomenon present in the SLM process. The developed CA-FE uses the CA technique described in Chapter 2 in order to predict the microstructural growth. The CA-FE model was self-coded with C++ and in section 4.4 the algorithm followed by the developed code is shown and explained. As shown in section 4.4 the predicted microstructure bare close resemblance with actual microstructures obtained with the SLM process for AA-2024 in terms of direction of growth and type of growth. However, in order to determine if the predicted results are accurate and reliable, the average GS of both experimental and simulated results for different processing parameters will be measured and discussed in Chapter 6. In general terms it can be said up to this point that the developed CA-FE method is novel and further experimental validations to the model will be performed.

5. Experimental Methodology

Within the present chapter the experimental procedures followed to produce, characterise and measure the parameters of interest of samples produced using SLM. This is used as a tool to validate experimentally the developed numerical models (Chapter 6).

Within the scope of the present research, the material of interest as mentioned in Chapter 3 is AA-2024, in order to produce this material using SLM a set of specific processing parameters are needed, however, specifically for this material limited information can be found on literature of previous SLM related work. So in order to select the optimal processing parameters (i.e. LP, ET, etc.) for the current aluminium alloy a design of experiments was performed. In section 5.1 the design of experiments is presented and the optimal parameters are found. The optimal processing parameters were those which produced the highest density part.

Once the highest density part was obtained, the relevant specimen was prepared in order to obtain the micrographs of interest, as well as some selected samples with less density. The procedures followed in order to prepare the samples and obtain the relevant micrographs will be described in section 5.2.

Once the samples were accordingly prepared, micrographs of the melt pool size and the microstructures were obtained and analysed in section 5.3. The main interest in this section will be on how the average size of the melt pool of each of the selected samples as well as an average GS was calculated, which are of interest for the present research.

Each of the mentioned sections within the present chapter contains fully detailed procedures as well as descriptions of the work undertaken within the scope of the research.

5.1. Design of Experiments

A Design of Experiments (DOE) usually predicts an outcome (in this case the density) by introducing changes on preconditions (processing parameters). Ultimately a DOE will describe the variation of the outcome under conditions that are hypothesized to reflect the variation. Only basic procedures followed for the DOE will be presented, since the optimisation of processing parameters is not within the scope of the present research, however, this step is briefly included because there was the need to fabricate high density samples in order to validate experimentally the numerical model.

In order to predict the optimal processing parameters for AA-2024 a DOE was produced according to the minimum and maximum processing parameters. The DOE was undertaken with assistance of Minitab Statistical Software, using a 2 level full factorial design with 4 factors (LP, ET, PD and HS) and 1 response (density). A full factorial design was selected because of its efficiency for estimating main effects (averaged effects of a single factor over all units) and the ability to assess the interaction among the factors (Cox and Reid, 2000). The low and high factors for the full factorial design are shown in Table 5.1 and were selected based on previous experience of different aluminium alloys within the University of Sheffield Additive Manufacturing research group.

Table 5.1 Low and high values of the factors.

Factor	*Low*	*High*
Power (w)	120	200
Exp. Time (μs)	90	450
Point Distance (μm)	25	60
Hatch Spacing (mm)	0.03	0.08

Entering the corresponding data to the software, 16 experiments were suggested based on the defined limits (see Table 5.2). The suggested experiments were then produced on the SLM system and the obtained specimens (as shown in Figure 5.1) were accordingly analysed (sample preparation and density measurements through micrographs) in order to determine their approximate density.

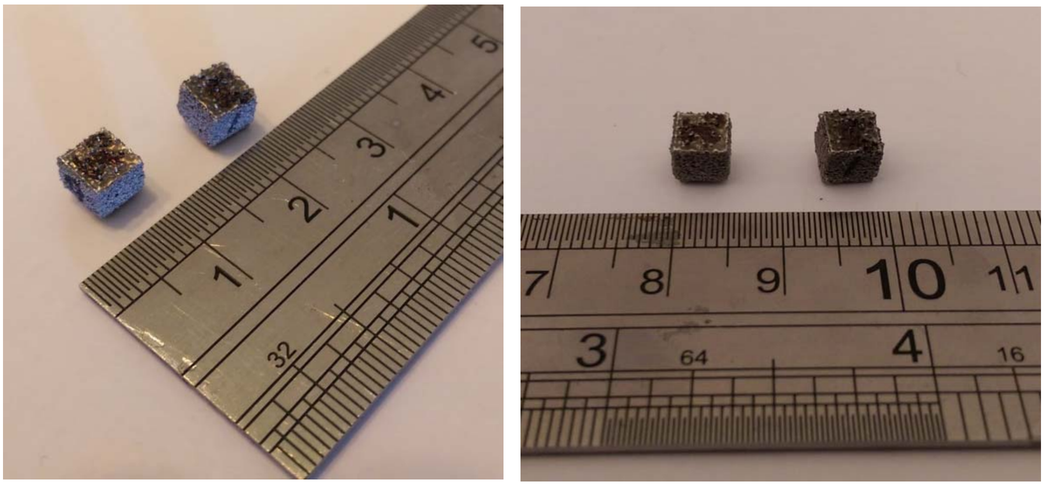

Figure 5.1 Produced samples

Table 5.2 Full factorial table with density results.

Sample	*Power (W)*	*Exposure Time (μs)*	*Point Distance (μm)*	*Hatch Spacing (mm)*	*Measured Density (%)*
1	120	90	60	0.08	52.55
2	120	450	25	0.03	80.46
3	120	450	25	0.08	61.87
4	200	90	60	0.08	82.40
5	120	450	60	0.03	55.78
6	200	90	60	0.03	74.09
7	200	450	60	0.03	97.46
8	200	450	25	0.03	91.05
9	200	450	60	0.08	88.87
10	200	90	25	0.08	91.25
11	120	90	25	0.08	59.28
12	120	90	60	0.03	24.45
13	200	450	25	0.08	97.40
14	120	450	60	0.08	85.97
15	120	90	25	0.03	69.48
16	200	90	25	0.03	66.65

The measured approximate density was entered to the DOE in order to predict the optimal parameters for a 100% dense part. According to the response optimizer tool of Minitab, the optimal set of processing parameters for AA-2024 are those shown in Table 5.3:

Table 5.3 Optimal processing parameters for AA-2024.

Power (W)	200
Exposure Time (μs)	400
Point Distance (μm)	25
Hatch Spacing (mm)	0.08

The present research will focus on samples with a density value above 90%, so the set of optimal parameters (shown on Table 5.3) along a random set of parameters selected shown in Table 5.4, which were calculated for different values of power using the response optimiser of Minitab, were produced and analysed. The number of samples shown on Table 5.4 were selected in order to accommodate in a single build five samples of each set. These lower density samples will help to validate under several conditions the developed models.

Table 5.4 Selected processing parameters to produce.

Sample	LP (W)	ET (μs)	PD (μm)	HS (mm)	Measured ρ
1	200	450	25	0.08	99.2%
2	200	450	35	0.8	97.7%
3	180	350	30	0.03	96.9%
4	170	400	60	0.08	92.9%
5	170	300	60	0.7	93.1%
6	170	300	50	0.08	90.5%
7	170	400	50	0.08	93.5%

After the production of the samples maintenance was carried on to the system in which the samples were produced, briefly before the scheduled maintenance. During a scheduled maintenance of the Renishaw SLM system the actual laser power was measured and it was determined that at 200W the system had a real output of 143W, at 150W was 98.8W, at 100W was 63W and at 50W was 25.1W (due to laser degradation). Therefore, the laser power in the model and in future builds was reduced to model these more realistic laser power outputs for the current Renishaw system.

At this point it is worth mentioning that in modelling the hatch spacing, this value is ignored, since this value is a tri-dimensional variable of the process that describes the spacing between lines within a layer, as shown in Figure 5.2., and the developed numerical models are in 2D. Therefore, the values to consider going forward are the power, exposure time and point distance.

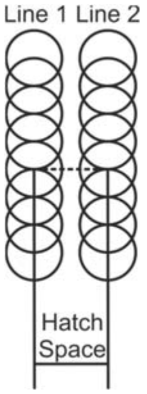

Figure 5.2. Hatch Spacing Description

Samples were produced in two primary sets: benchmark samples (samples in which data will be used as an input to the models) and validation samples (samples in which data will be used to validate the developed models). Samples from both sets were obtained from different builds in order to take into account the intrinsic variability of the SLM system.

In the next section the procedure followed to obtain the desired data from the fabricated samples is to be detailed, and other valuable data will be presented as well.

5.2. Sample Preparation

In order to study the microstructure of AA-2024 produced by SLM, metallographies of the produced specimens where obtained; metallography studies the constitution and structures of metals and alloys. In order to perform a proper metallographic sample preparation a series of basic steps should be followed. In sequence the steps were mounting, grinding, polishing, etching and microscopic examination.

The selected specimens were mounted on Bakelite on a Struers CitoPress-5 automatic mounting press. Once mounted the samples were then grinded and polished according to standard procedures using a Struers LaboSystem automatic preparation system.

Once the samples were polished a density analysis was performed on each of them, in order to input the data to the DOE developed in section 5.1. Afterwards they were etched with two different reagents in order to reveal different structures. A set of samples were immersed for 30 seconds on Keller's reagent (95mL water, 2.5 mL HNO_3, 1.5 mL HCl, and 1.0 mL HF) in order to reveal the melt pool geometry of the samples. Another set of samples was anodized using Barker's reagent (1.8 % Fluoboric acid in water) on a Struers LectroPol-5 with 20V for 80s and agitation velocity of 10RPM at 22°C.

The etched specimens were then examined in a Carl Zeiss inverted optical microscope in order to capture the desired micrographs. The specimens etched with Barker's reagent were examined using polarized light in order to see the revealed microstructure in colour. The analyses undertaken to each of the micrographs is presented in the next section.

5.3. Micrograph Analysis

The validation of the developed models in Chapter 4 was performed with experimental measurements of the melt pool size and the average GS of the corresponding specimens. In this section a brief explanation of how measurements were taken to the produced specimen is to be presented, more detail on the obtained data will be presented and discussed in Chapter 6.

The micrographs of the specimens etched with Keller's reagent reveal part of the microstructure of the specimen, however the generated melt pools by the irradiated laser beam to the powder bed can be clearly observed and analysed with specimens etched with this reagent, see Figure 5.3.

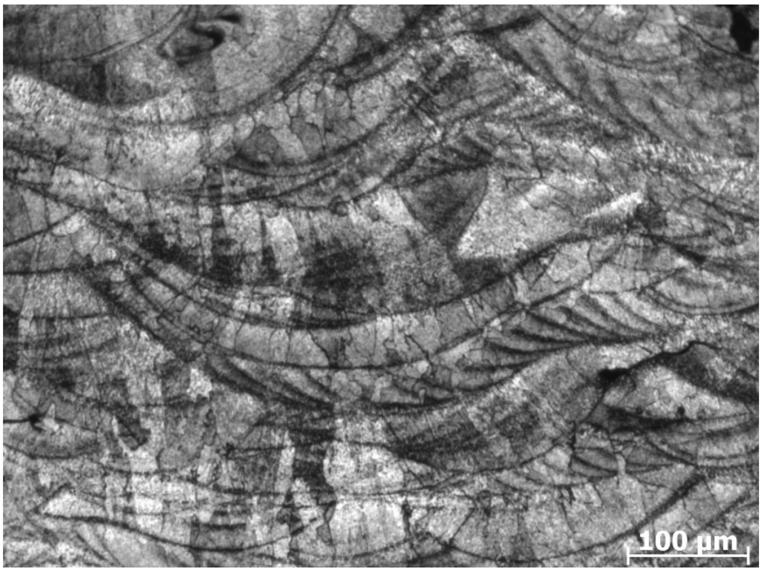

Figure 5.3 Revealed structure of specimen etched with Keller's reagent (100x).

Example micrographs of the produced samples (benchmark and validation) etched with Keller's reagent can be found in Figures 1 and 2 in Appendix 2. From the obtained micrographs per specimen the melt pool diameter and depth was then analysed per sample, see Figure 5.4. The dashed lines in Figure 5.4 represent an approximate location of the deposited layers; approximately 3 to 5 measurements (shown in different colours in Figure 5.4) to the clearest melt pools per micrograph were performed to the 10 micrographs obtained per sample. Examples of the performed measurements to benchmark and validation samples can be found in Figures 1 and 2 in Appendix 3. The obtained data for all the produced samples (diameter, depth and standard deviation of the measurements) will be presented in Chapter 6 and compared with the data obtained from the developed numerical models.

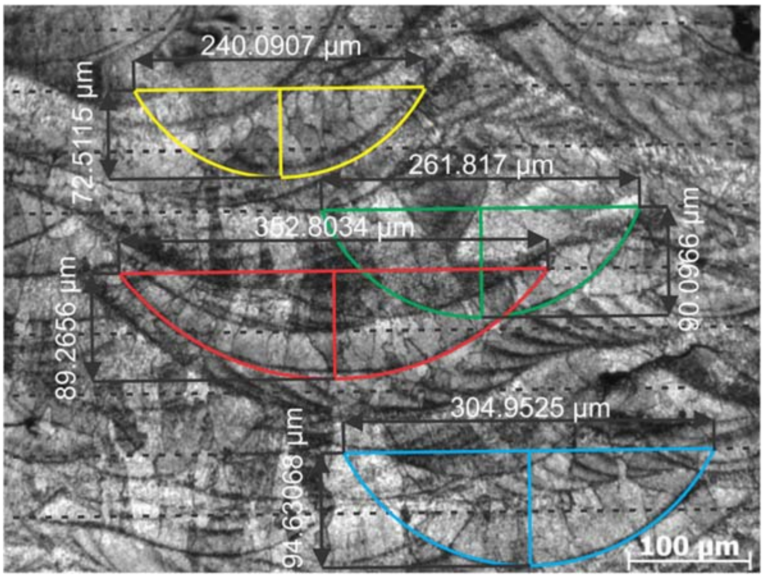

Figure 5.4 Measured melt pool size and diameter (100x).

It can be observed that microstructure was also revealed on the samples etched with Keller's reagent; however, it was difficult to identify where grains were located along the sample. In contrast the samples anodized with Barker's reagent gave some colour to the obtained micrographs and the identification of grains was performed with more ease (see Figure 5.5).

More example micrographs of the benchmark and validation samples etched with Barker's reagent can be found in Figures 3 and 4 in Appendix 2. From the micrographs obtained from the specimens anodized with Barker's reagent the average GS was determined according to the procedure mentioned on the ASTM E112 standard described in Chapter 4, see Figure 5.6.

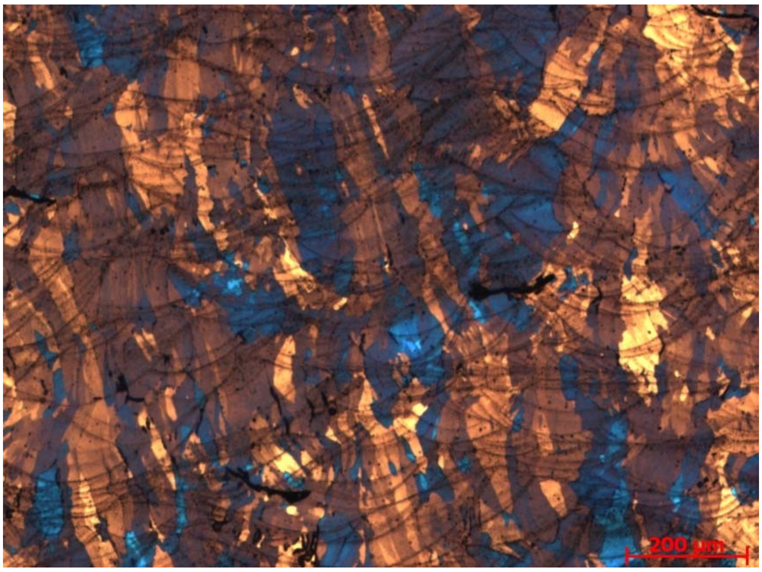

Figure 5.5 Revealed microstructure of specimen anodized with Barker's reagent (50x).

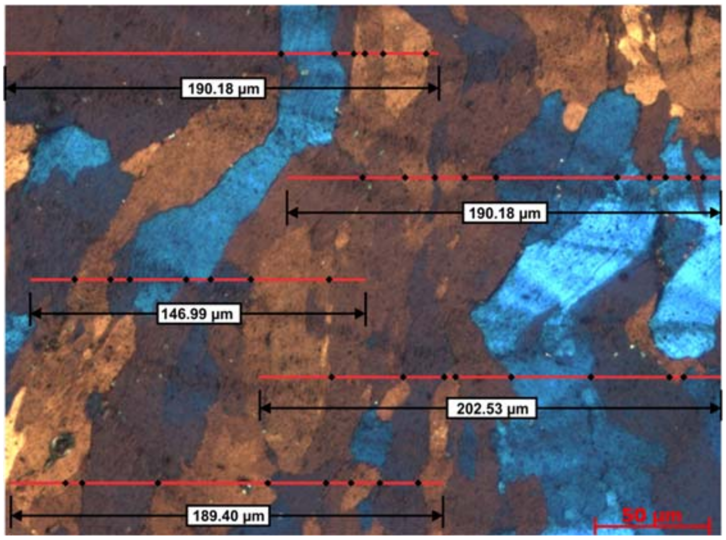

Figure 5.6 Count of grain boundary intersections per length unit in order to calculate an average GS according to the procedure determined by the ASTM E112 standard (@200x).

It is noted that the measurements were performed at a magnification of 200x in order to identify with more detail the grains intersecting the defined line in the micrograph. Examples of measurements performed to benchmark and validation samples can be found in Figures 3 and 4 in Appendix 3. As observed in Figure 5.5 the grains are not equiaxed, they are columnar, so in order to determine a consistent average GS within all the analysed specimens, the measurements were performed parallel to the deposited layers and not perpendicular, see Figure 5.6. With these considerations a consistent comparison with the predicted microstructure of the numerical model was performed. The calculated average GS of each produced specimen will be shown and compared with the simulated data in Chapter 6.

5.4. Summary

The experimental procedures followed in order to obtain the required data for the validation of the developed numerical models was described and detailed on the development of the current chapter.

Section 5.1 briefly described the DOE performed in order to produce “acceptable” specimens (high density specimens) that provided the required data (melt pool dimensions, average GS) for the validation of the numerical models. Once the optimal processing parameters were found and suitable specimens produced, further preparation of the specimens was performed.

In section 5.2 the metallographic preparation steps followed in the current work was described. The steps were carefully followed in order to have a correct preparation of the specimens. Two different steps were performed during the specimen preparation in order to obtain different data (melt pool dimensions and average GS). Once the preparation of each of the specimens was correctly performed each of the samples were then examined using an optical microscope in order to obtain micrographs which then could be analysed.

A description of the analyses undertaken to the obtained micrographs is then presented in section 5.3. The analyses performed included the measurement of the melt pool dimensions of each specimen, as well as the average GS, the obtain data from this stage will then be compared with the developed numerical models in Chapter 6.

With the data obtained from the experimental procedures, the experimental validation can now be performed; in the next chapter the procedures followed in order to validate the developed models in the current research will be presented and accordingly discussed.

6. Results - Experimental Validation

The experimental validation of the developed numerical models is presented in the current chapter. The validation stages are of upmost importance in order to rely on such numerical models; these models need to be compared with experimental data. Once the model is validated future results of the developed model can be used as a basis for future work, otherwise the reliability and accuracy of the developed model is compromised.

As the microstructural evolution of the produced part depends on the thermal history imposed by the process, two models were developed, as shown in Chapter 4. One of the developed models predicts the temperature profile imposed by the process, and the other developed model uses the thermal history calculated by the first model and calculates the microstructural evolution. Based on this the validation process is divided in two parts.

The first part of the validation process is described in section 6.1. In order to validate the temperature distribution, the melt pool dimensions of experimental parts are compared with the melt pool dimensions predicted by the developed model. This ensured that the thermal history of both the model and the process were similar.

The second part of the validation can be found in section 6.2. Once the dimensions of the melt pool were predicted and validated with experimental data, the predicted microstructure has to be validated as well. In order to validate the predicted microstructure an average GS was used to measure both experimental parts and simulated microstructures. As soon as the validation was performed, this process ensured that the predicted microstructures developed by the model agree with future calculations.

More detail on the procedures followed to perform the validation can be found on each of the sections within this Chapter.

6.1. Melt Pool Dimensions Validation

In order to validate the developed FEM model that predicts the thermal history present in the SLM process a melt pool measurement of produced and simulated specimens was performed. The measurement of melt pools was selected as a validation procedure since actually measuring the thermal history generated by a 35μm laser spot with accuracy directly within the process is challenging.

The procedures followed to obtain the melt pool dimensions on the samples produced by the SLM system were described in Chapter 5. In Table 6.1 the measured melt pool dimensions of the produced samples are presented. Examples of the performed measurements can be found in Figures 1 and 2 in Appendix 3.

Table 6.1 Experimental mean melt pool dimensions.

Sample	*Experimental mean diameter (μm)*	*Standard deviation of measured diameter*	*Experimental mean depth (μm)*	*Standard deviation of measured depth*
1	237.82	38.71	77.6	11.58
2	205.77	19.58	74.66	8.84
3	205.46	37.98	76.05	11.69
4	202.41	24.97	82.09	13.23
5	200.14	22.3	78.58	11.94
6	179.22	20.60	73.99	8.80
7	208.56	26.10	82.7	11.15

An average of 30 melt pools per sample were measured in order calculate the data shown in Table 6.1. The data obtained from the benchmark samples was then used as in order to find the correct anisotropic enhancement factor (described at Chapter 4) according to the processing parameters, the relationship between the factor and the parameters will be discussed with detail in Chapter 7.

Using the appropriate anisotropic enhancement factor the maximum dimensions of the predicted melt pools by the developed FEM model were measured, shown in Table 6.2. The predicted temperature profile evolution used to measure the predicted melt pool size of each sample, can be found in Figures 1 to 7 in Appendix 4.

Table 6.2. Measurement of the predicted melt pool by FEM layer-by-layer model.

Sample	*Maximum Predicted Diameter (μm)*	*Maximum Predicted Depth (μm)*
1	235	75
2	220	75
3	195	65
4	210	75
5	195	70
6	205	70
7	210	75

In order to directly compare both experimental (benchmark and validation samples) and predicted melt pool dimensions are plotted, see Figure 6.1.

The presented data suggests that the developed 2D layer-by-layer FEM model predicts within 86% the melt pool dimensions of parts produced on the SLM system. With this as a basis, the temperature profiles calculated by the FEM model successfully predicts the actual thermal history that it is imposed to a part processed with SLM.

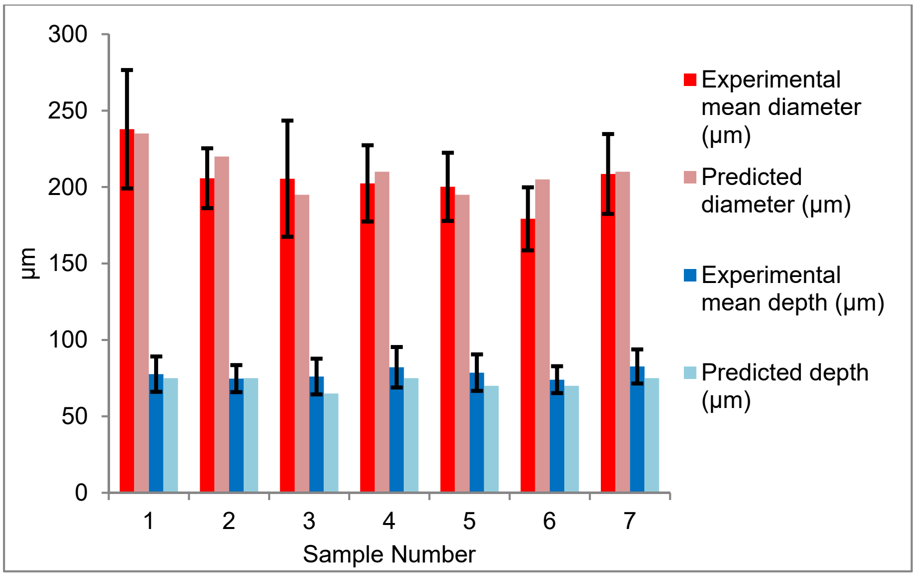

Figure 6.1 Comparison between experimental and predicted data.

Once the FEM model was validated with experimental data, the model was then used as input data for the developed CA-FE model as described in Chapter 4. The validation of the CA-FE was then performed and is described in the next section.

6.2. Average Grain Size Number Validation

The resulting microstructure of a SLM produced part is characterised by a columnar growth towards the build direction. As described previously in Chapter 4, the ASTM E112 standard will be followed in order to determine an average GS. The ASTM E112 procedure is followed in order to obtain the GS for both experimental and predicted microstructures in order to validate the developed CA-FE model.

The samples produced with the SLM process were then measured according to the procedure described in Chapter 5. The obtained average GS of the produced samples is shown in Table 6.3. Examples of the performed measurements can be found in Figures 3 and 4 in Appendix 3.

Table 6.3 Experimental average GS.

Sample	GS	*Standard deviation*
1	8.32	0.46
2	8.47	0.65
3	9.05	0.40
4	8.11	0.34
5	9.05	0.48
6	8.71	0.59
7	8.66	0.51

An average of 50 measurements per sample was performed in order to calculate the data shown in Table 6.3. The measured data of the benchmark samples was then used as an input to the developed CA-FE model, since as mentioned in Chapter 4, an average number of grains per melt pool is required as an input for the developed model. A more detailed description of how this information is interpreted by the developed code will be presented in Chapter 7.

Once the data was inputted, the model calculated the final predicted microstructure for each of the developed samples. The average GS was then calculated; the obtained values are shown in Table 6.4. The predicted microstructural evolution from were measurements were extracted can be found in Figures 1 to 7 in Appendix 5.

Table 6.4. Measurement of predicted average GS by the CA-FE model.

Sample	*GS*
1	8.47 ±0.59
2	8.07 ±1.62
3	9.34 ±0.60
4	9.31 ±0.67
5	9.13 ±0.23
6	9.13 ±0.39
7	9.42 ±0.83

In Figure 6.2 both experimental and predicted data are plotted in order to have a direct comparison of both dimensions.

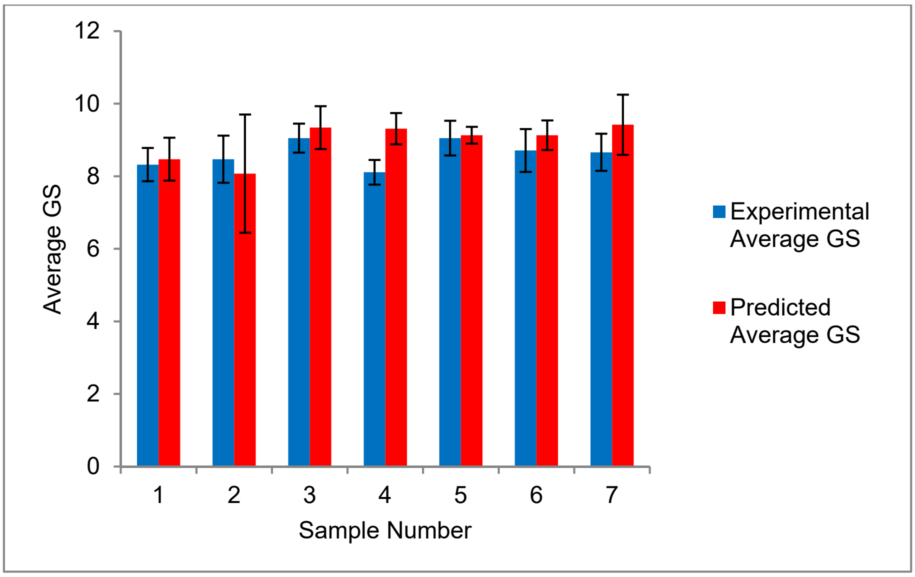

Figure 6.2 Comparison between experimental and predicted data.

The data shown in Figure 6.2 suggests that the developed CA-FE model predicts within an 88% the average GS of parts produced on the SLM system. Figure 6.3 shows images of both predicted and experimental microstructures of sample number 1 in order to visually compare the obtained data.

From the example shown in Figure 6.3, when analysed in more detail it was observed that the predicted microstructure has grains that grow through several deposited layers, comparable to the type of growth present in the corresponding experimental data. It was also observed that small equiaxed grains can be found near the interactions between layers in both microstructures, limiting the further growth of columnar grains. These observed phenomena on both predicted and experimental data also corroborated that the developed model successfully predicts the final microstructure of parts produced by FEM.

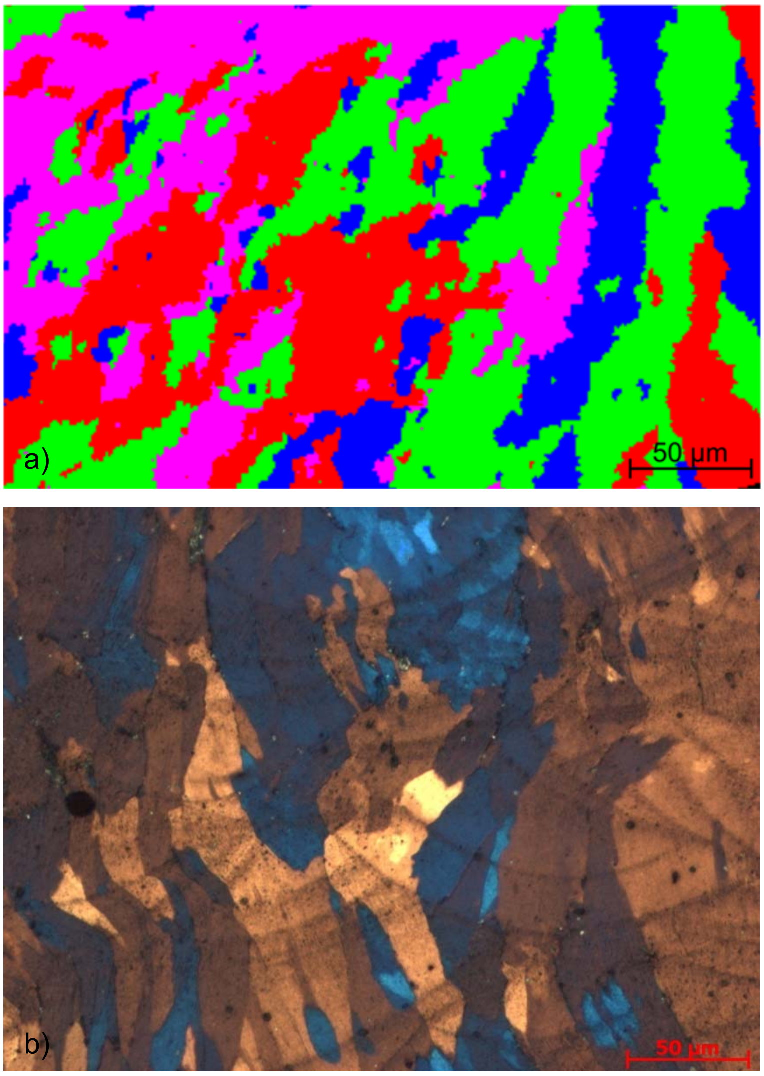

Figure 6.3 Comparison of a) predicted microstructure and b) experimental microstructure (@ 200x) of sample number 1.

The data was used as an input in order to optimise both developed numerical models is not the same as the data used to validate the model as mentioned in Chapter 5. Tables 6.1 and 6.3 present the mean data of all of the fabricated samples and its standard deviation. This was undertaken in order to have a more reliable comparison between the predicted and the experimental information in order to ensure that both developed models are reliable enough to predict both melt pool dimensions and obtained microstructures for future builds. Based on the standard deviation of the measured experimental data it can be determined that the developed models successfully predict both the temperature profiles generated within the process and the final microstructure of a produced part.

6.3. Summary

Within the current Chapter the experimental validation of the developed FEM and CA-FE models was described and performed.

In section 6.1 the developed thermal model was validated with data obtained from both benchmark and validation samples. According to the presented data the developed FEM model predicts the melt pool dimensions of parts produced by SLM, hence, it is supposed that the developed FEM model predicts successfully the thermal history and temperature profiles generated within the SLM process. This reliable data is then used in order to perform the relevant calculations in order to predict the final microstructure.

The developed CA-FE model which predicts the final microstructure of SLM produced parts is then validated in section 6.2. The validation is performed using data from both benchmark and validation samples. According to the data and observations presented in section 6.2 the developed CA-FE model successfully predicts the final microstructure of a part produced by SLM, independently of the processing parameters used.

Further analysis of the developed models was performed and it is described, analysed and discussed in Chapter 7.

7. Result Analysis and Discussion

Valuable information can be extracted and analysed from the developed models presented in Chapter 4. These developed models were subjects of experimental validation, which was presented in Chapter 6, and it was concluded that the results obtained successfully predicted the effects of the SLM process. Within this chapter an in-depth analysis to the data extracted from the developed models is shown.

At first instance the developed 2D layer-by-layer FEM model developed on the present research provides valuable information about the actual SLM process. The extracted information will be presented, analysed and discussed with detail in section 7.1. Along with the data obtained from the model, a relationship between the anisotropic enhancement factor, introduced in Chapter 4, and the processing parameters will be established in order to accurately simulate an artificial melt pool flow within the calculations. A brief discussion of how the developed FEM model will assist to optimise processing parameters in future work will also be presented.

The data extracted from the developed CA-FE model will be analysed and discussed in section 7.2. Within the mentioned section a discussion of how the developed model is able to predict the columnar growth within the actual SLM parts will be presented, as well as a brief discussion on how the developed model can be used in future work to customise microstructures based on the optimised processing parameters according to the performance requirements of the part.

A more detailed discussion and analysis of the abovementioned is presented throughout this Chapter.

7.1. Analyses of the 2D layer-by-layer FEM developed model

In this section a detailed analysis of the data obtained from the 2D layer-by-layer FEM developed model will be discussed. The selected data to analyse and discuss was considered as the most valuable information available from the developed model; although more data can be extracted, for the scope of the present research only the data of interest will be analysed.

7.1.1. Anisotropic enhancement factor relationship with processing parameters.

The anisotropic enhancement factor concept was introduced in Chapter 4, and according to Safdar et al. (2013) it artificially simulates the melt pool flow in SLM on FEM. So, based on this argument, this methodology was applied to the developed model in order to accurately predict the simulated melt pool dimensions.

During the development of the FEM model, the correct value of anisotropic enhancement factor was found by trial and error, comparing the results obtained from the benchmark samples with the results obtained by the simulation. The found values of anisotropic enhancement factor that result in accurate predictions for each of the benchmark samples are listed in Table 7.1.

Table 7.1 Anisotropic enhancement factor used for each sample.

Sample Number	α_{xx}	α_{yy}
1	3.0	1.5
2	3.0	1.5
3	15.0	8.0
4	25.0	15.0
5	25.0	15.0
6	25.0	15.0
7	25.0	15.0

Despite having different processing parameters for each of the selected samples, the anisotropic enhancement factor seems to have a relationship with one of the processing parameters used for each sample. After analysing the processing parameters presented in Table 5.3 it was observed that a relationship with the laser power and the anisotropic enhancement factor can be established in order to predict the correct anisotropic factor to use on future predictions. The prediction of this factor can be undertaken within the limits of the maximum power the SLM system and the lowest power, in which acceptable samples can be obtained, see Figure 7.1.

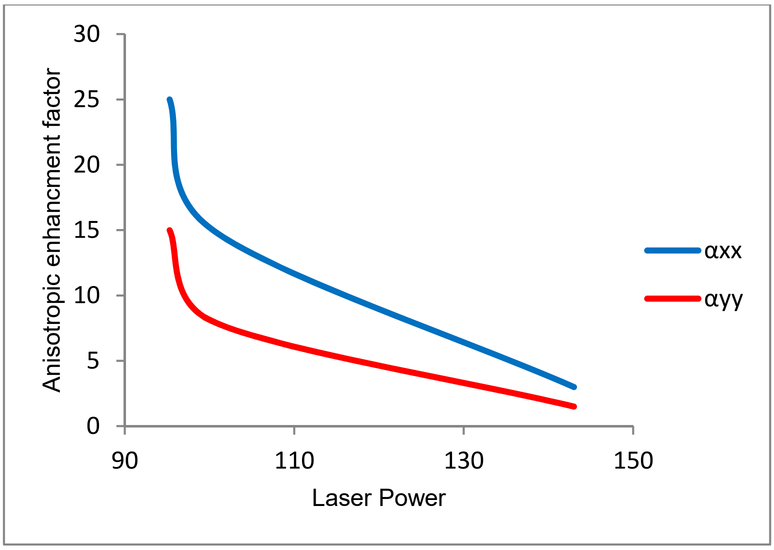

Figure 7.1 Relation between laser power and anisotropic enhancement factor

Following the above-mentioned relationship (see Figure 7.1), if values are selected within the established limits, it will be possible to calculate a correct prediction of the melt pool dimensions. It is worth to mention that such argument is just a hypothesis since further validations are required in order to rely on this relationship; those validations were not performed in the current work since it consists of significant additional experiments that falls outside the remit of this research, it has therefore been suggested as inclusion for future work.

7.1.2. Prediction of cooling and solidification rates.

From the developed 2D layer-by-layer FEM model valuable information regarding the cooling rates to which the sample is imposed can be extracted. A brief description of this process was described in Chapter 4; however, in the present section a more detailed analysis will be performed.

As described in Chapter 4, the RSP estimated cooling rates are in the range of 10^5 to 10^6K/s (Jacobson and McKittrick, 1994). Kurz and Trivedi (1994) outlined the solidification conditions to a similar process to SLM, and established a relationship between the $|\dot{T}|$, G and V, defined as $|\dot{T}| = G * V$. Usually the solidification conditions for laser processing will lead to a columnar growth, see Figure 4.11. At first instance the model agreed with theory (as discussed in Chapter 4 and shown in Table 4.4); however, the performed calculations were only for a set of processing parameters. The calculation was then performed on all of the produced samples, in Table 7.2 the mean cooling and solidification rates extracted from the developed 2D FEM layer-by-layer model are shown, as well as the calculated mean V.

Table 7.2. Mean cooling and solidification rates extracted from developed FEM for each simulated sample.

Sample Number	Mean cooling rate of the liquid (K/s)	Mean cooling rate at the mushy zone (K/s)	Mean solidification rate (K/m)	Thermal gradient in the liquid (K/m)	Calculated mean V (m/s)
1	4.3×10^5	2.38×10^5	2.66×10^6	3.5×10^6	0.12
2	5.41×10^5	2.30×10^5	2.14×10^6	2.9×10^6	0.18
3	1.12×10^5	1.70×10^5	1.91×10^6	1.7×10^6	0.07
4	1.55×10^5	2.41×10^5	1.67×10^6	1.7×10^6	0.09
5	2.11×10^5	2.55×10^5	1.35×10^6	2.2×10^6	0.1
6	1.45×10^5	2.68×10^5	1.35×10^6	2.2×10^6	0.07
7	1.15×10^5	2.28×10^5	1.82×10^6	2.0×10^6	0.06

Using the data obtained from the developed FEM model (see Table 7.2) along with the microstructure selection map, see Figure 4.11, it is possible to predict the resulting microstructure of the sample, which in all of the cases will be a columnar growth.

Harrison et al. (2015) used measurements of primary dendrite arm spacing of parts produced with SLM in order to calculate an estimated cooling rate of the process. The estimated cooling rate of ~3x10^5 agrees with the values obtained in the developed model. So based on this study it can be said that the present model could be used to predict the primary dendrite arm spacing on parts produced by SLM and study its variation and dependence of this parameter with the fabrication processing parameters.

7.1.3. Prediction of the Heat Affected Zone

The HAZ is defined as an area of a material that has had its microstructure and properties altered as a consequence of heat. The extent and magnitude of property change depends primarily on the material and the amount and concentration of inputted heat. In the present section the HAZ will be considered as the area in which the temperature is between the liquidus and solidus temperature of the material. In general, due to the small laser beam spot used in the SLM process, the HAZ can be considered as small, however it may slightly change the resulting microstructure of a part.

The developed FEM model can predict the HAZ; however, the effect of the HAZ in both the developed simulations and in produced parts is not within the scope of the present work. Hereafter, this section will only be presented as an area of opportunity for future researches in regards the effects of the HAZ on produced samples and its prediction.

Figure 7.2 shows the two types of envelopes predicted by the developed FEM model.

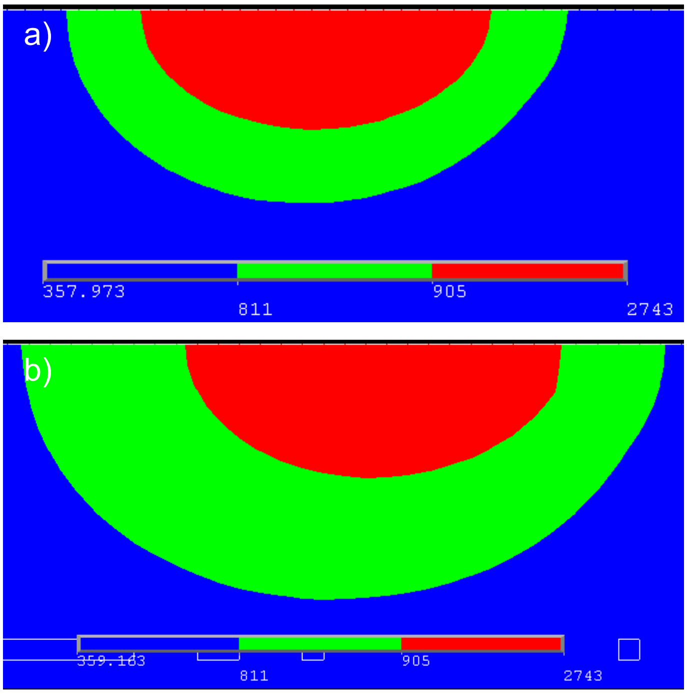

Figure 7.2 Predicted distribution of HAZ (green area) a) with low processing speed and b) high processing speed.

The predicted HAZ distribution is greatly affected by the apparent velocity of the moving heat source. If the apparent velocity of the heat source is slow the distribution will be constant, see Figure 7.2a; however, as the apparent velocity of the moving heat source increases, a HAZ distribution will be as that shown in Figure 7.2b.

The microstructure within the HAZ could be altered, just as in laser welding (see Figure 7.3); however, more detailed studies need to be performed to the areas surrounding the melt pool in order to determine its effect and the importance of the HAZ on the final obtained microstructure on parts produced by SLM. The model developed in the current research could then be used as a basis in order to predict the HAZ effects on parts build with SLM.

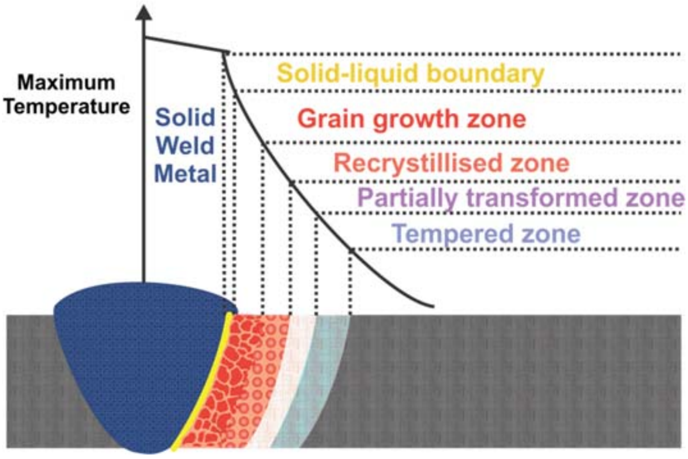

Figure 7.3 HAZ on laser welding.

7.1.4. Possible Prediction of Porosity

As it is known, porosity plays an important role in parts produced by the SLM technology. When a new material is to be manufactured using this technology a DOE of experiments in order to obtain a ~100% dense part is usually undertaken. This DOE involves trying different set of processing parameters in the machine in order to produce samples which can then be analysed to determine their porosity. This process involves usage of time and material on the machine; however, the DOE process could be aided by the developed FEM model improving the time and material consumption.

In Chapter 5 several processing parameters that produce porosity were selected. After simulating these sets of parameters on the developed model, porosity was predicted as observed on the example, see Figure 7.4.

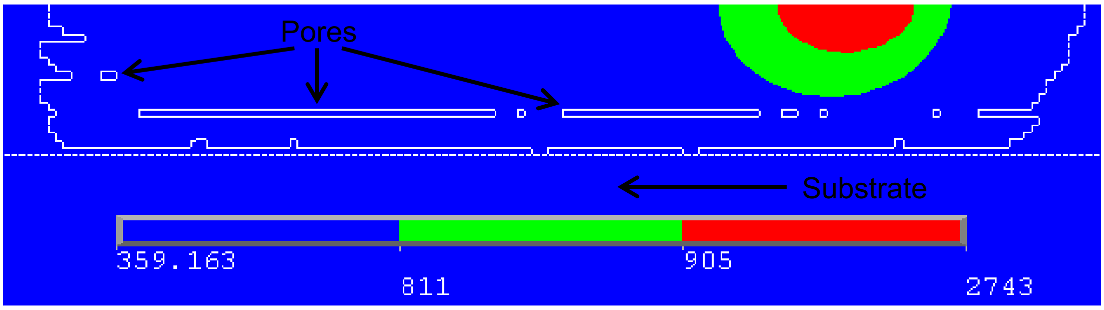

Figure 7.4 Predicted porosity on developed FEM model of sample number 7.

The dashed line delimits the substrate from the powder bed, the solid line envelopes the formed solid after the irradiation of the laser beam. If the results from sample 7 (see Figure 7.4) are closely analysed, the first layer of powder was not fully melted and almost null or slight penetration into the substrate can be observed, which in consequence generated the same effect to the subsequent layer. Therefore, it can be said that the model can predict when a layer will not be fully melted and porosity will be generated.

The developed model can be used as an initial tool in order to understand the effects of the laser power, exposure time and point distance on the material of interest. The results of the prediction could then help to define the lower and upper limits of the parameters of interest on a DOE. Nevertheless, using the developed model will not ensure that porosity will be completely eliminated on produced parts, since it only represents the 2D effects of the above-mentioned parameters. Usually, defects such as porosity are driven by more complex phenomena as well (i.e. solidification, lack of melting, gas inclusions, etc.), and the study of such factors was not within the scope of the present research. The prediction of porosity with a numerical model might be an interesting area of opportunity, in order to expand the capabilities of the developed FEM model. The aforementioned will be useful to consider, as in a near future, this tool might be used to find the optimal processing parameters of a material instead of the methodology followed at the present time.

7.2 Analysis of the developed CA-FE model

A detailed analysis of the data obtained from the developed CA-FE model will be presented and discussed in the present section. The data concerning to the columnar growth and the appearance of small sized grains from the developed model will be discussed. Additionally, understanding how microstructure is formed on a process like SLM may lead to future possibilities of customising the obtained microstructures of parts produced via this technology; therefore, this will be a subject to be analysed in this section as well.

7.2.1 Prediction of columnar growth by the developed CA-FE model.

As described in Chapter 4, the developed CA-FE model uses the calculated temperature profiles by the developed FEM model in order to predict the microstructural evolution of a simulated part produced by SLM. The developed CA-FE model uses data provided by produced benchmark samples in order to successfully predict the microstructure. The data inputted to the developed code is in form of a probability of nucleation based on the measured GS. The probability of nucleation is a parameter that depends of the material to be used, so in the specific case of the present work this probability was established as 0.025 based on experimental observations and trial and error runs of the code. The probability of nucleation was also calculated using a theory proposed by Sands (2007), however the calculated value is several orders of magnitude lower (0.0003) than the above-mentioned value. Using the probability of nucleation calculated with the theory proposed by Sands (2007) on the developed CA-FE model, the obtained microstructures do not agree with experimental information.

As discussed in Chapter 6, the average GS of the predictions made by the developed CA-FE model agrees with experimental information obtained from experiments. In addition, making a close comparison of the predicted microstructure with the microstructure obtained from experiments (see Figure 7.5) a high aspect ratio of columnar with smaller equiaxed type interspersed grains can be observed in both microstructures. It can be observed (despite the difference in colours) in both the predicted and experimental microstructure that columnar grains grow between layers and visually have a similar length. It is also observed in both microstructures that two or more grains with the same orientation intersect at some point forming bigger grains, supressing the growth of smaller columnar or equiaxed grains in between layers. However, in order to fully validate these similarities, more deposited layers should be simulated. This in order to measure the average GS number of the length of the grains and compare the predicted values with experimental values.

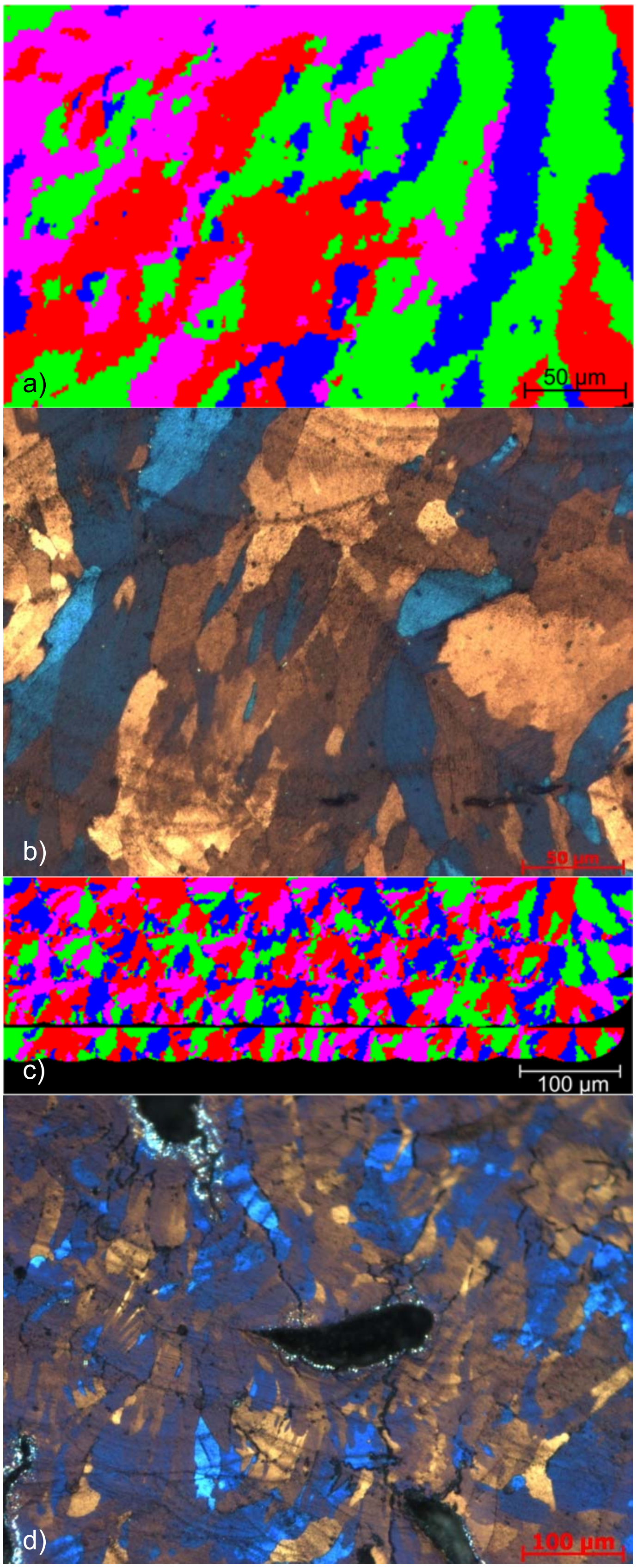

Figure 7.5 a) Predicted microstructure vs b) actual microstructure (@ 200x) of highest density sample (#1), and c) predicted microstructure vs d) actual microstructure (@ 100x) of lowest density sample (#6).

New grain boundaries intersecting primary columnar grains are occasionally formed at the limits of each melt pool at the prediction, comparable to the observed phenomenon in the experiments performed, as well as in the work undertaken by Harrison et al. (2015). New formed grains continue to grow and competitive growth will have an important role on the layer-by-layer process as the heat flux reduces. For reference, see Figures 3 and 4 in Appendix 2, as well as Figures 1 to 7 in Appendix 5.

In all of the presented cases the predicted microstructures contained similar phenomena observed on experiments, so it can be reconfirmed that the developed CA-FE model successfully predicts the microstructural evolution of actual parts produced by SLM and helps to further understand the grain growth mechanisms that are present within parts produced by SLM.

7.2.2 Possible customisable microstructure model

In order to completely control the SLM process looking into the manufacture of fully customised components can be achieved once the grain growth mechanisms are fully understood. The level of understanding of the grain growth mechanisms involved in the SLM provided by the develop model, will help to further develop actual SLM technologies.

The manufacture of fully customised components is one of the next big challenges SLM technologies have. The technology by itself has the capacity to perform this task; however, as above-mentioned it needs to be fully controlled in order to accomplish the desired. Trial and error experiments are usually performed in order to track any change within a manufactured component via SLM. The developed model on the present research could then be a key if it is included as a tool and used along the process in order to achieve greater objectives saving time and material.

The developed model in the present research, if used as a basis, has the capabilities to be further developed in order to be used as an accurate predictive tool during the customisation of components. Within the model, different processing conditions can be tested in order to determine the resultant variability within the process and accurately predict the desired customised microstructure.

7.3 Summary

Data extracted from the developed 2D FEM layer-by-layer and CA-FE models was analysed and discussed within the current Chapter.

In section 7.1 data extracted from the FEM model was discussed. A relationship between the anisotropic enhancement factor and the laser power was established in order to successfully predict the melt pool diameter of SLM processed AA-2024. The calculated cooling and solidification rates from the model confirmed once again, that the process could be considered as a RSP technique. Using the calculations introduced in Chapter 4, the calculated V was used along the predicted G and the microstructure selection map in order to determine the type of microstructure will form, which in all of the cases was a dendritic growth, as expected. From the FEM model the HAZ zone can be predicted as well, its effects are suggested to be further studied in order to determine its importance to the final microstructure of components fabricated with SLM; the developed model could be an important tool in order to determine those effects. Defects such as porosity play an important role in components produced via SLM, the developed tool if further developed, could accurately predict generated porosity within the process and avoid such defects.

Section 7.2 extracts information from the novel CA-FE developed model and discusses its findings when making comparisons with experimental information. It is noted that similar growth phenomena found in experiments are also predicted by the developed tool. The developed model was able to predict the formation of small equiaxed grains at the liquid interface of the formed melt pools, which then will compete with larger columnar grains and grow towards the general heat flux. This effect results in both, limiting the growth of big columnar grains and the formation of small and dispersed equiaxed grains. These predicted results were also found on experiments; therefore, through these made observations it was determined that the developed model successfully predicts the final microstructure. The developed tool could then be used in future research as a tool to obtain customised microstructures. The development of these customised components is one of the next steps to be integrated within technologies such as SLM, the developed tool will be of great importance to accomplish and understand the phenomena involved during the processing of components via SLM.

8. Conclusions and future work

8.1. Conclusions

The theory and methodology for the creation of a model that could predict the microstructural evolution of a component manufactured with SLM has been presented. A CA-FE coupling was proposed as a possible simulation technique capable of predicting the grain growth of a component undergoing numerous thermal cycles via the SLM process. In order to develop such coupling, a novel approach to create a FEM model was proposed. This proposed approach calculates the material properties in each of the material's state (powder, liquid, solid and mushy zone) in order to accurately predict the solidification process within the developed FEM model. The proposed models are the first of their kind, since previous works overlook diverse properties of the powder bed as well those of materials.

A novel approach of a 2D FEM single layer and a 2D FEM layer-by-layer model was created. The developed models use as input most of the parameters involved in the manufacturing of parts via SLM (i.e. laser power, point distance, exposure time, etc.) and other properties particular for the material used (i.e. absorptance, density, thermal conductivity, etc.) in order to predict the temperature profiles generated within the process. Similar FEM models of the SLM can be found on literature (Shiomi et al., 1999, Matsumoto et al., 2002, Guo-feng and Guang-nan, 2004, Roberts et al., 2009, Gusarov et al., 2007, Gusarov and Smurov, 2009, Gusarov and Smurov, 2010, Körner et al., 2011, Song et al., 2012, Safdar et al., 2013, Loh et al., 2015, Foroozmehr et al., 2016); however, few of them model with detail the mushy zone properties. Including the ability to perform thermal calculations of the mushy zone within the developed models is one of the novelties of this research. The integration of the mushy zone calculations in the present model allowed the development of detailed solidification model (CA-FE).

The temperature profiles calculated by the novel 2D FEM layer-by-layer model, served as an input for the novel self-developed code CA-FE coupling. The developed CA-FE model uses the temperature profiles calculated by the developed FEM approach in order to simulate the solidification phenomenon present within the SLM process. After the calculations were performed by the CA-FE model, the calculated microstructures were similar to the microstructures of components manufactured via SLM.

Benchmark and validation samples were produced in order to experimentally validate both FEM and CA-FE models. The melt pool dimensions and the average GS for benchmark samples were measured and the obtained results were used as an input to calculate both the anisotropic enhancement factors (FEM) and the nucleation density (CA-FE) of the models. Simulations were performed and the results were compared with those of the validation samples. The melt pool dimensions and the average GS were used in order to validate the calculated temperature profiles and microstructures. After the validations were performed, it was concluded that both FEM and CA-FE model successfully predict both the temperature profiles and microstructures of components manufactured via SLM.

From the developed 2D FEM layer-by-layer model, valuable data was extracted. In order to predict the melt pool dimensions of AA-2024 components manufactured via SLM a relationship between the anisotropic enhancement factor and the laser power was established. From the simulation, cooling and solidification rates were extracted in order to confirm that the process is considered as a RSP technique. Using these rates and the GV microstructure selection map, it was determined that the formed microstructure would be composed by a dendritic growth. The HAZ was predicted by the developed FEM model and further studies were suggested in order to determine its importance within the SLM process. Porosity, a common defect of parts manufactured via SLM, was predicted by the developed FEM model. These predictions can be used to avoid such defect when using the SLM process to manufacture components. It was suggested to perform further validations to the porosity predictions in order to fully rely on the results obtained from the FEM model.

The calculated microstructures by the CA-FE model had considerable similarities with those of components manufactured via SLM. Calculated microstructures had similar growth phenomena to those found in experiments. The formation of small equiaxed grains at the liquid interface of the formed melt pools were predicted, which then will compete with larger columnar grains and grow towards the general heat flux. This growth competition led to the appearance of either small dispersed grains or columnar grains that stopped growing between layers due to these dispersed grains. These same effects were observed in experiments, determining that the calculated microstructure by the developed CA-FE model agree with experiments.

Given that the developed models agreed with experimental data, it is expected that such models could be used with other materials and expanded to a three-dimensional space in order to predict generated temperature profiles and microstructure of components manufactured with SLM. The development of customised microstructures could be one of the next steps to be integrated within technologies such as SLM. In addition, the developed models could be used to aid future research to understand and control the physical phenomena present during the manufacturing of a component using the metallic powder bed process SLM.

8.2 Future Work

Attempting to account for all of the physical aspects involved during laser melting is a challenge. The following recommendations could be considered for future research in this area.

The developed models do not take into account the three-dimensional space behaviour of temperature profiles or microstructure formations. An expansion to 3D could be performed in the future, in order to have more realistic and accurate prediction tools.

The FEM model in the present research takes into account the flow present within a melt pool using an anisotropic enhancement factor. However, this is not the most accurate way to simulate this effect. In future work, the lattice boltzmann method should be considered in order to take into account this phenomena and accurately simulate the formed melt pools and the melting of powder particles.

The FEM model developed during the present research is able to predict the HAZ and formed porosity. However, further studies to these phenomena should be considered in order to determine the effects of the HAZ on microstructures of components manufacture by SLM, and in order to accurately predict the formation of pores with the FEM model in order to avoid such phenomenon on manufactured parts.

The CA-FE model developed in the present research uses a “weak” coupling mode, in which the solidification calculations are performed only by FEM. The fully integration of both developed models should be performed in future work. Since this will ensure that the solidification within the model considers all the physical aspects involved in the development of this phenomena.

Computing time is always an important parameter in numerical models. Even though in the present research computing time is not mentioned, it is a clear area of opportunity for further development. In the models, the approximate time to obtain results from the developed FEM models is of ~96 hours, in contrast the CA-FE gives results in ~4 hours. Future research should be perform into optimising the developed FEM model so the processing time could be reduced.

The current research focused on a single material (AA-2024). Further materials should be tested on the developed models in order to expand their application.

9. References

ASLE ZAEEM, M., YIN, H. & FELICELLI, S. D. 2013. Modeling dendritic solidification of Al–3%Cu using cellular automaton and phase-field methods. *Applied Mathematical Modelling,* 37**,** 3495-3503.

ASTM 2010. Standard Terminology for Additive Manufacturing Technologies. *F2792.*

BOETTINGER, W. J. Growth Kinetic Limitations during Rapid Solidification. Materials Research Society Symposia Proceedings, 1982. 15-31.

BOETTINGER, W. J., WARREN, J. A., BECKERMANN, C. & KARMA, A. 2002. Phase-Field Simulation of Solidification. *Annual Review of Materials Research,* 32**,** 163-194.

BOLEY, C. D., KHAIRALLAH, S. A. & RUBENCHIK, A. M. 2015. Calculation of laser absorption by metal powders in additive manufacturing. *Applied Optics,* 54**,** 2477-2482.

CAROZZANI, T., DIGONNET, H. & CH, A. G. 2012. 3D CAFE modeling of grain structures: application to primary dendritic and secondary eutectic solidification. *Modelling and Simulation in Materials Science and Engineering,* 20**,** 015010.

CHEN, L.-Q. 2002. Phase-Field Models for Microstructure Evolution. *Annual Review of Materials Research,* 32**,** 113-140.

CHLEBUS, E., KUŹNICKA, B., KURZYNOWSKI, T. & DYBAŁA, B. 2011. Microstructure and mechanical behaviour of Ti—6Al—7Nb alloy produced by selective laser melting. *Materials Characterization,* 62**,** 488-495.

COX, D. R. & REID, N. 2000. *The Theory of the Design of Experiments*, Chapman and Hall/CRC.

DANTZIG, J. A. & RAPPAZ, M. 2009. *Solidification*, EFPL Press.

DAS, A. & FAN, Z. 2004. A Monte Carlo simulation of solidification structure formation under melt shearing. *Materials Science and Engineering: A,* 365**,** 330-335.

DAS, S. 2003. Physical Aspects of Process Control in Selective Laser Sintering of Metals. *Advanced Engineering Materials,* 5**,** 701-711.

DESBIOLLES, J. L., DROUX, J. J., RAPPAZ, J. & RAPPAZ, M. 1987. Simulation of solidification of alloys by the finite element method. *Computer Physics Reports,* 6**,** 371-383.

ESHRAGHI, M., FELICELLI, S. D. & JELINEK, B. 2012. Three dimensional simulation of solutal dendrite growth using lattice Boltzmann and cellular automaton methods. *Journal of Crystal Growth,* 354**,** 129-134.

FALLAH, V., AMOOREZAEI, M., PROVATAS, N., CORBIN, S. F. & KHAJEPOUR, A. 2012. Phase-field simulation of solidification morphology in laser powder deposition of Ti–Nb alloys. *Acta Materialia,* 60**,** 1633-1646.

FISCHER, P., KARAPATIS, N., ROMANO, V., GLARDON, R. & WEBER, H. P. 2002. A model for the interaction of near-infrared laser pulses with metal powders in selective laser sintering. *Applied Physics A,* 74**,** 467-474.

FOROOZMEHR, A., BADROSSAMAY, M., FOROOZMEHR, E. & GOLABI, S. I. 2016. Finite Element Simulation of Selective Laser Melting process considering Optical Penetration Depth of laser in powder bed. *Materials & Design,* 89**,** 255-263.

FRANS, K. J. G., RAABE, D., NESTLER, B., KOZESCHNIK, E. & MIODOWNIK, M. A. 2007. *Computational Materials Engineering: An Introduction to Microstructure Evolution*, Elsevier.

GANDIN, C.-A., DESBIOLLES, J. L., RAPPAZ, M. & THEVOZ, P. 1999. A Three-Dimensional Cellular Automaton - Finite Element Model for the Prediction of Solidification Grain Structures. *Metallurgical and Materials Transactions A,* 30A**,** 3153-3165.

GANDIN, C.-A. & RAPPAZ, M. 1994. A Coupled Finite Element - Cellular Automaton Model for the Prediction of Dendritic Grain Structures in Solidification Processes. *Acta Materialia,* 42**,** 2233-2246.

GANDIN, C. A. & RAPPAZ, M. 1997. A 3D Cellular Automaton algorithm for the prediction of dendritic grain growth. *Acta Materialia,* 45**,** 2187-2195.

GOULETTE, M., SPILLING, P. & ARTHEY, R. 1986. *Cost effective single crystals*, Rolls-Royce Limited.

GUO-FENG, Y. & GUANG-NAN, C. 2004. Numerical simulation of transient thermal field in laser melting process. *Applied Mathematics and Mechanics,* 25**,** 945-950.

GUSAROV, A. V. & SMUROV, I. 2009. Two-dimensional numerical modelling of radiation transfer in powder beds at selective laser melting. *Applied Surface Science,* 255**,** 5595-5599.

GUSAROV, A. V. & SMUROV, I. 2010. Modeling the interaction of laser radiation with powder bed at selective laser melting. *Physics Procedia,* 5, Part B**,** 381-394.

GUSAROV, A. V., YADROITSEV, I., BERTRAND, P. & SMUROV, I. 2007. Heat transfer modelling and stability analysis of selective laser melting. *Applied Surface Science,* 254**,** 975-979.

HARRISON, N. J., TODD, I. & MUMTAZ, K. 2015. Reduction of micro-cracking in nickel superalloys processed by Selective Laser Melting: A fundamental alloy design approach. *Acta Materialia,* 94**,** 59-68.

ION, J. 2005. *Laser Processing of Engineering Materials: Principles, Procedure and Industrial Application*, Elsevier Science.

JACKSON, K. A. 1984. Crystal growth kinetics. *Materials Science and Engineering,* 65**,** 7-13.

JACKSON, K. A. & HUNT, J. D. 1966. Lamellar and rod eutectic growth. *Transactions of the Metallurgical Society of AIME,* 236**,** 1129-1142.

JACOBSON, L. A. & MCKITTRICK, J. 1994. Rapid solidification processing. *Materials Science and Engineering: R: Reports,* 11**,** 355-408.

JANSSENS, K., FRANS, G., RAABE, D., NESTLER, B., KOZESCHNIK, E. & MIODOWNIK, M. A. 2007. *Computational Materials Engineering: An Introduction to Microstructure Evolution*, Elsevier.

JELINEK, B., ESHRAGHI, M., FELICELLI, S. & PETERS, J. F. Large-scale parallel lattice Boltzmann—Cellular automaton model of two-dimensional dendritic growth. *Computer Physics Communications*.

KEMPEN, K., VRANCKEN, B., BULS, S., THIJS, L., HUMBEECK, J. V. & KRUTH, J.-P. 2014. Selective Laser Melting of Crack-Free High Density M2 High Speed Steel Parts by Baseplate Preheating. *Journal of Manufacturing Science and Engineering,* 136.

KHAIRALLAH, S. A. & ANDERSON, A. 2014. Mesoscopic simulation model of selective laser melting of stainless steel powder. *Journal of Materials Processing Technology,* 214**,** 2627-2636.

KIER, L. B., SEYBOLD, P. G. & CHENG, C.-K. 2005. *Cellular Automata Modeling of Chemical Systems*, Springer.

KÖRNER, C., ATTAR, E. & HEINL, P. 2011. Mesoscopic simulation of selective beam melting processes. *Journal of Materials Processing Technology,* 211**,** 978-987.

KOSEKI, T., INOUE, H., FUKUDA, Y. & NOGAMI, A. 2003. Numerical simulation of equiaxed grain formation in weld solidification. *Science and Technology of Advanced Materials,* 4**,** 183-195.

KREMEYER, K. 1998. Cellular Automata Investigations of Binary Solidification. *Journal of Computational Physics,* 142**,** 243-262.

KRUTH, J. P., FROYEN, L., VAN VAERENBERGH, J., MERCELIS, P., ROMBOUTS, M. & LAUWERS, B. 2004. Selective laser melting of iron-based powder. *Journal of Materials Processing Technology,* 149**,** 616-622.

KRUTH, J. P., LEVY, G., KLOCKE, F. & CHILDS, T. H. C. 2007. Consolidation phenomena in laser and powder-bed based layered manufacturing. *CIRP Annals - Manufacturing Technology,* 56**,** 730-759.

KURZ, W. & FISHER, D. J. 1998. *Fundamentals of Solidification*, Trans Tech Publications LTD.

KURZ, W., GIOVANOLA, B. & TRIVEDI, R. 1986. Theory of microstructural development during rapid solidification. *Acta Metallurgica,* 34**,** 823-830.

KURZ, W. & TRIVEDI, R. 1994. Proceedings of the Eighth International Conference on Rapidly Quenched and Metastable Materials Rapid solidification processing and microstructure formation. *Materials Science and Engineering: A,* 179**,** 46-51.

LANGER, J. S. & MÜLLER-KRUMBHAAR, J. 1977. Stability effects in dendritic crystal growth. *Journal of Crystal Growth,* 42**,** 11-14.

LAUBITZ, M. J. 1959. Thermal Conductivity of Powders. *Can. J. Physics,* 37**,** 798-808.

LAVERNIA, E. & SRIVATSAN, T. S. 2010. The rapid solidification processing of materials: science, principles, technology, advances, and applications. *Journal of Materials Science,* 45**,** 287-325.

LI, R., LIU, J., SHI, Y., WANG, L. & JIANG, W. 2012. Balling behavior of stainless steel and nickel powder during selective laser melting process. *The International Journal of Advanced Manufacturing Technology,* 59**,** 1025-1035.

LIPTON, J., GLICKSMAN, M. E. & KURZ, W. 1987. Equiaxed dendrite growth in alloys at small supercooling. *Metallurgical Transactions A,* 18**,** 341-345.

LIU, Q., DANLOS, Y., SONG, B., ZHANG, B., YIN, S. & LIAO, H. 2015. Effect of high-temperature preheating on the selective laser melting of yttria-stabilized zirconia ceramic. *Journal of Materials Processing Technology,* 222**,** 61-74.

LOEB, A. L. 1954. Thermal Conductivity: VIII, A Theory of Thermal Conductivity of Porous Materials. *Journal of the American Ceramic Society,* 37**,** 96-99.

LOH, L.-E., CHUA, C.-K., YEONG, W.-Y., SONG, J., MAPAR, M., SING, S.-L., LIU, Z.-H. & ZHANG, D.-Q. 2015. Numerical investigation and an effective modelling on the Selective Laser Melting (SLM) process with aluminium alloy 6061. *International Journal of Heat and Mass Transfer,* 80**,** 288-300.

LUIKOV, A. V. 1971. *A.V. Luikov Presentation Volume*.

MARTORANO, M. A., BECKERMANN, C. & CH, A. G. 2003. A Solutal Interaction Mechanism for the Columnar-to-Equiaxed Transition in Alloy Solidification. *Metallurgical and Materials Transactions A,* 34A**,** 1657-1674.

MATSUMOTO, M., SHIOMI, M., OSAKADA, K. & ABE, F. 2002. Finite element analysis of single layer forming on metallic powder bed in rapid prototyping by selective laser processing. *International Journal of Machine Tools and Manufacture,* 42**,** 61-67.

MCCARTNEY, D. G. & WILLS, V. A. 1988. A finite element model of alloy solidification incorporating velocity-dependent growth temperatures. *Applied Mathematical Modelling,* 12**,** 354-361.

MILLS, K. C. 2002. *Recommended Values of Thermophysical Properties for Selected Commercial Alloys*.

MILLS, K. C., KEENE, B. J., BROOKS, R. F. & SHIRALI, A. 1998. Marangoni effects in welding. *Philosophical Transactions of the Royal Society of London A: Mathematical, Physical and Engineering Sciences,* 356**,** 911-925.

MOHANTY, S. & HATTEL, J. H. 2014. Numerical Model based Reliability Estimation of Selective Laser Melting Process. *Physics Procedia,* 56**,** 379-389.

MUMTAZ, K. & HOPKINSON, N. 2010. Selective laser melting of Inconel 625 using pulse shaping. *Rapid Prototyping Journal,* 16**,** 248-257.

PLAPP, M. & KARMA, A. 2000. Multiscale Finite-Difference-Diffusion-Monte-Carlo Method for Simulating Dendritic Solidification. *Journal of Computational Physics,* 165**,** 592-619.

POWLEY, T. 2015. Rise of the 3D printing machines. *The Financial Times.* www.ft.com.

RAABE, D. 1998. *Computational Materials Science*, Wiley-VCH.

RAABE, D. 2002. Cellular Automata in Materials Science with particular reference to Recrystallization Simulation. *Annual Review of Materials Research.*

RAO, S. S. 2011. *The Finite Element Method in Engineering*, Elsevier.

RAPPAZ, M. 1989. Modelling of microstructure formation in solidification processes. *International Materials Reviews,* 34**,** 93-124.

ROBERTS, I. A., WANG, C. J., ESTERLEIN, R., STANFORD, M. & MYNORS, D. J. 2009. A three-dimensional finite element analysis of the temperature field during laser melting of metal powders in additive layer manufacturing. *International Journal of Machine Tools and Manufacture,* 49**,** 916-923.

SAFDAR, S., PINKERTON, A. J., LI, L., SHEIKH, M. A. & WITHERS, P. J. 2013. An anisotropic enhanced thermal conductivity approach for modelling laser melt pools for Ni-base super alloys. *Applied Mathematical Modelling,* 37**,** 1187-1195.

SANDS, D. 2007. New theory of undercooling during rapid solidification: application to pulsed laser heated silicon. *Applied Physics A,* 88**,** 179-189.

SEMMA, E., EL GANAOUI, M., BENNACER, R. & MOHAMAD, A. A. 2008. Investigation of flows in solidification by using the lattice Boltzmann method. *International Journal of Thermal Sciences,* 47**,** 201-208.

SEMMA, E. A., EL GANAOUI, M. & BENNACER, R. 2007. Lattice Boltzmann method for melting/solidification problems. *Comptes Rendus Mécanique,* 335**,** 295-303.

SHEN, Z. H., ZHANG, S. Y., LU, J. & NI, X. W. 2001. Mathematical modeling of laser induced heating and melting in solids. *Optics & Laser Technology,* 33**,** 533-537.

SHIOMI, M., YOSHIDOME, A., ABE, F. & OSAKADA, K. 1999. Finite element analysis of melting and solidifying processes in laser rapid prototyping of metallic powders. *International Journal of Machine Tools and Manufacture,* 39**,** 237-252.

SIH, S. S. & BARLOW, J. W. Measurement and Prediction of the Thermal Conductivity of Powders at High Temperature. 5th Annual SFF Symposium, 1994 The University of Texas at Austin. 321-329.

SONG, B., DONG, S., LIAO, H. & CODDET, C. 2012. Process parameter selection for selective laser melting of Ti6Al4V based on temperature distribution simulation and experimental sintering. *The International Journal of Advanced Manufacturing Technology,* 61**,** 967-974.

STEEN, W. M. & MAZUMDER, J. 2010. *Laser Material Processing*, Springer-Verlag London.

SUN, D. K., ZHU, M. F., PAN, S. Y., YANG, C. R. & RAABE, D. 2011. Lattice Boltzmann modeling of dendritic growth in forced and natural convection. *Computers & Mathematics with Applications,* 61**,** 3585-3592.

SZPUNAR, B. & SMITH, R. W. 1996. Monte Carlo simulation of solidification processes; Porosity. *Canadian Metallurgical Quarterly,* 35**,** 299-303.

TAN, W., BAILEY, N. S. & SHIN, Y. C. 2011. A novel integrated model combining Cellular Automata and Phase Field methods for microstructure evolution during solidification of multi-component and multi-phase alloys. *Computational Materials Science,* 50**,** 2573-2585.

TOLOCHKO, N. K., KHLOPKOV, Y. V., MOZZHAROV, S. E., SOBOLENKO, N. V. & YADROITSEV, I. A. 1997. Measurement of the absorption coefficient of freely poured one-component metallic powders and its change during laser sintering. *Powder Metallurgy and Metal Ceramics,* 36**,** 433-437.

TOLOSA, I., GARCIANDÍA, F., ZUBIRI, F., ZAPIRAIN, F. & ESNAOLA, A. 2010. Study of mechanical properties of AISI 316 stainless steel processed by “selective laser melting”, following different manufacturing strategies. *The International Journal of Advanced Manufacturing Technology,* 51**,** 639-647.

TSAI, D.-C. & HWANG, W.-S. 2010. Numerical simulation of solidification morphologies of Cu-0.6Cr casting alloy using modified cellular automaton model. *Transactions of Nonferrous Metals Society of China,* 20**,** 1072-1077.

WOHLERS 2013. T. Wohlers Report 2013: Additive Manufacturing and 3D Printing State of the Industry: Annual World Wide Progress Report. *In:* ASSOCIATES, W. (ed.).

WOLFRAM, S. 2002. *A New Kind of Science*, Wolfram Media.

WOODSIDE, W. 1958. Calculation of the thermal conductivity of porous media. *Can. J. Physics,* 36**,** 815-823.

YEVKO, V., PARK, C. B., ZAK, G., COYLE, T. W. & BENHABIB, B. 1998. Cladding formation in laser-beam fusion of metal powder. *Rapid Prototyping Journal,* 4**,** 168-184.

YIN, H. & FELICELLI, S. D. 2010. Dendrite growth simulation during solidification in the LENS process. *Acta Materialia,* 58**,** 1455-1465.

YIN, H., FELICELLI, S. D. & WANG, L. 2011. Simulation of a dendritic microstructure with the lattice Boltzmann and cellular automaton methods. *Acta Materialia,* 59**,** 3124-3136.

YOUNG, T. 1805. An Essay on the Cohesion of Fluids. *Philosophical Transactions of the Royal Society of London,* 95**,** 65-87.

YUAN, Y. & LEE, T. R. 2013. Contact Angle and Wetting Properties. *Surface Science Techniques.* Springer-Verlag Berlin Heidelberg.

ZAEEM, M. A., YIN, H. & FELICELLI, S. D. 2012. Comparison of Cellular Automaton and Phase Field Models to Simulate Dendrite Growth in Hexagonal Crystals. *Journal of Materials Science & Technology,* 28**,** 137-146.

ZEHNER, P. & SCHLUNDER, E. U. 1970. Thermal conductivity of granular materials at moderate temperatures (in German). *Chemie Ingr. Tech.***,** 933-941.

ZHAN, X., WEI, Y. & DONG, Z. 2008. Cellular automaton simulation of grain growth with different orientation angles during solidification process. *Journal of Materials Processing Technology,* 208**,** 1-8.

ZHANG, B., DEMBINSKI, L. & CODDET, C. 2013. The study of the laser parameters and environment variables effect on mechanical properties of high compact parts elaborated by selective laser melting 316L powder. *Materials Science and Engineering: A,* 584**,** 21-31.

ZHANG, L. & ZHANG, C.-B. 2006. Two-dimensional cellular automaton model for simulating structural evolution of binary alloys during solidification. *Transactions of Nonferrous Metals Society of China,* 16**,** 1410-1416.

Appendix 1

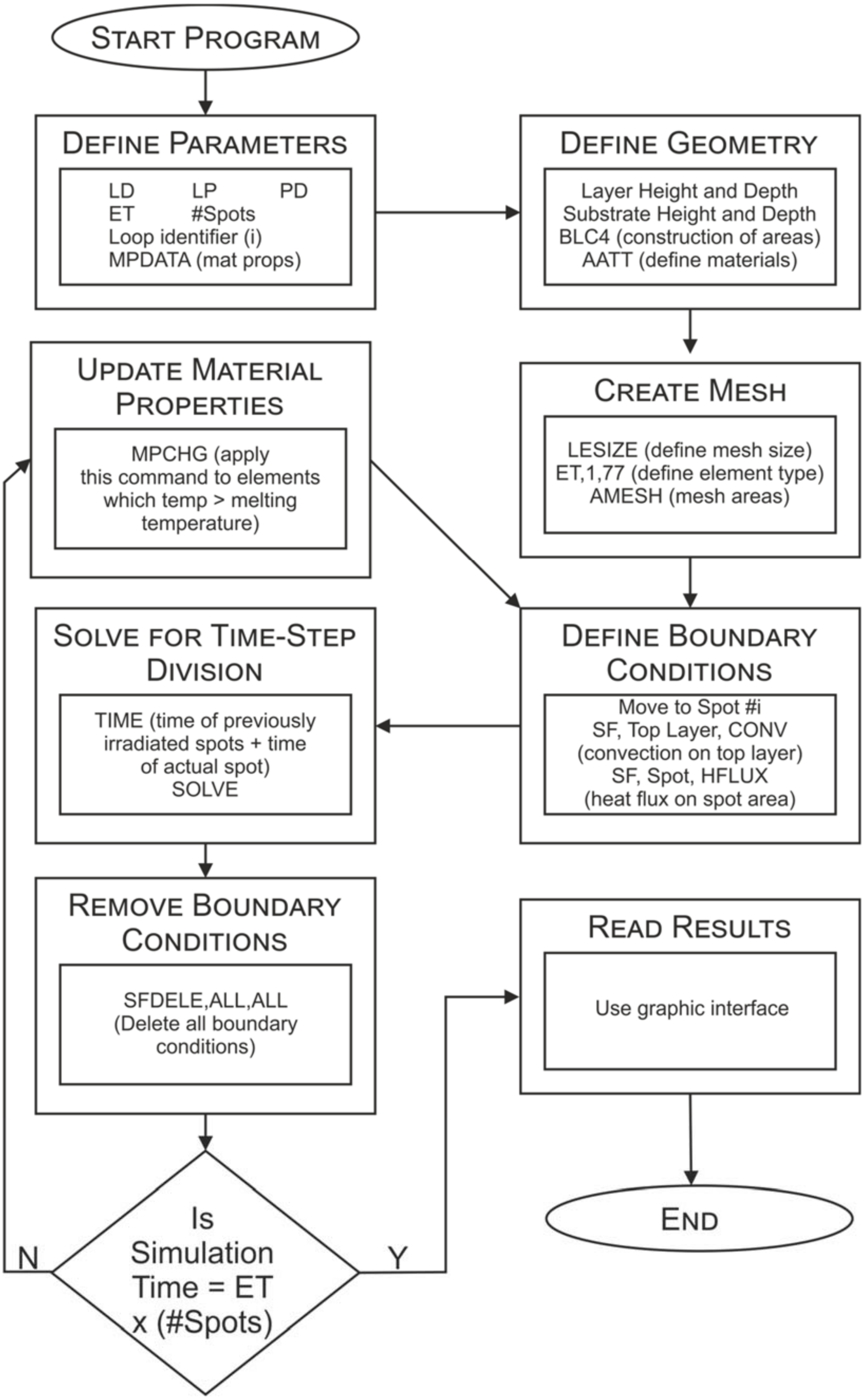

Figure 1. Flow diagram of the single layer FEM model.

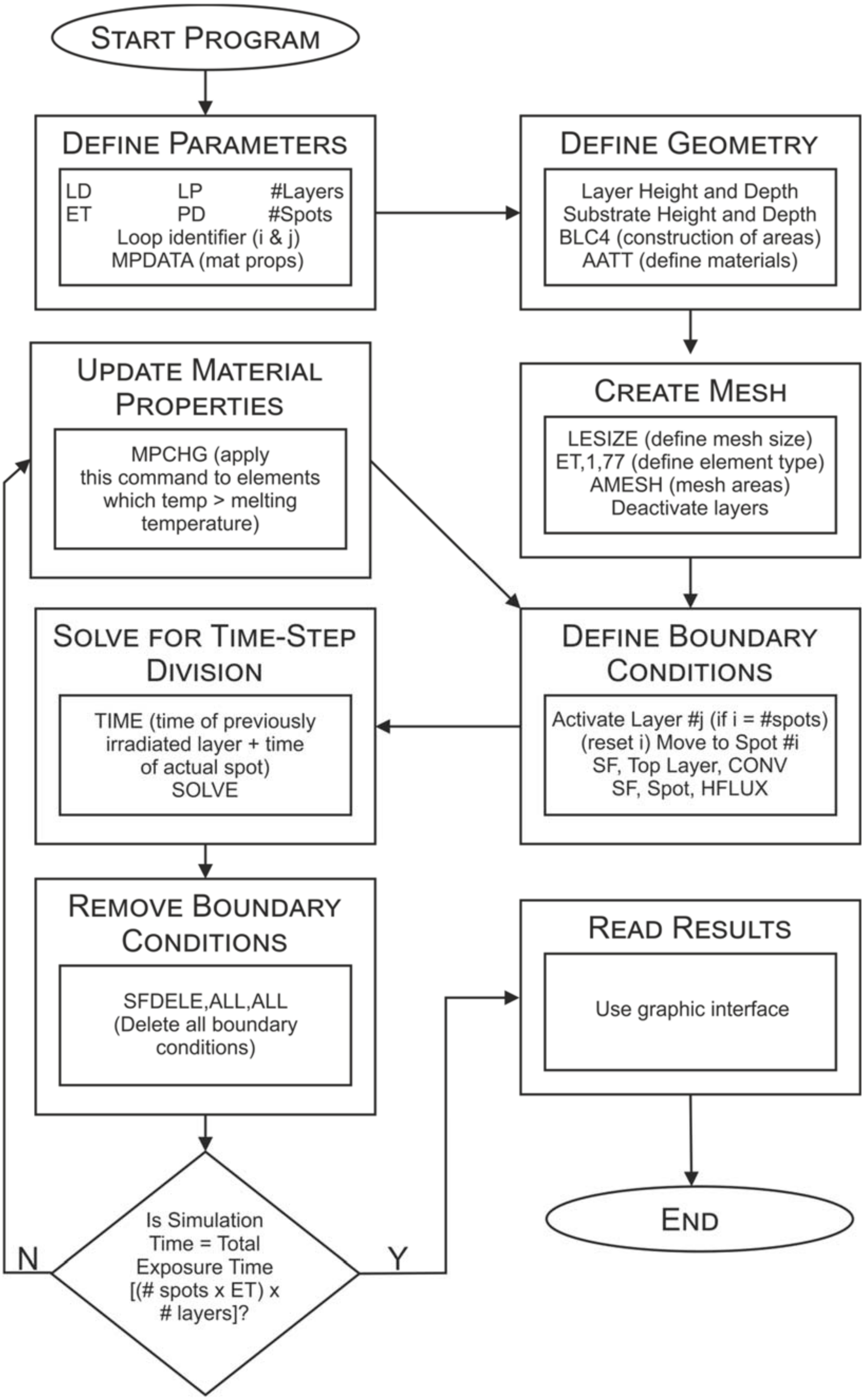

Figure 2. Flow diagram of the layer-by-layer FEM model.

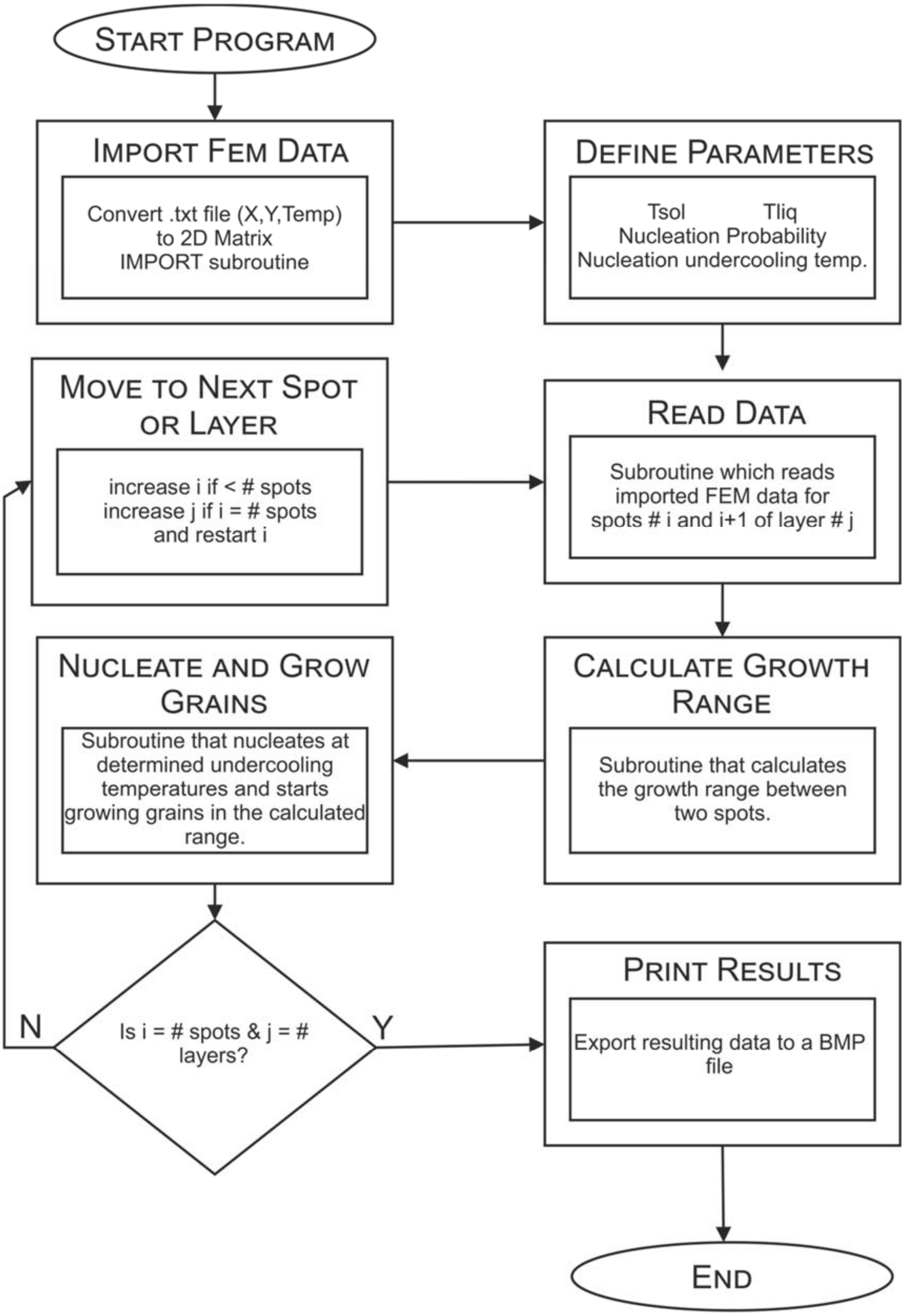

Figure 3. Flow diagram of the CA-FE model.

Appendix 2

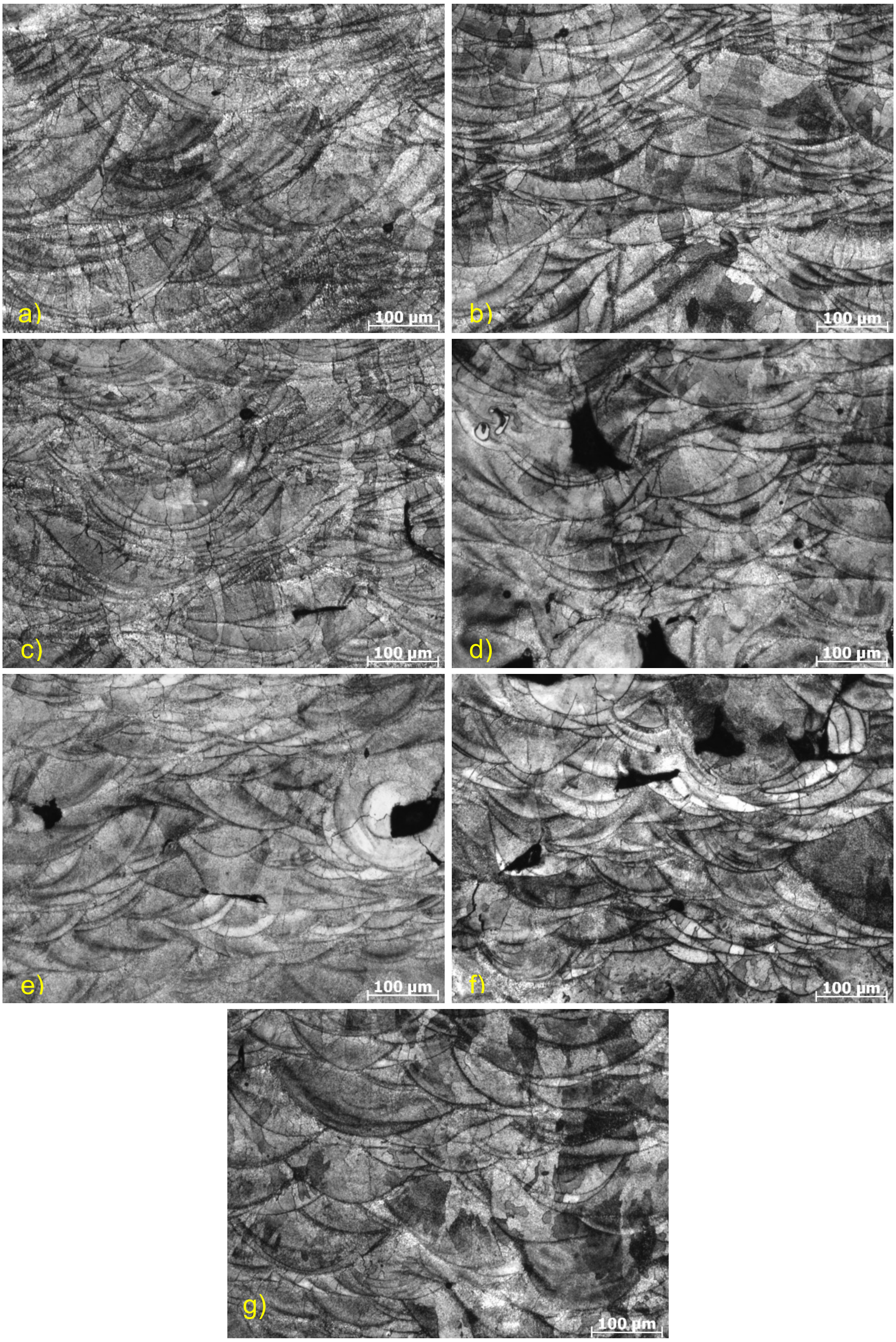

Figure 1. Example of metallographies etched with Keller's reagent of benchmark sample a) 1, b) 2, c) 3, d) 4, e) 5, f) 6 and g) 7.

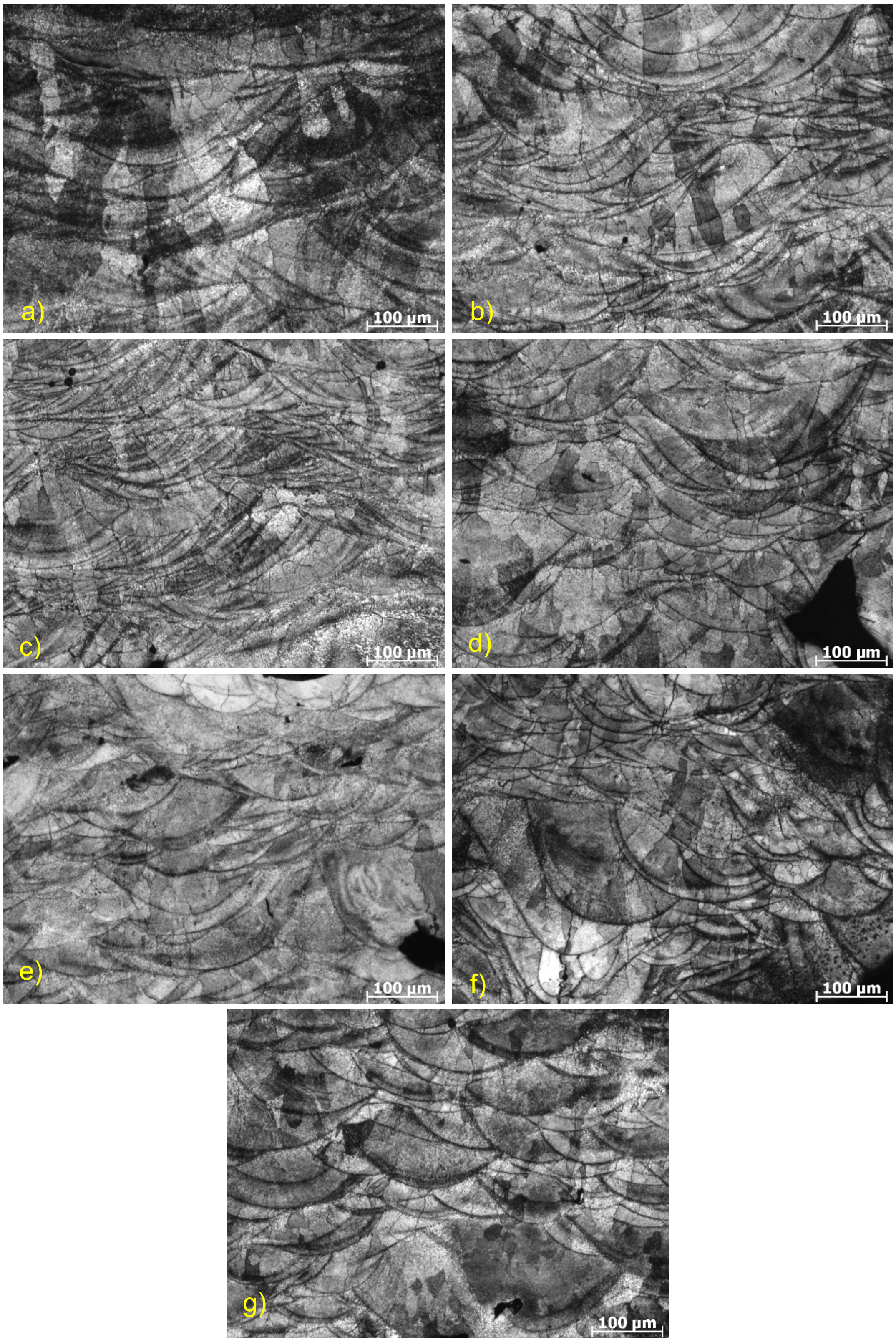

Figure 2. Example of metallographies etched with Keller's reagent of validation sample a) 1, b) 2, c) 3, d) 4, e) 5, f) 6 and g) 7.

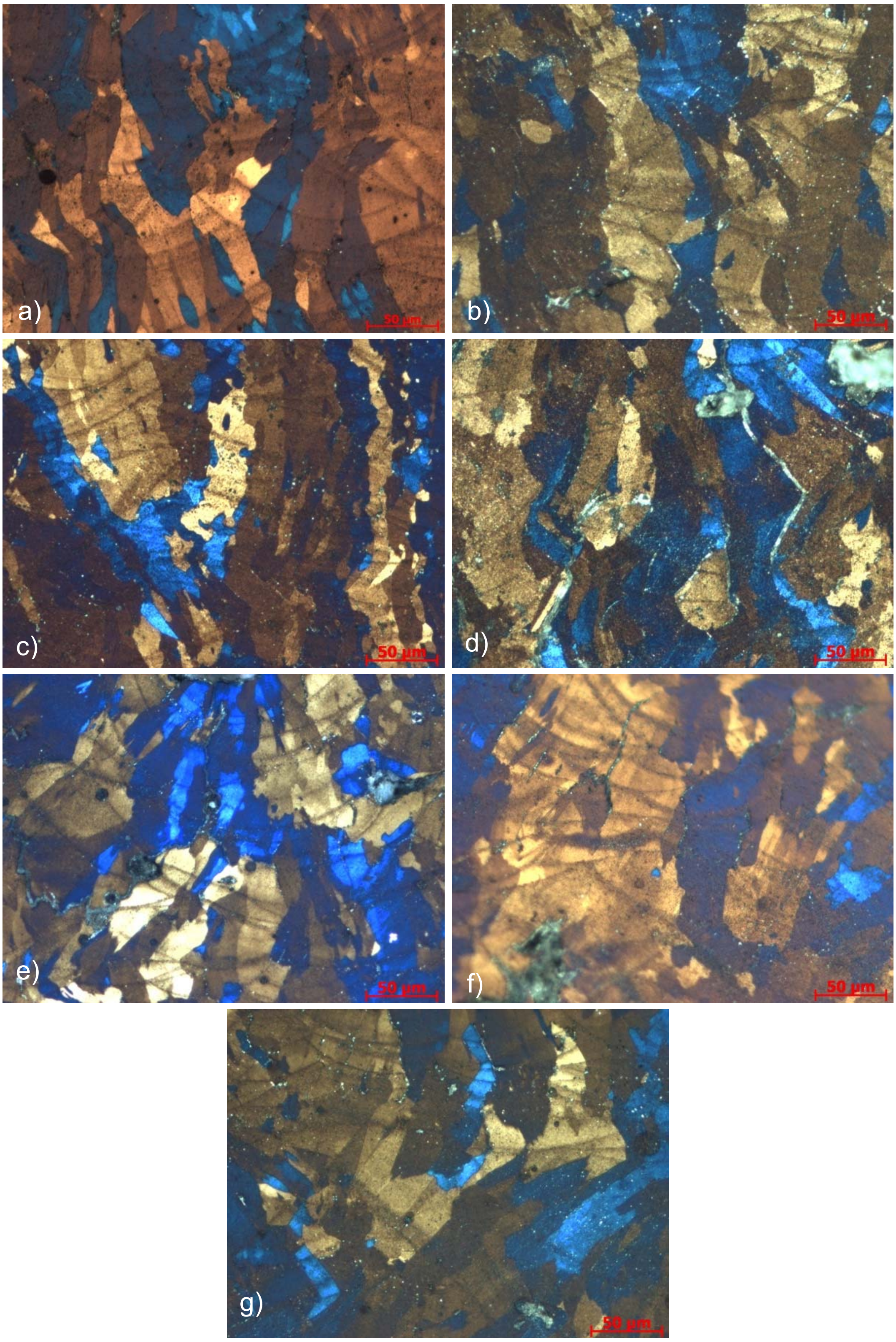

Figure 3. Example of metallographies etched with Barker's reagent of benchmark sample a) 1, b) 2, c) 3, d) 4, e) 5, f) 6 and g) 7.

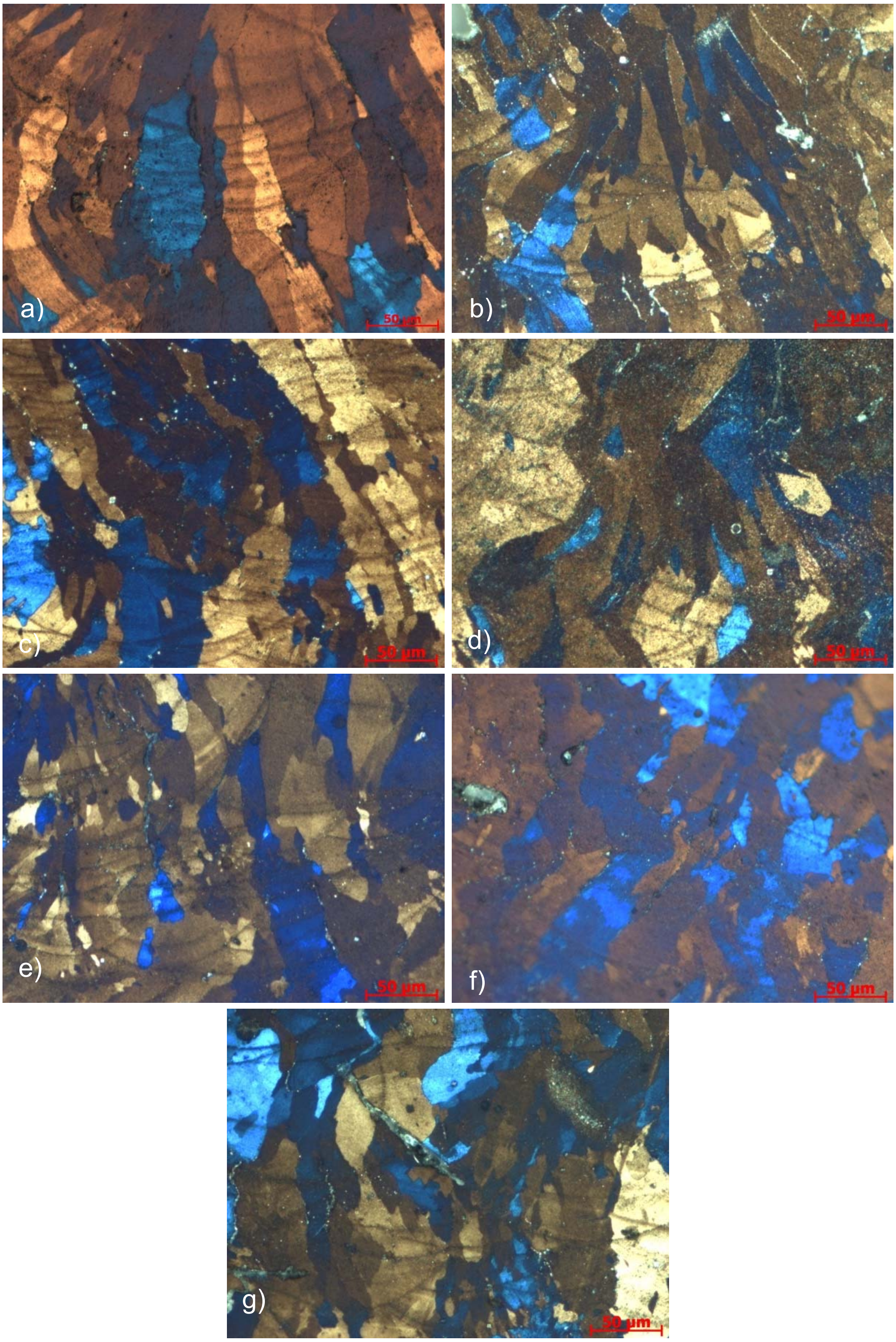

Figure 4. Example of metallographies etched with Barker's reagent of validation sample a) 1, b) 2, c) 3, d) 4, e) 5, f) 6 and g) 7.

Appendix 3

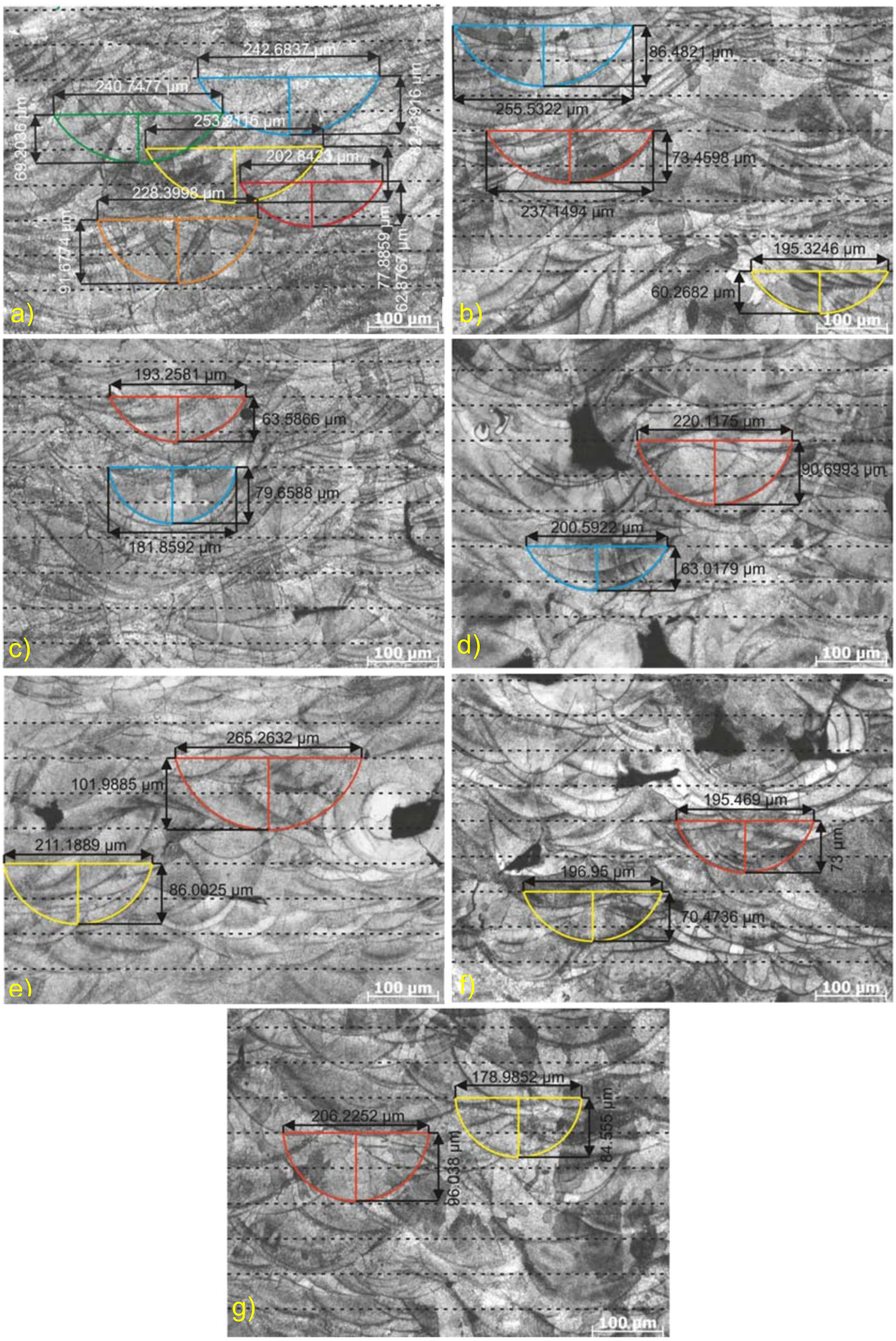

Figure 1. Melt pool measurement example performed to benchmark sample a) 1, b) 2, c) 3, d) 4, e) 5, g) 6 and h) 7.

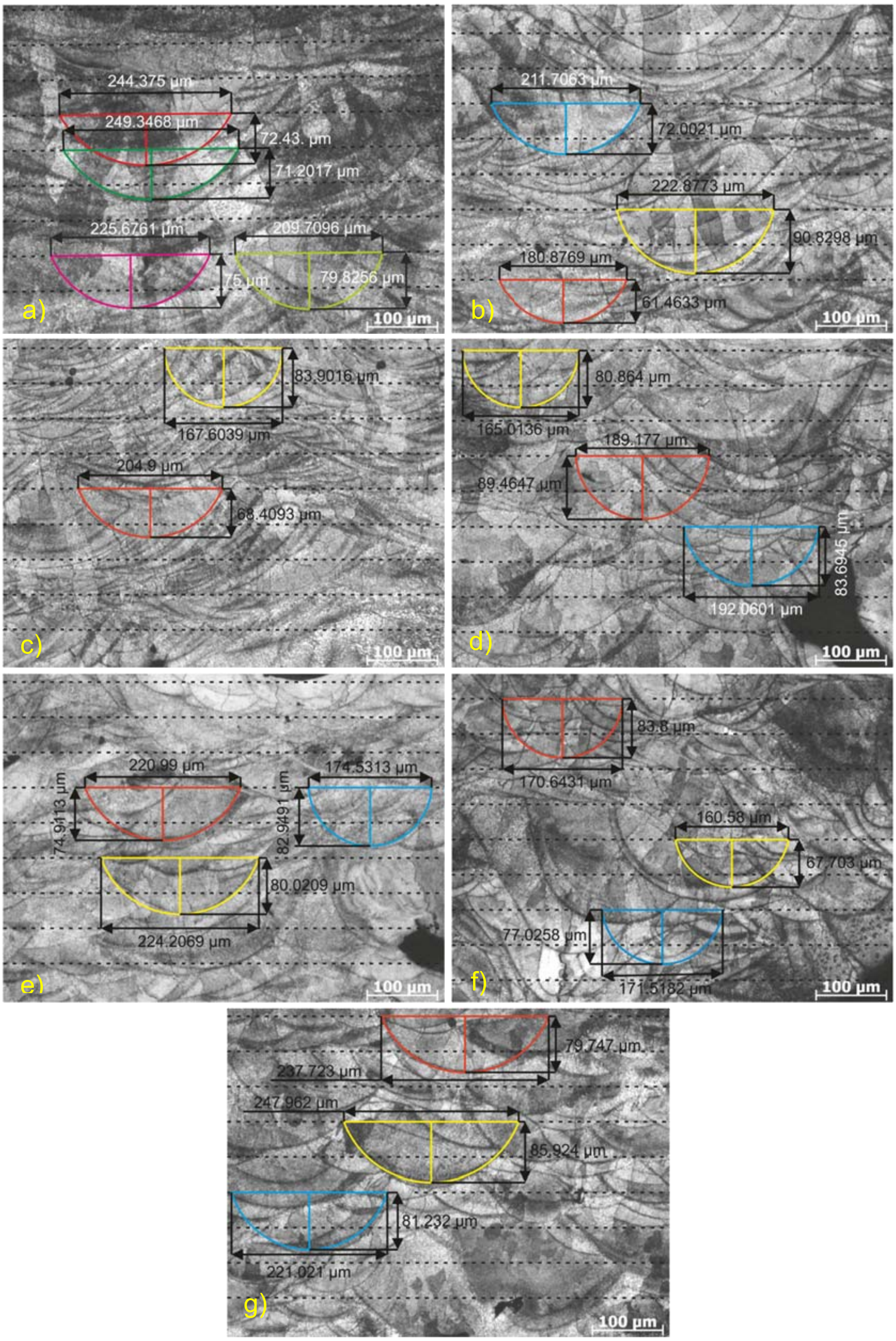

Figure 2. Melt pool measurement example performed to validation sample a) 1, b) 2, c) 3, d) 4, e) 5, g) 6 and h) 7.

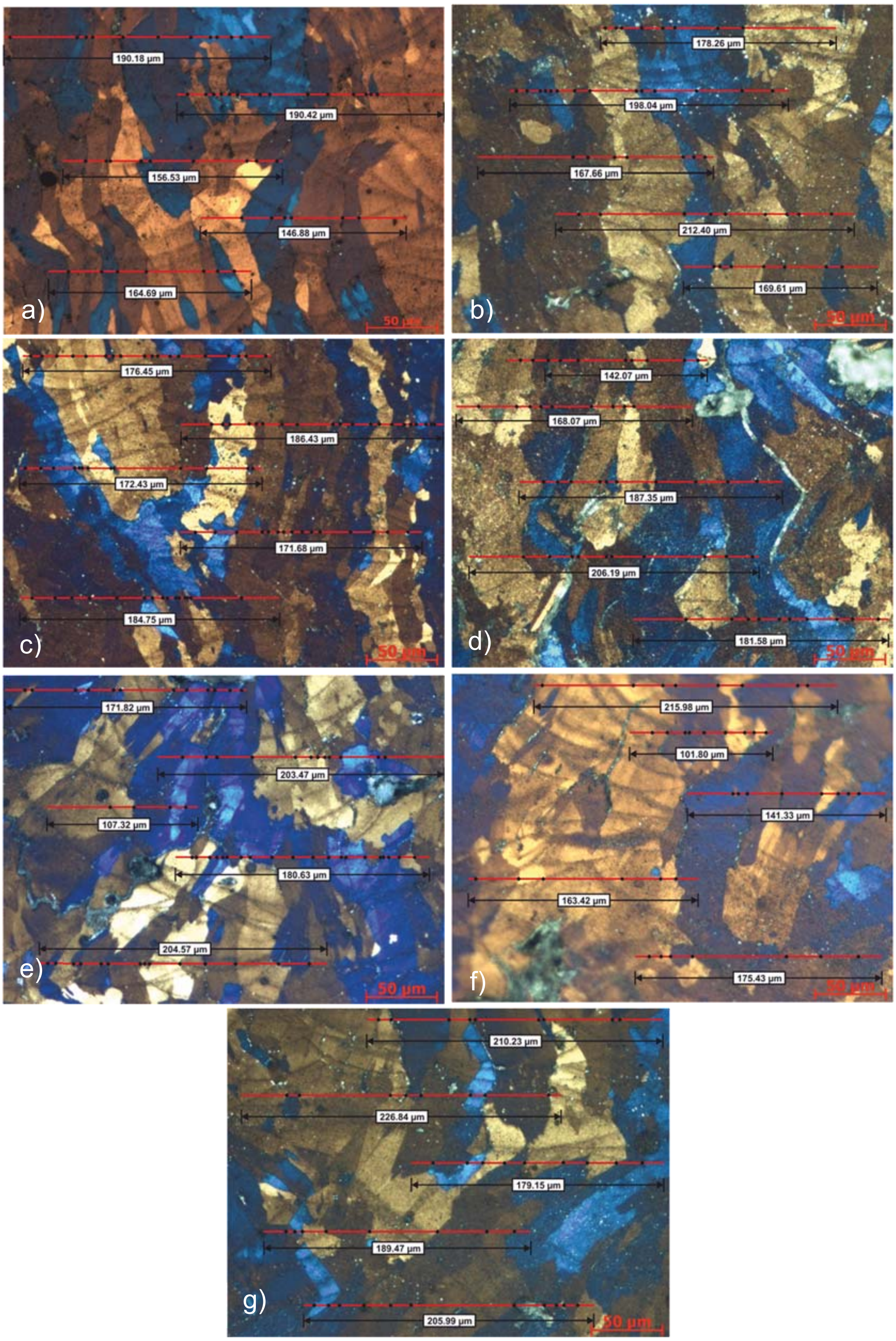

Figure 3. Average grain size measurement example performed to benchmark sample a) 1, b) 2, c) 3, d) 4, e) 5, g) 6 and h) 7.

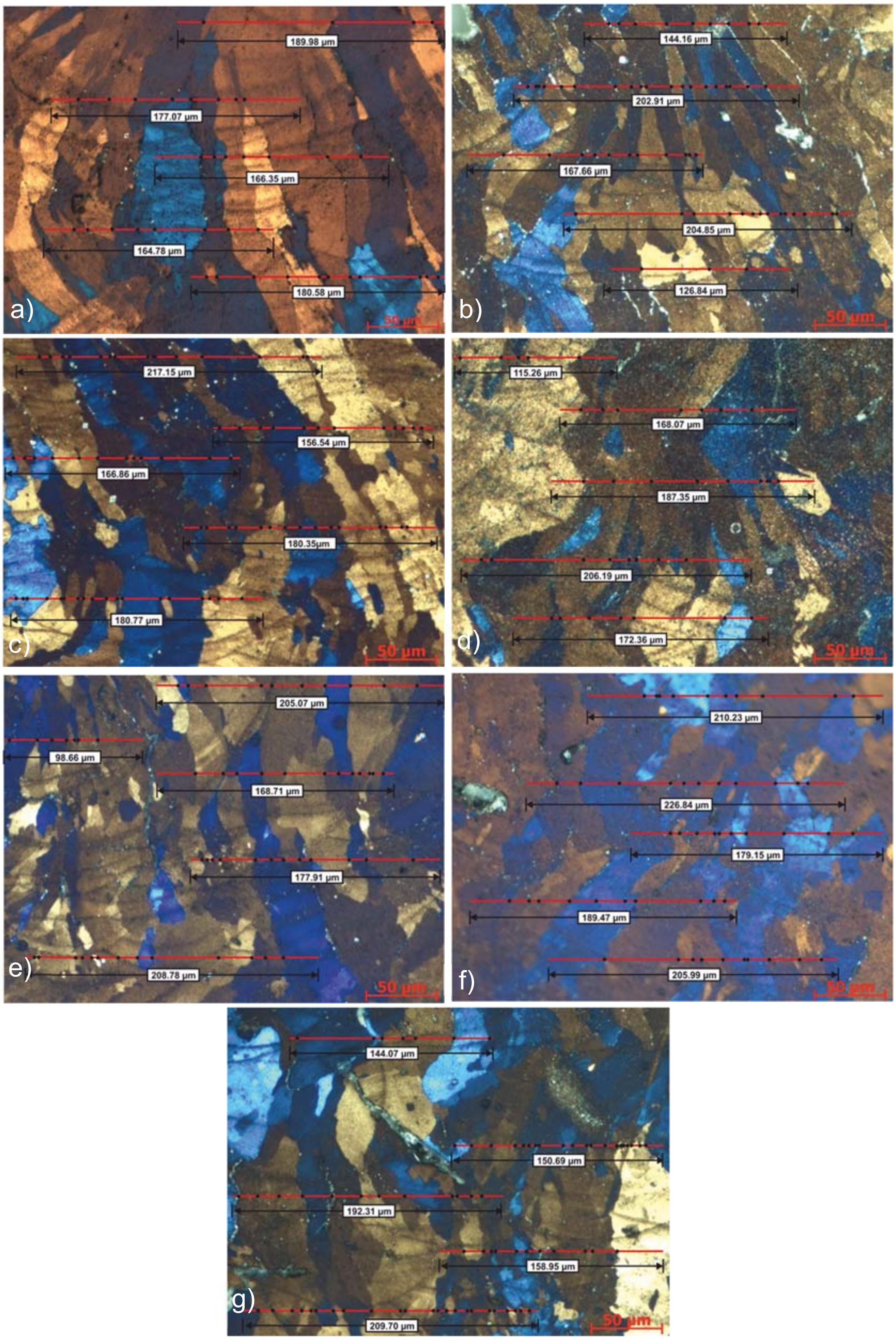

Figure 4. Average grain size measurement example performed to validation sample a) 1, b) 2, c) 3, d) 4, e) 5, g) 6 and h) 7.

Appendix 4

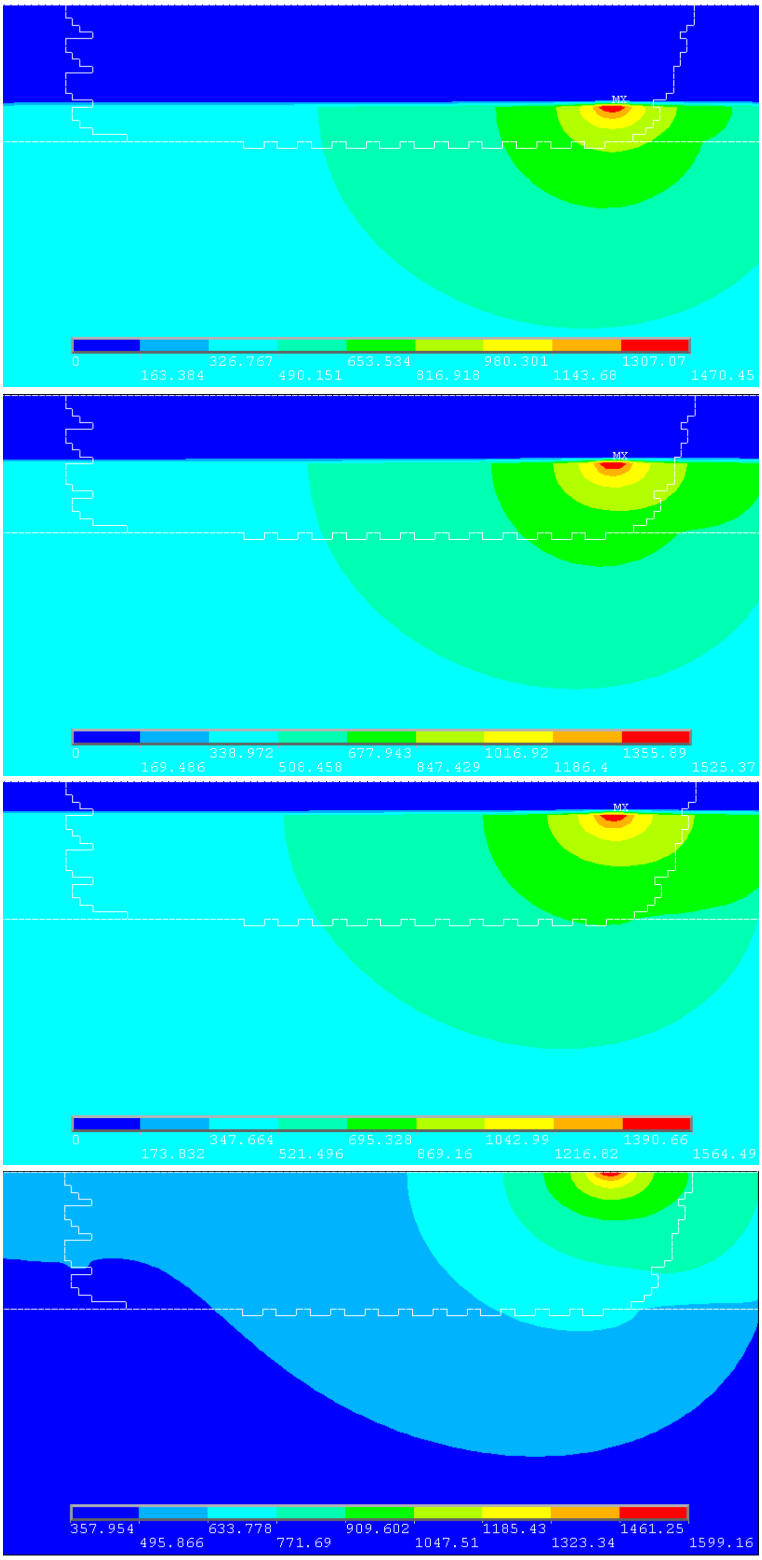

Figure 1. Evolution of the temperature profiles of sample 1 after the deposition of each layer.

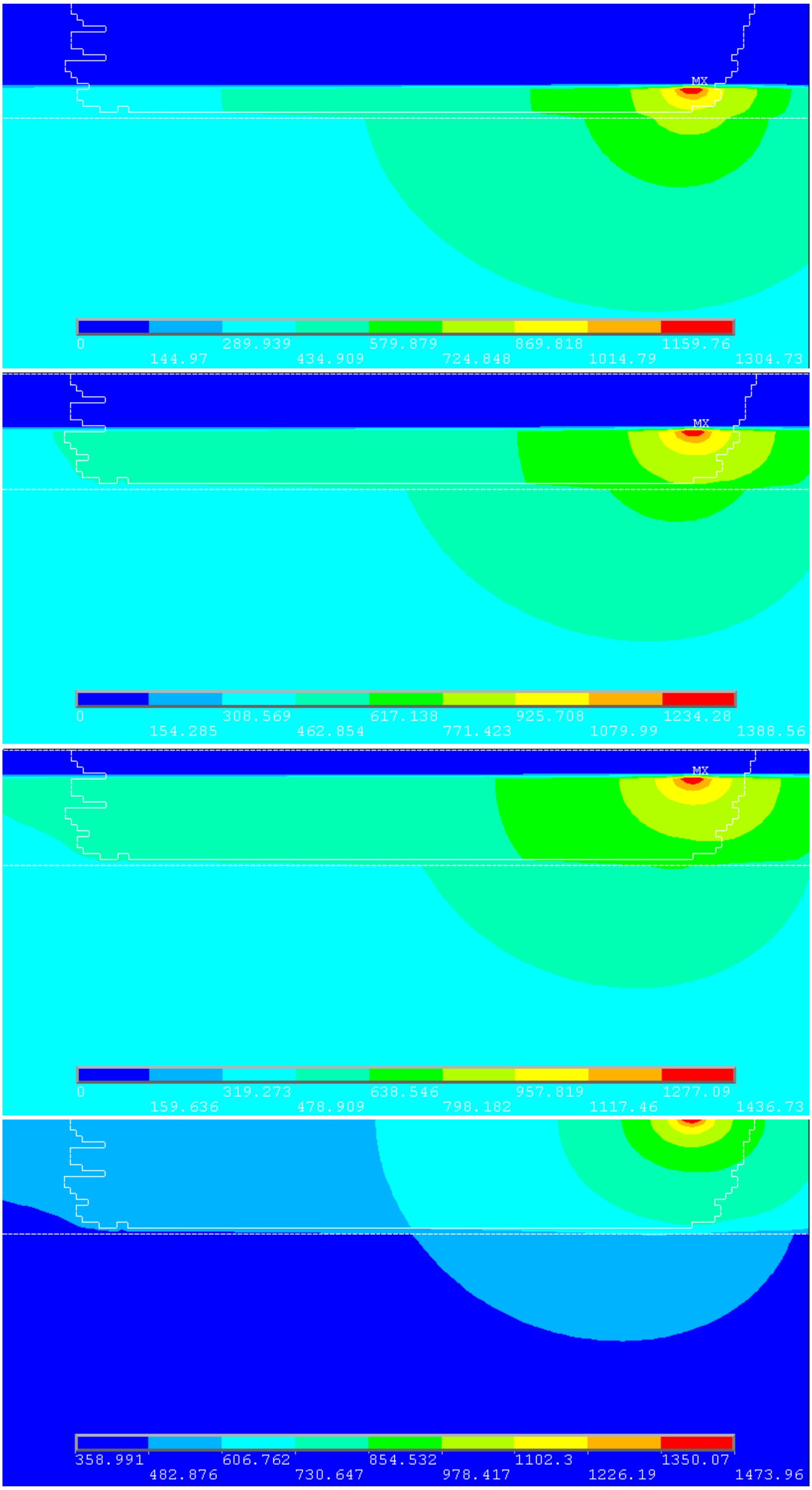

Figure 2. Evoution of the temperature profiles of sample 2.

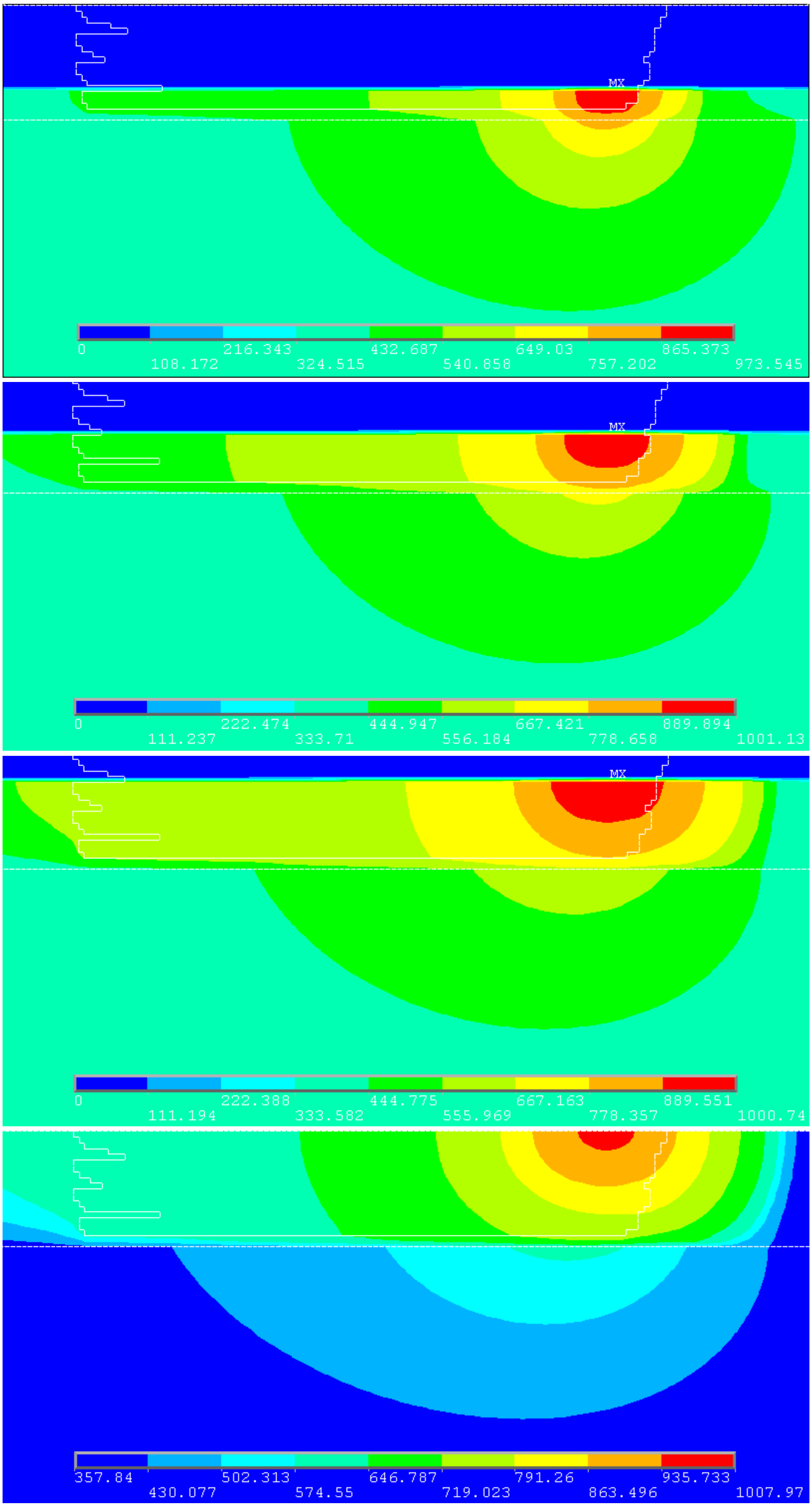

Figure 3. Evoution of the temperature profiles of sample 3.

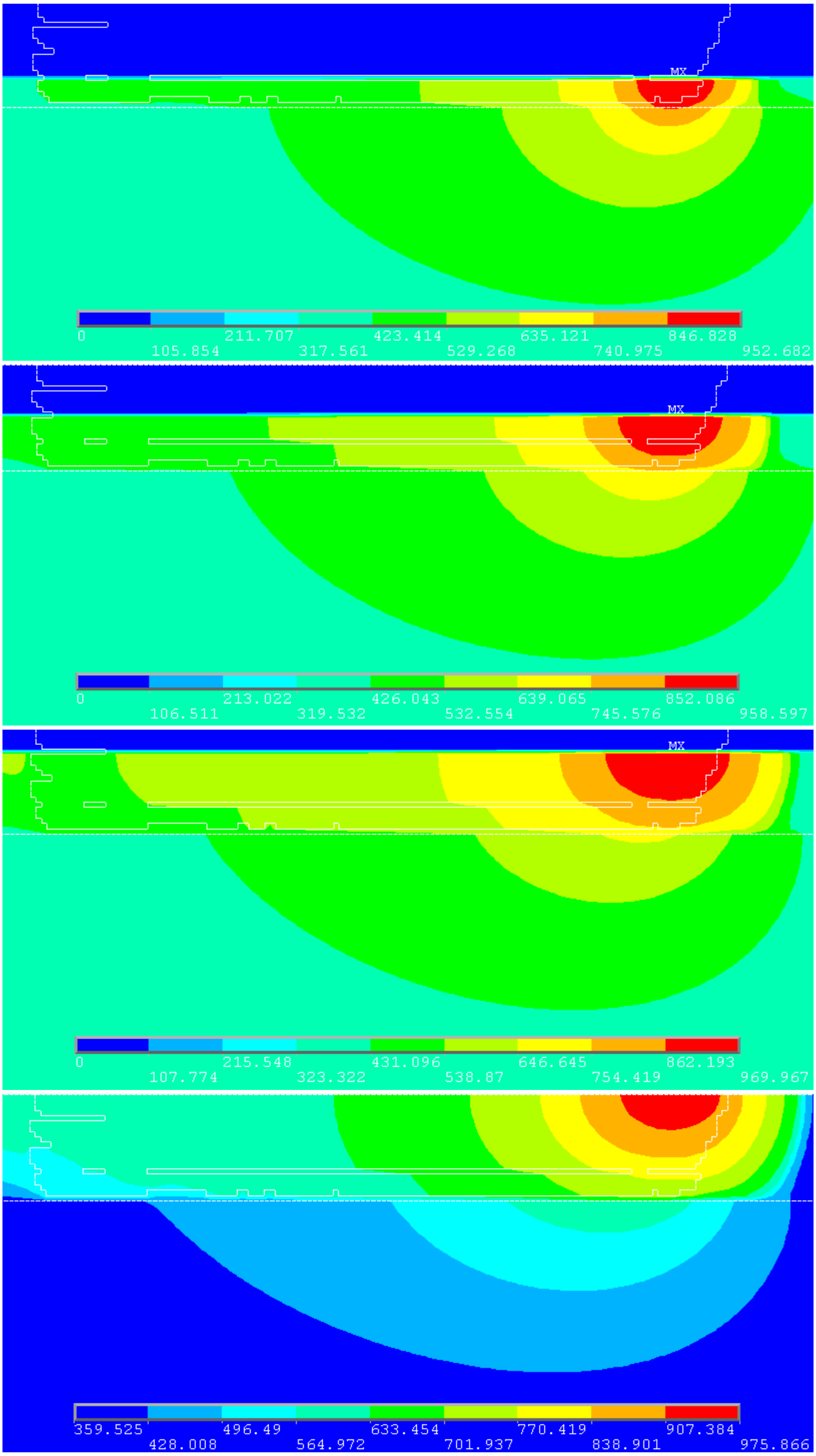

Figure 4. Evoution of the temperature profiles of sample 4.

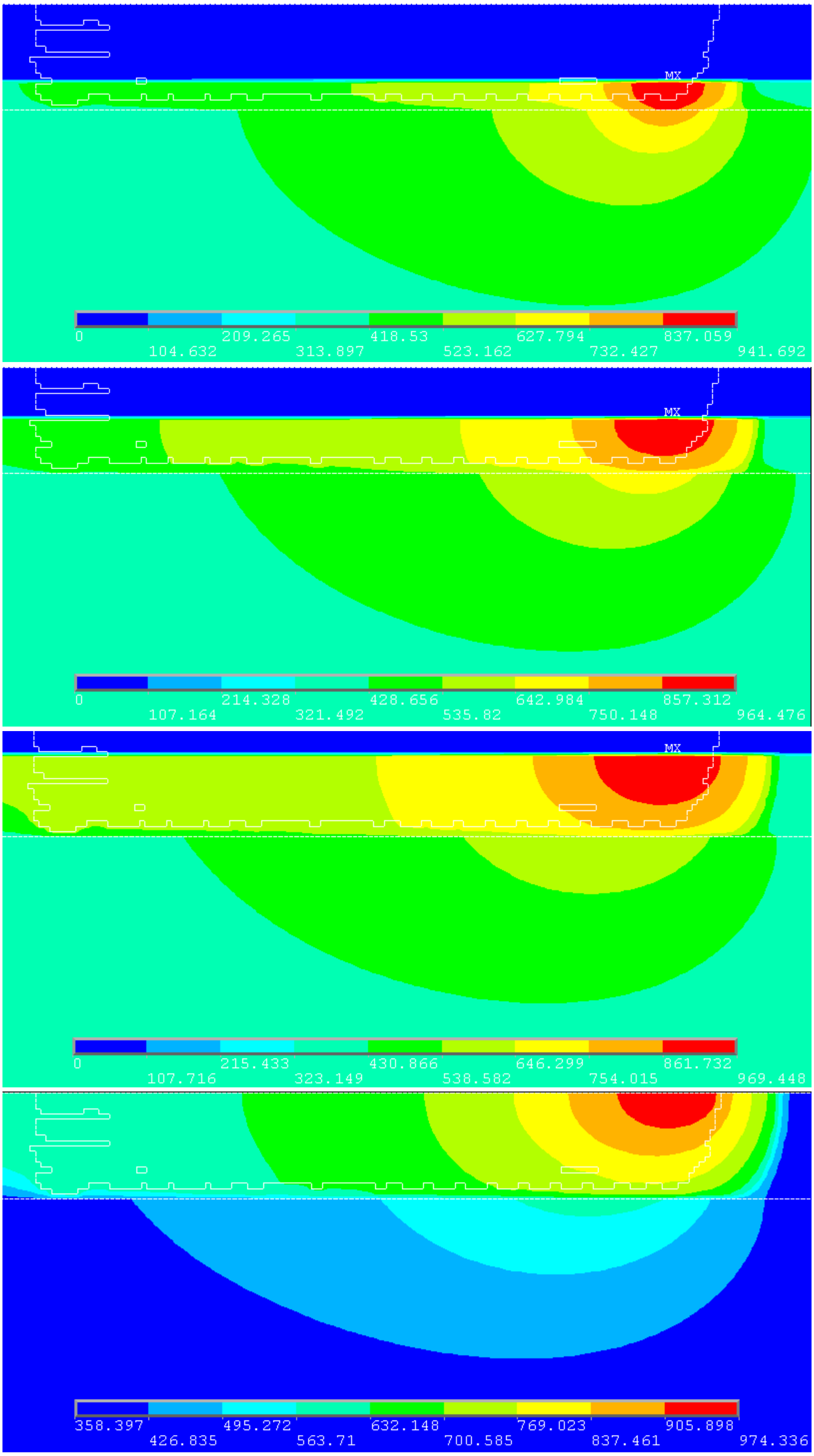

Figure 5. Evoution of the temperature profiles of sample 5.

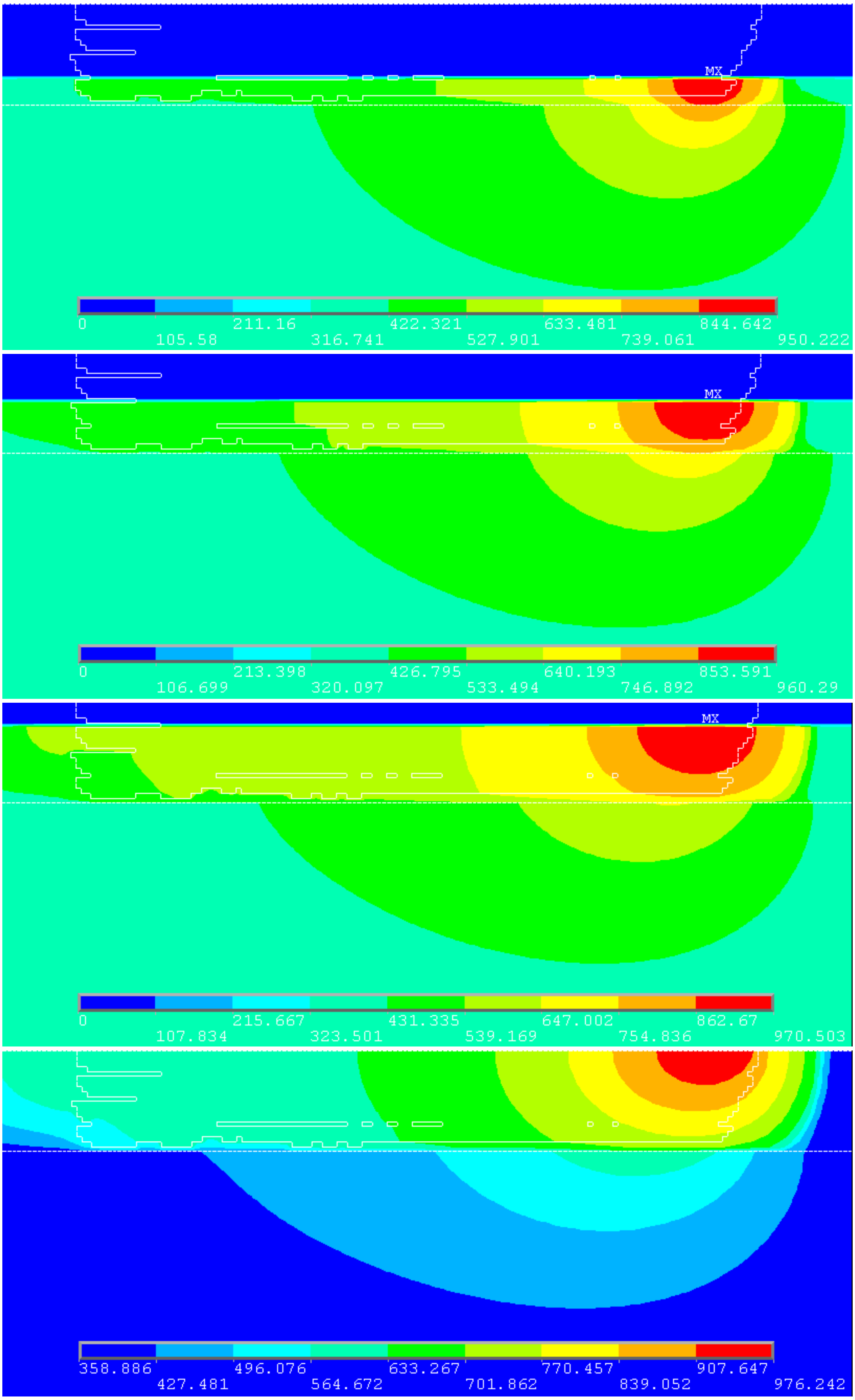

Figure 6. Evoution of the temperature profiles of sample 6.

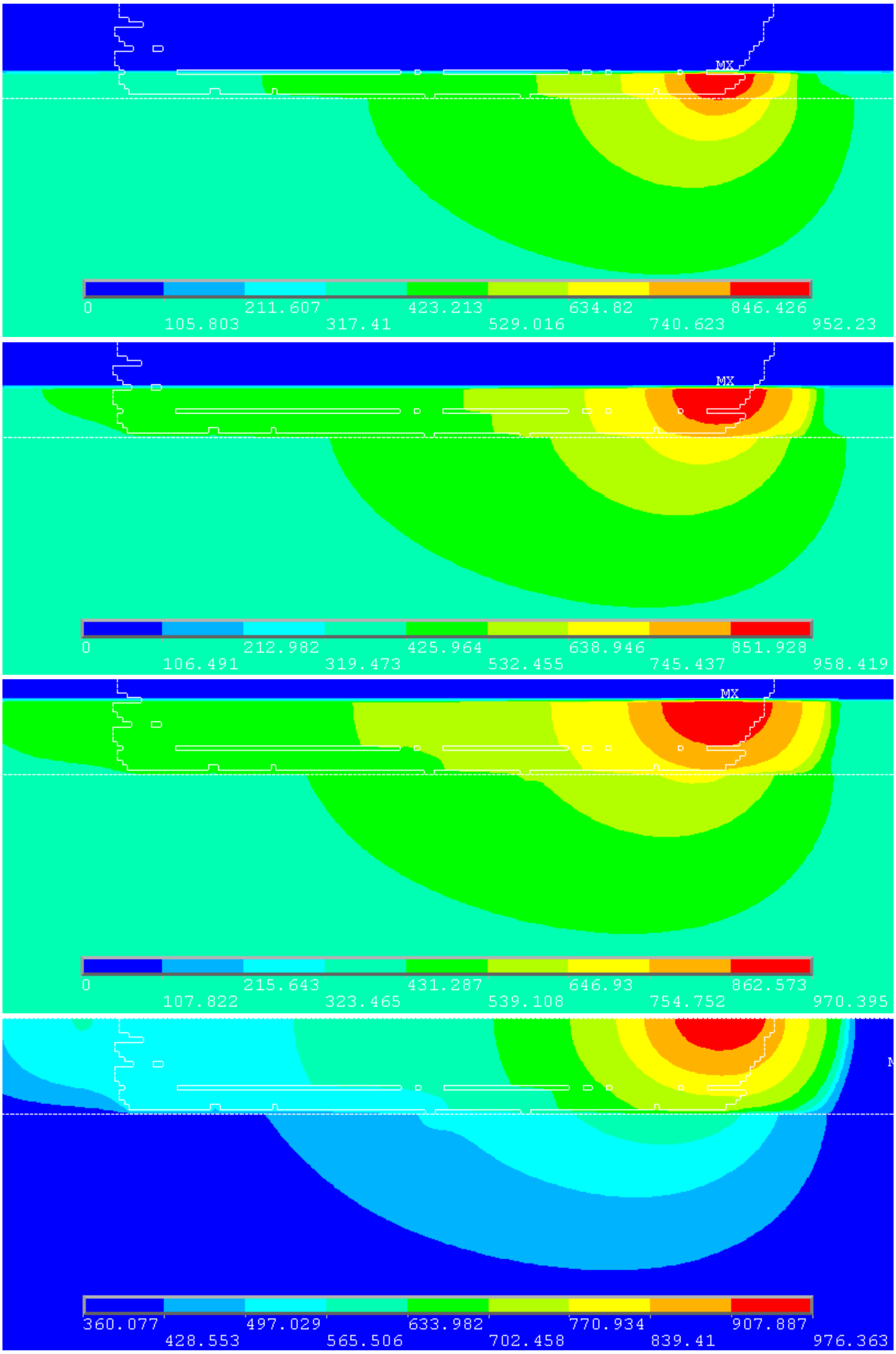

Figure 7. Evoution of the temperature profiles of sample 7.

Appendix 5

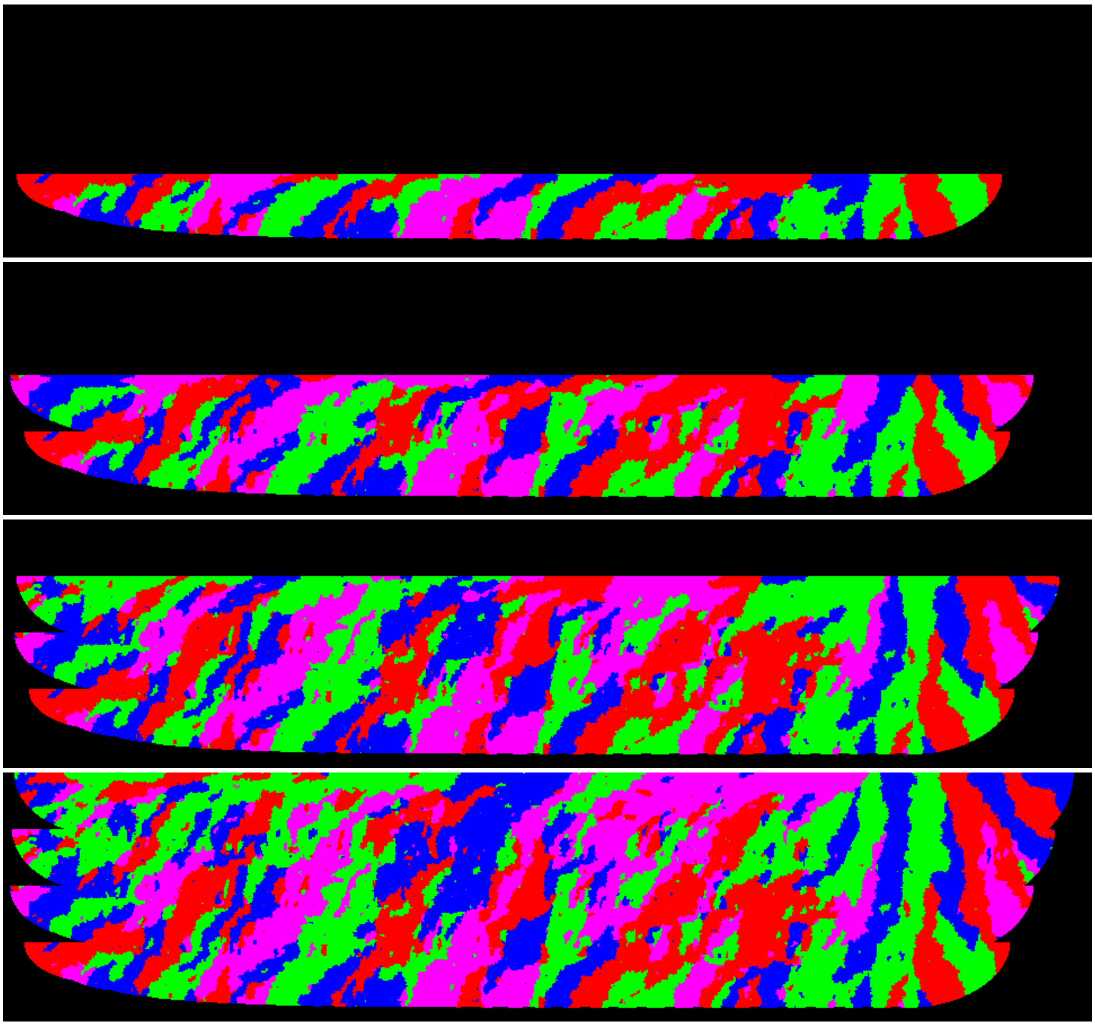

Figure 1. Microstructural evolution of sample 1.

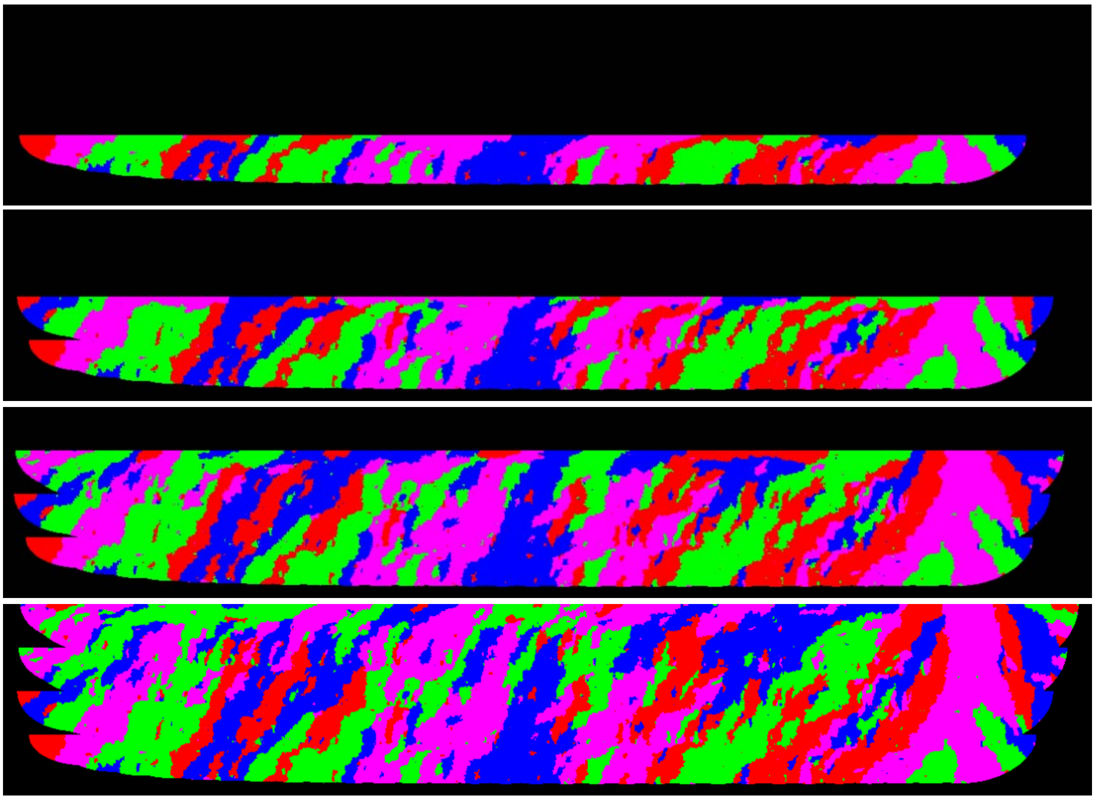

Figure 2. Microstructural evolution of sample 2.

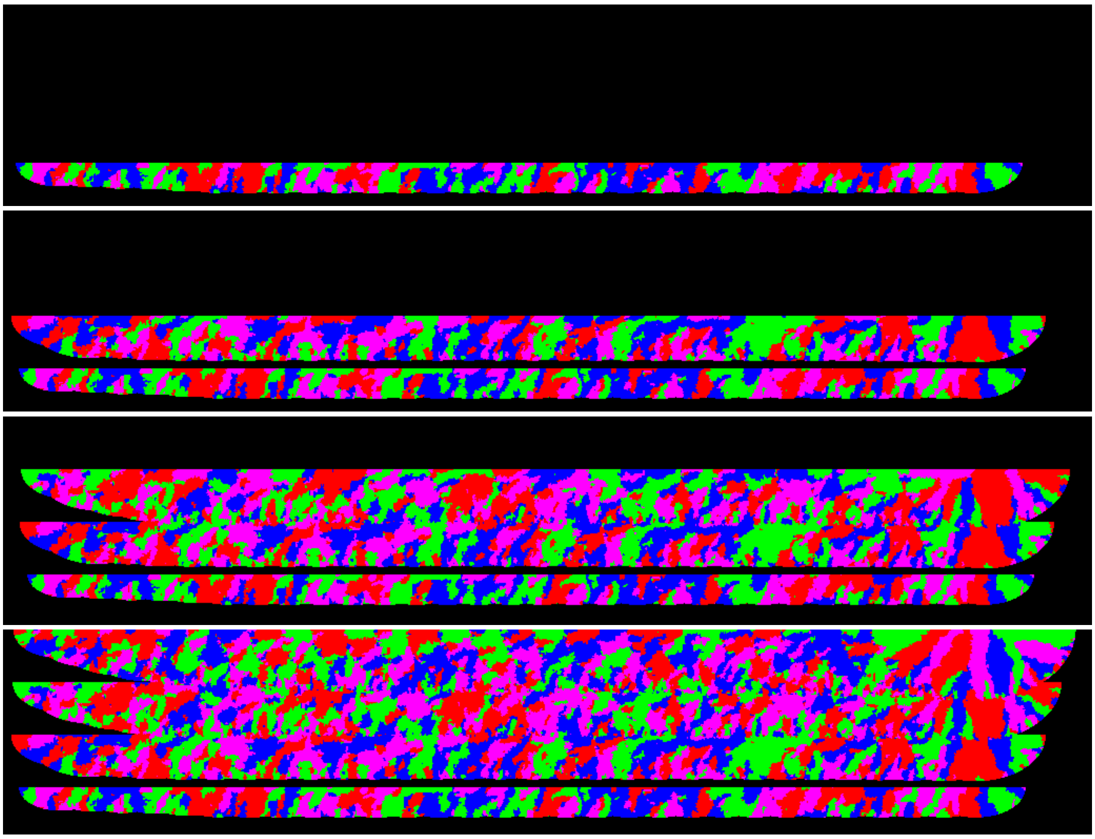

Figure 3. Microstructural evolution of sample 3.

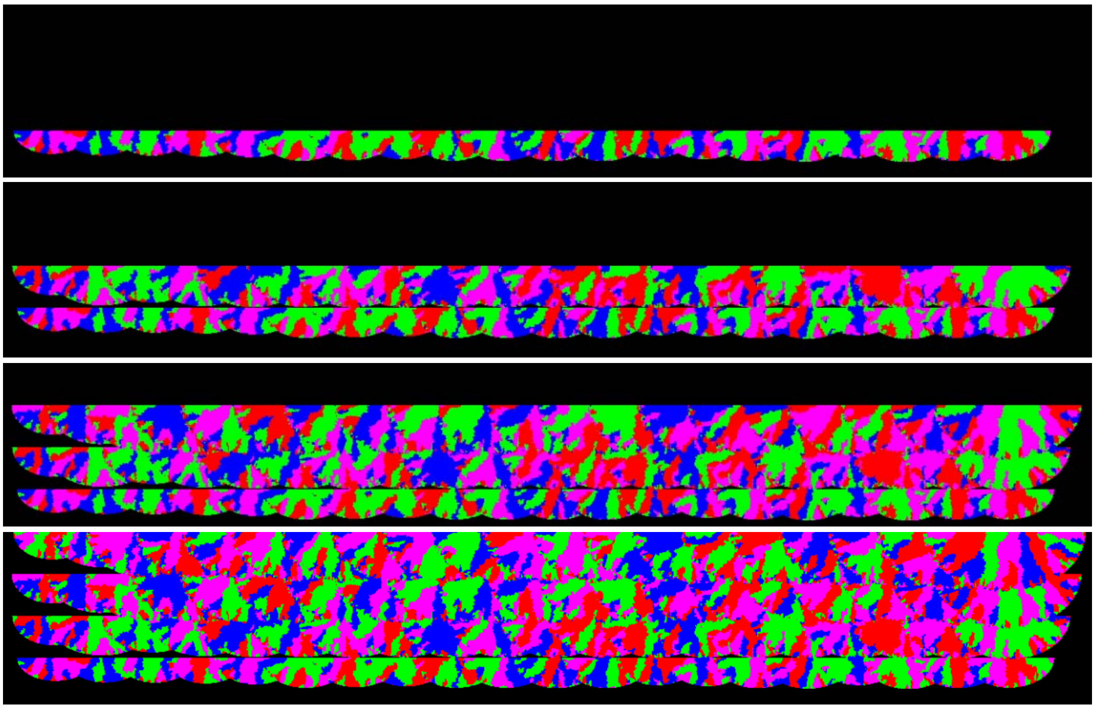

Figure 4. Microstructural evolution of sample 4.

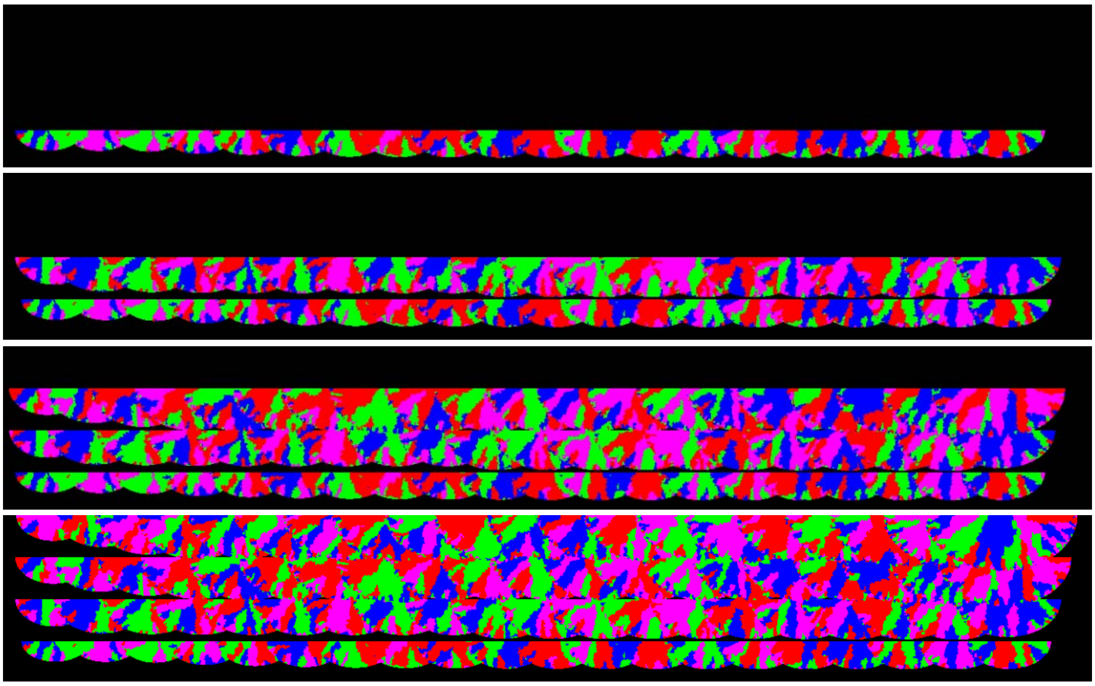

Figure 5. Microstructural evolution of sample 5.

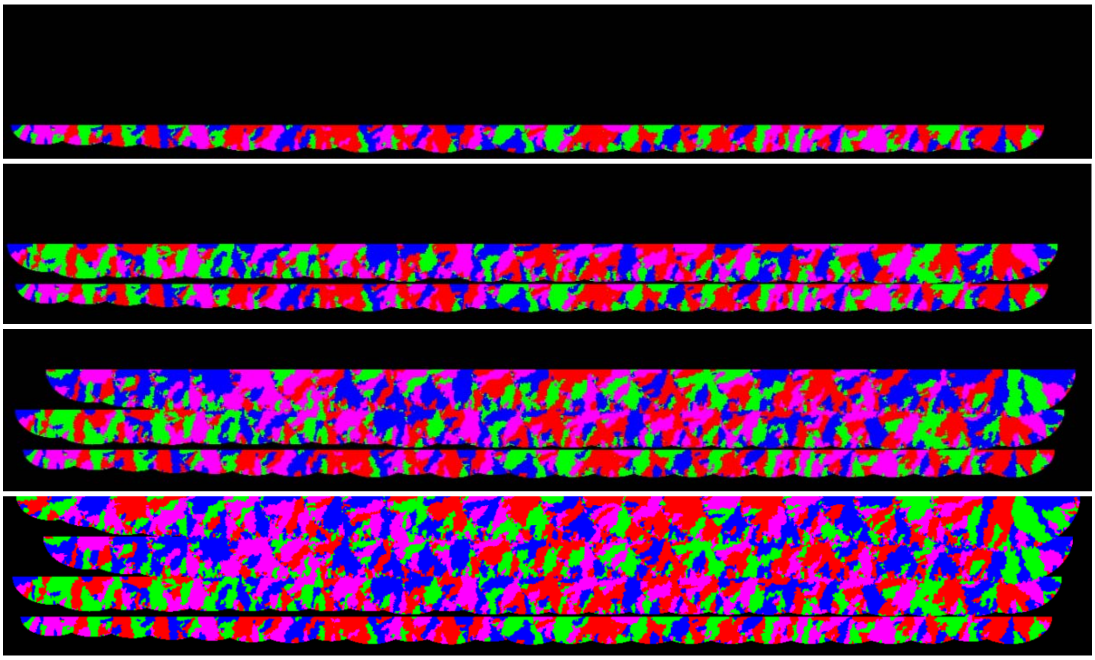

Figure 6. Microstructural evolution of sample 6.

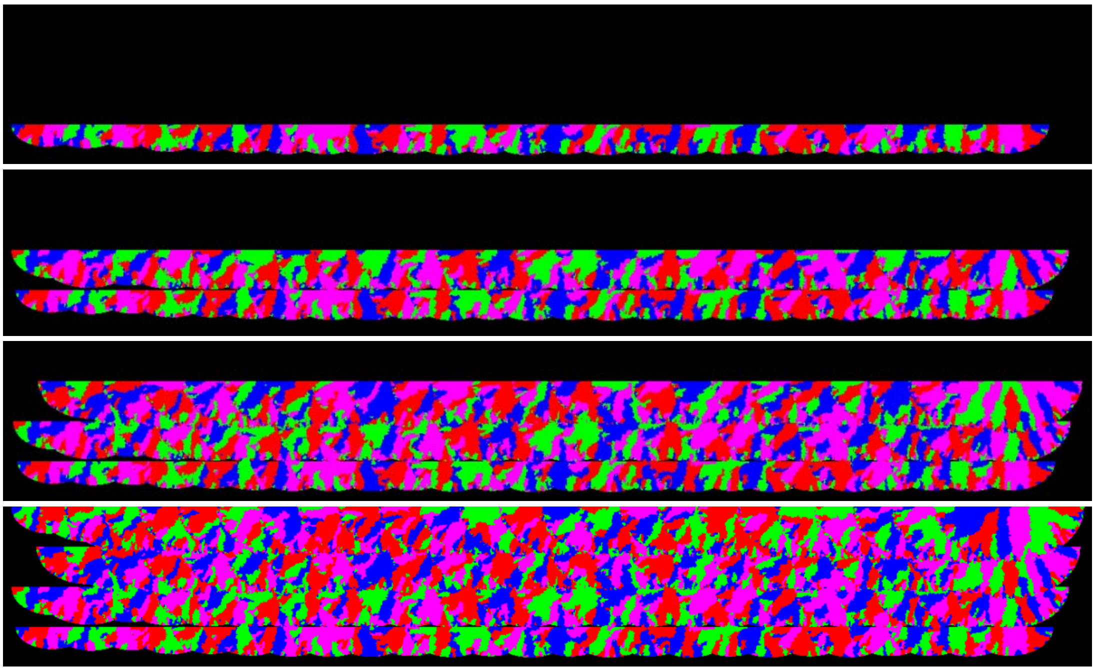

Figure 7. Microstructural evolution of sample 7.

Appendix 6

Measurement of the laser spot characteristics of the Renishaw SLM system performed with a Spiricon Laser Beam Analyser. The laser power used to perform the measurement was of 200W.

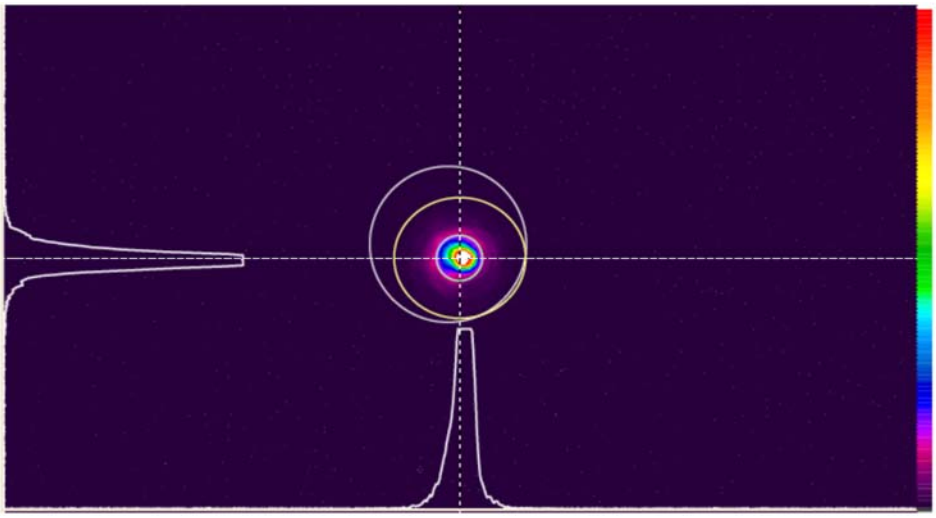

Figure 1. 2D Laser Spot Profile

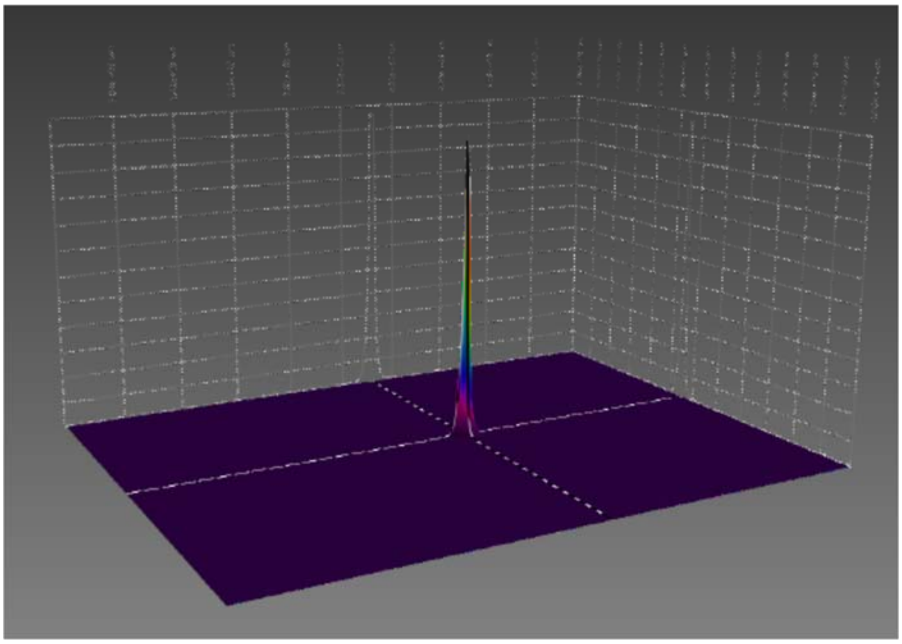

Figure 2. 3D Laser Spot Profile

Table 1. Data obtained from the Beam Analyser

Centroid X	3925.12μm
Centroid Y	2874.71μm
Diameter X	180.4μm
Diameter Y	140.8μm
Peak Diameter	163.2μm
Spot Diameter (measured at flatten profile of figure 1)	~53μm